TECHNISCHE UNIVERSITÄT MÜNCHEN

TUM School of Engineering and Design

System Identification with Coda Waves and Model Updating for Digital Twins in Civil Engineering

Stefan Grabke

Vollständiger Abdruck der von der TUM School of Engineering and Design der Technischen Universität München zur Erlangung eines

Doktors der Ingenieurwissenschaften (Dr.-Ing.)

genehmigten Dissertation.

Vorsitz:

Prof. Dr.-Ing. habil. Fabian Duddeck

Prüfende der Dissertation:

1. Prof. Dr.-Ing. Kai-Uwe Bletzinger
2. Prof. Dr.-Ing. habil. Roland Wüchner
3. Prof. Dr. techn. Günther Meschke

Die Dissertation wurde am 03.07.2024 bei der Technischen Universität München eingereicht und durch die TUM School of Engineering and Design am 28.10.2024 angenommen.

Schriftenreihe des Lehrstuhls für Statik
TU München

Band 68

Stefan Grabke

System Identification with Coda Waves and Model Updating for Digital Twins in Civil Engineering

München 2025

Veröffentlicht durch

Kai-Uwe Bletzinger
Lehrstuhl für Statik
Technische Universität München
Arcisstr. 21
80333 München

Telefon: +49(0)89 289 22422
Telefax: +49(0)89 289 22421
E-Mail: kub@tum.de
Internet: www.cee.ed.tum.de/st/

ISBN: 978-3-943683-79-0

Abstract

Structural health monitoring is an important field in civil engineering with increasing importance. On the one hand, this is due to high demands on the stability of structures, especially infrastructure, and on the other hand the aging of existing infrastructure in combination with ever-increasing loads. With ongoing digitalization in the construction industry, this thesis starts at the numerical level to make an important contribution by further developing model-based methods in structural health monitoring of large structures.

The thesis focuses on damage detection using coda waves that are a special type of ultrasound. The method is particularly suitable for use in concrete and benefits from the multiple scattering of the ultrasound in the medium, as this allows a significantly larger area to be monitored with very high sensitivity. The thesis also deals with a second method, computational model updating, whose mathematical principles are almost identical but whose applicability is much more general concerning measurement data, building materials, etc. Both methods allow damage to be localized and, in some cases, even classified by solving an inverse problem. They represent an essential interface between real buildings and digital models. Such models, which compare with the actual state using measurements, are called digital twins.

Damage localization with coda waves is being further developed in various aspects in this thesis. To enable more flexibility in boundary conditions and geometries than the analytical solutions typically used to date, the finite element method is derived and used for the required wave propagation simulations. In addition, it is shown in a laboratory test that damage localization can also be carried out at lower frequencies than those previously used in the literature. This extension of the frequency spectrum is an important contribution to applying the technology in large structures, as the signals can be transmitted further. Other developments in the thesis contribute to improved robustness and damage classification with coda waves. In particular, successful damage localization based on the evaluated phase shift in the signal is a promising novelty. The developments are being tested with a multi-stage experiment. All parameters are calibrated in a purely numerical experiment to subsequently test the settings found in a laboratory test. The damage localization based on FE simulations was successfully validated with comparatively low frequencies by reliably detecting and, for the most part, localizing occurring cracks. The evaluation at various load levels also underlines the immense sensitivity of coda waves to multiple influences. In addition to the laboratory test, the damage localization is also tested in a real, large structure, the Gänstorbrücke. Possible damage locations were localized in a load test.

With the computational model updating, a second model-based evaluation method of measurement data is derived and applied in the thesis. However, the method is significantly more universal and allows identified changes to be classified. As with the coda waves, the application-oriented investigations are carried out on a purely numerical experiment whose results are then applied in a real experiment. In summary, the developments of both methods and validation through real experiments make an important contribution to the ambitious goals of digital twins presented in this thesis.

Zusammenfassung

Die Zustandsüberwachung von Bauwerken ist ein wichtiger Bereich im Bauwesen, der zunehmend an Bedeutung gewinnt. Dies liegt zum einen an den hohen Anforderungen an die Standsicherheit von Bauwerken, insbesondere Infrastrukturbauten, sowie an der Alterung bestehender Bauwerke in Kombination mit immer größer werdenden Belastungen. Mit der fortschreitenden Digitalisierung im Bauwesen setzt diese Arbeit auf numerischer Ebene an, um durch die Weiterentwicklung modellbasierter Methoden in der Strukturüberwachung großer Bauwerke einen wichtigen Beitrag zu leisten.

Die Arbeit konzentriert sich dabei auf Schadenserkennung mit Hilfe von Ultraschall, in Form von Coda-Wellen. Das Verfahren ist speziell für die Anwendung in Beton geeignet und profitiert von der Mehrfachstreuung des Ultraschalls im Medium, da dadurch ein großer Bereich mit sehr hoher Empfindlichkeit überwacht werden kann. Die Arbeit befasst sich auch mit einer zweiten Methode, der rechnerischen Modellanpassung, deren mathematische Grundlagen nahezu identisch sind, aber dessen Anwendbarkeit viel allgemeiner in Bezug auf Messgrößen, Baumaterialien etc. ist. Beide Methoden erlauben es durch Lösen eines inversen Problems Schäden zu lokalisieren und teilweise sogar zu klassifizieren. Sie stellen eine bedeutende Schnittstelle zwischen realen Bauwerken und digitalen Modellen dar. Derartige Modelle, die über Messgrößen einen Abgleich mit dem realen Ist-Zustand durchführen, werden als digitale Zwillinge bezeichnet.

Die Schadenslokalisierung mit Coda-Wellen wird in dieser Arbeit in verschiedenen Aspekten weiterentwickelt. Zum einen wird für die Wellenausbreitungssimulation die Finite-Elemente-Methode hergeleitet und eingesetzt, da sie deutlich mehr Flexibilität bei Randbedingungen und Geometrien bietet als die bisher typischerweise verwendeten analytischen Lösungen. Darüber hinaus wird in einem Laborversuch gezeigt, dass die Schadenslokalisierung auch mit niedrigeren Frequenzen als den bisher in der Literatur verwendeten, durchgeführt werden kann. Diese Erweiterung des Frequenzspektrums ist ein wichtiger Beitrag zur Anwendung der Technologie in großen Strukturen, da Signale so über größere Distanzen übertragen werden können. Weitere Entwicklungen der Arbeit tragen zu einer verbesserten Robustheit und Schadensklassifizierung mit Coda-Wellen bei. Insbesondere die erfolgreiche Schadenslokalisierung auf Basis der ausgewerteten Phasenverschiebung im Signal ist eine vielversprechende Neuheit. Die Entwicklungen werden in einem mehrstufigen Experiment getestet. In einem rein numerischen Experiment werden alle Parameter kalibriert, um anschließend die gefundenen Einstellungen in einem Laborversuch zu testen. Die Schadenslokalisierung auf Basis von FE-Simulationen konnte mit den vergleichsweise niedrigen Frequenzen erfolgreich validiert werden, indem auftretende Risse zuverlässig erkannt und größtenteils lokalisiert wurden. Die Auswertung zu verschiedenen Belastungsstufen unterstreicht zudem die hohe Empfindlichkeit von Coda-Wellen gegenüber verschiedener Einflüsse. Zusätzlich zum Labortest wird die Schadenslokalisierung auch an einem realen, großen Bauwerk, der Gänstorbrücke, getestet. Mögliche Schadensstellen wurden in einem Belastungstest lokalisiert.

Mit der rechnerischen Modellanpassung wird eine zweite modellbasierte Auswertungsmethode von Messdaten hergeleitet und angewendet. Die Methode ist jedoch deutlich universeller und erlaubt eine Klassifizierung der identifizierten Veränderungen. Wie bei den Coda-Wellen werden die anwendungsorientierten Untersuchungen an einem rein numerischen Test durchgeführt, dessen Ergebnisse dann in einem realen Test angewendet werden. Zusammengefasst wird so durch Weiterentwicklung beider Methoden und Validierung durch reale Versuche ein wichtiger Beitrag zu den in der Arbeit vorgestellten ambitionierten Zielen von digitalen Zwillingen geleistet.

Acknowledgements

This thesis was written during my time as a research associate at the chair of Structural Analysis at the Technical University of Munich. The time was enriching, sometimes exhausting, and overall very formative for my professional and personal development. I can now defend a finished thesis after many years of work thanks to many people who supported me along the way and to whom I would like to express my gratitude.

First and foremost, I extend my sincere gratitude to Prof. Kai-Uwe Bletzinger, my supervisor, for his pivotal role in allowing me to conduct my research at the chair of Structural Analysis. His unwavering support, academic freedom, and guidance have not only shaped but also defined my research endeavors. I am deeply thankful to him for fostering an exceptional working environment that has allowed me to explore and thrive in my research interests. I am also deeply indebted to Prof. Roland Wüchner for his initial introduction to the topic and his invaluable guidance even after his departure to a different institute. His assistance and thought-provoking discussions have been instrumental in my technical and personal growth, for which I am truly grateful.

I want to thank Prof. Günther Meschke for completing my board of examiners and Prof. Fabian Duddeck for the organization.

Special thanks also to the Deutsche Forschungsgemeinschaft (DFG, German Research Foundation) for funding the research that contributed a lot to this thesis. I want to thank my colleagues within the research unit, Fabian, Eva, Felix, Noah, Niklas, Giao, Martin, and the associated PIs, for the helpful exchange and the good times during our plenary meetings at sometimes very special and enjoyable places.

Furthermore, I would like to thank all my colleagues, especially Martin, Ann-Kathrin, Aditya, Altug, Reza, Iñigo, Klaus, Thomas, Armin, Anna, Tobi, Shahrokh, Ihar, Manu, Veronika, Dagamawi, Basti, David, Talah, Andi and the recent new generation of PhDs at our chair who accompanied me over the past years for the insightful discussions, collaborative work, and our enjoyable time together. Especially during the lockdowns of the COVID-19 pandemic, I realized the vital and enriching role of joint lunch breaks and conversations with colleagues.

Lastly, I want to express my deepest gratitude to my family and friends. My parents for their constant support throughout my personal and educational career, my wife for her continuous support and advice, and her patience during this difficult but rewarding time of my life.

Stefan Grabke
Technische Universität München
February, 2025

Contents

List of Abbreviations

BAM Bundesanstalt für Materialforschung und -prüfung

BCs boundary conditions

BIM building information modelling

BVLS bounded-variable least squares

CC cross-correlation coefficient

CFL Condition Courant-Friedrichs-Lewy condition

CWI coda wave interferometry

DC decorrelation coefficient

DIC digital image correlation

DT digital twin

DTI digital twin instance

DTP digital twin prototype

FD finite differences

FE finite element

FEM finite element method

FOS fiber-optic sensor

LHS left-hand side

NDT non-destructive testing

NNLS non-negative least squares

PDE partial differential equation

P-waves primary waves

RHS right-hand side

RSS residual sum of squares

RTE radiative transfer equation

SHM structural health monitoring

SI system identification

SVD singular value decomposition

S-waves secondary waves

tof time-of-flight

Chapter 1

Introduction

1.1 Motivation

A civil engineer's job is to guarantee the safety of buildings and infrastructure throughout the structure's lifespan. In particular, a functioning and safe infrastructure plays a decisive role in a strong economy. Bridges are of enormous importance within the infrastructure and, simultaneously, one of the most sensitive parts. During their lifespan, structures change, damages can occur, and even today's loads are usually higher than the standards of years ago. For critical infrastructure such as bridges, it is thus essential to monitor structures' actual state to guarantee society's safety. In Germany, the need is also underlined by the advanced age of the infrastructure, as an approximate third of all bridges are already older than 50 years [1], which is old when considering the expected lifespan is between 50 and 100 years. Another motivation for preserving built infrastructure is minimizing new construction to reduce the use of raw materials and greenhouse gas emissions.

Germany has a well-established monitoring concept defined by the national code DIN 1076 [2]. It stipulates that bridges must be controlled every six years with an external, close-up visual inspection. However, this proven concept is very labor-intensive and ultimately a subjective assessment based on information visible on the surfaces of the structures. If damages are detected on the surface and should be examined more closely, also deeper in the structure, there are various methods from the field of non-destructive testing (NDT). However, these are usually associated with even more effort. In individual cases, NDT is already being used for permanent monitoring, also known as structural health monitoring (SHM). Contrary to visual inspection, permanent monitoring typically leads to an objective evaluation of the structures. One challenge with implementing SHM in, e.g., a national code is that the building materials strongly differ. Steel, for example, is a homogenous material, whereas

concrete is very inhomogeneous with a wild mix of cement, aggregates, and pores. Next to the material, accessibility or environmental influences are factors that can limit applicable NDT methods. A superordinate concept is needed to implement the various NDT methods into an integral predictive maintenance workflow. In order to do so, a modular structure is required so that measurement techniques can be combined in different ways, and digitalization must be as extensive and automated as possible. The digital twin (DT) concept, which describes a virtual model that communicates via a bi-directional dataflow with reality, is ideal. The communication between the virtual model and reality offers excellent potential for improving SHM. For example, the model can be used to structure measurement data much better and more clearly, and it can also be enriched with historical data. The exchange also makes it possible to compare calculations in the model with real measurement data to validate and improve the model and ultimately use it for predictions. This transfers the reactive maintenance towards predictive maintenance with accompanying long-term planning. An illustration of how to embed the DT concept into SHM can be seen in Fig. 1.1 from a report by the Federal Ministry for Digital and Transport in Germany on DTs for bridges [3].

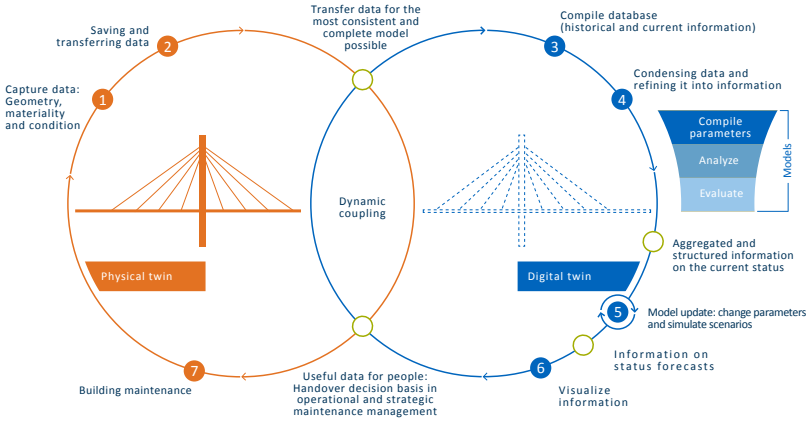

Figure 1.1: The value chain through the digital twin (adapted from [3]).

The overall DT concept of Fig. 1.1 combines the evaluations in the virtual space with the real structure on a general level to improve monitoring. However, parts of the used models are also continuously connected to reality. They either use measurement data for further computations, e.g., model-based imaging of damage or compare computational results to measurement data to improve the numerical models. This comparison with the status quo and the resulting improvement of the digital model is the key to reliable and meaningful models that can be potentially used for predictions or to

simulate scenarios. A universal method to improve the numerical models is the computational model updating (cf. Ch. 7 + 8).

Established SHM methods (strain gauges, displacement measurements, accelerometer, etc.; cf. Sec. 4.1) that can be used with computational model updating usually provide local information. This thesis also focuses on a technology that is suitable for large-scale monitoring of concrete, the coda wave interferometry (CWI) (cf. Ch. 4 - 6). See Planès et al. [4] for a good overview of the technology. CWI originates from geophysics, more precisely seismology, and is now applied to concrete structures. It is based on the principle that signals with their diffuse tail can be reproduced. As soon as small changes appear in the propagation medium, the signal changes slightly. These changes and especially their development within the signal are measured and evaluated. Coda waves are in a frequency such that they travel several meters through a specimen and are scattered multiple times, meaning they not only travel directly between source and receiver but also in a diffuse area around it. The scattering has the benefit that coarse sensor networks can monitor a large area. Another significant advantage of the scattering and longer travel distances within the specimen is an enormous sensitivity to changes that affect the coda signal. Parameters that affect the coda signal are, e.g., stress [5–8], temperature [9, 10], moisture changes [11], and damage in the form of micro- or macro cracks [12, 13]. Several groups [14–19] have conducted field experiments with CWI and demonstrated the immense potential of the technology. However, the immense sensitivity to all kinds of influences comes with challenges, such that it is more difficult to filter only influences from cracks. Next to detecting a fault somewhere in the monitored specimen, CWI also allows for localization and, with certain limitations, a classification. Work in this field was conducted by Larose et al. [20] and Zhang et al. [21, 22], who successfully applied CWI for damage detection in concrete structures. The mentioned studies are based on analytic solutions that describe the ultrasound behavior in concrete, which comes with limitations for applications in complex geometries. A major challenge in CWI is to find a good trade-off between large-area coverage of the geometry to be monitored, accuracy, and applicability. The frequency used plays a central role here. The presented work uses a central frequency of 60 kHz, which appears somewhat low at first glance compared to literature [4, 23] and the mentioned experiments [20–22] that all use frequencies above 100 kHz. A longer wavelength allows signals in concrete to be transmitted over a longer distance but is scattered less. It is thus questionable whether the known imaging methods based on multiple scattering can be used without further ado. Summarized has CWI great potential, as concrete is the most commonly used construction material, and the technology allows to combine monitoring of large areas with a very high sensitivity to little changes. Therefore, the focus of the application-oriented method developments as a contribution to a digital twin is on the coda wave technology. The computational model updating is also discussed to achieve universal applicability with various SHM technologies.

1.2 Objectives

The central objective of this thesis is developing and improving numerical methods for SHM applications that, in a bigger picture, contribute to a DT of structures. The two investigated methods, CWI and computational model updating, appear at first glance very different due to different kinds of measurements, but on the methodical and mathematical level, they are, in fact, very similar. The CWI is applied in this thesis for damage localization by solving an inverse problem. Several objectives are pursued in this work to improve the technology, namely:

- Application of finite element method (FEM) as a method for solving the governing problem instead of the established analytical solutions to make the damage localization with CWI versatile for complex structures.
- Extension of the multiple scattering-based imaging to a frequency of 60 kHz that, according to literature [4], belongs to the single scattering regime.
- Improvement of robustness to avoid manual filtering of measurement data
- Damage localization before, during, and after macrocrack formation to investigate the sensitivity of the technology, damage classification, and find application limits.
- Application of the developed algorithms in laboratory and field experiments.

On the one hand, CWI is a method specific to concrete, and, on the other hand, the imaging primarily localizes, but quantification of detected damage is challenging. In the end, only indirect conclusions can be drawn about structural-mechanical parameters that an engineer typically works with in his models when assessing a structure. For this reason, this thesis also investigates a method that can be used more universally and allows for quantifying stiffness changes: computational model updating. The universal applicability of computational model updating and comparing measurements with models to improve the computational model are central elements of DTs. Given the very ambitious goals of DTs, combining various measurement techniques and methods, as presented in this work, in one model is essential. Ultimately, this is the only way to achieve maximum precision and information content in the numerical model while maintaining robustness.

1.3 Outline

CHAPTER 2 introduces the concept of a digital twin (DT). It gives a brief historical overview and introduces the key differences between a (simple) digital model and a DT. Further on, the focus is on DTs in civil engineering, where different subtypes are specified and a classification in the context of this work is given.

CHAPTER 3 introduces the basics for solving ill-posed inverse problems. On the mathematical level, the later presented applications of CWI and computational model updating are very similar, and derived algorithms are thus universally applicable. Explanations of the mathematical algorithms start with a linear problem and then extend to necessary regularization techniques and non-linear problems. Finally, techniques to apply constraints on the solution and the applied algorithms are shown.

CHAPTER 4 starts a part of this thesis dealing with coda waves. The chapter introduces the technology in the context of NDT. Further, the basics of concrete and waves and the combination of ultrasound waves in concrete are discussed. The chapter continues with the basics of evaluation and influences on coda signals and the signal processing for later presented damage localization, as well as an overview of used hardware.

CHAPTER 5 presents contributions for imaging with coda waves. First, the widely used analytical solution is discussed. Then the use of FEM for the problem is derived, which is a significant improvement, especially when it comes to complex geometries. A further improvement of the FEM solution is shown, which is achieved by adding radiation terms describing the ballistic wave in a post-processing step. Afterwards, the choice of the central parameter of the simulations, the diffusivity, is discussed, and a novel method to obtain the parameter based on derivatives of the analytic diffusion solution is presented. The chapter continues with explanations of the inverse problem for damage localization with CWI. The problem is a linear one that uses gradient information. The necessary sensitivities of coda waves are derived based on models for multiple scattered waves. Also, a method that significantly improves the robustness and allows the presented models to work with measurement data from the rather low-frequency signal of 60 kHz is shown. In this novel idea, sensitivities are clipped in the areas near transducers. Interpretations and justifications for this modification are discussed in the corresponding section.

CHAPTER 6 shows results of CWI based damage localization. Three experiments are evaluated that build on each other and investigate different parameters. The first pure numerical experiment calibrates overall signal processing, simulation, and solving settings. The found settings are applied in the second one, an actual laboratory experiment. With a fiber-optic sensor (FOS) as reference technology, the sensitivity, accuracy, and robustness of CWI based damage localization are investigated. The chapter concludes with

a third experiment that performs damage localization on a field experiment at a real bridge.

CHAPTER 7 deals with computational model updating in structural analysis. It is the underlying basis for DTs that aim to represent reality with digital models as well as possible. The basis for the model updating is once again an inverse problem that uses gradient information. The sensitivities in this case are obtained by deriving the FEM problem directly with respect to the quantity of interest. The adjoint sensitivity analysis is beneficial for computing sensitivities for model updating. The chapter discusses the inverse problem of computational model updating with corresponding solution techniques. It concludes with an outlook on combining computational model updating with CWI based damage localization.

CHAPTER 8 applies the computational model updating in two experiments. As in the CWI part, the first one is a purely numerical one used to investigate different parameters such as mesh refinement and load and measurement positions. The second experiment is a simple real experiment of a 3-point bending test with moving load.

CHAPTER 9 finishes the thesis with a conclusion and gives an outlook for future research and developments.

Chapter 2

Digital Twin

2.1 Origins of the Digital Twin

The term digital twin (DT) is widely used in many industry fields, and its definitions vary. Especially within the last decade, the DT gained interest as increased computational power, sophisticated 3D visualizations, and sensor developments allowed for improved computation and visualization of reality. This chapter introduces the fundamental concept of a DT and then focuses on the application of DT ideas in civil engineering. In general, a DT refers to a concept with three components that are also visualized in Fig. 2.1:

- the real physical object in the *real space*
- the model or digital object in the *virtual space*
- a bidirectional data/information connection of the two spaces

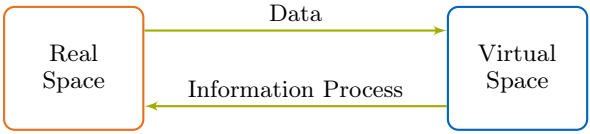

Figure 2.1: Early digital twin concept (adapted from [24]).

An existing example of a DT is, e.g., Google Maps [25], which nowadays offers real-time updates of the traffic situation due to a data flow from real to virtual space. The information process that points in the other direction from an optimization process in the virtual space could be a route change suggested by Google Maps due to a traffic jam.

In 1991, Gelernter [26] named the idea of the DT concept *Mirror Worlds*. In 2002 Grieves [27], who has a background in product lifecycle management, called this concept *Mirrored Spaces Model* and later further developed it to an *Information Mirroring Model* [28–30]. The term DT, together with a detailed definition, was introduced in a report by NASA in 2010. The report describes a DT as "an integrated multiphysics, multiscale simulation of a vehicle or system that uses the best available physical models, sensor updates, fleet history, etc., to mirror the life of its corresponding flying twin. The digital twin is ultra-realistic and may consider one or more important and interdependent vehicle systems."[31] As the DT is nowadays a widely applied concept, several other definitions have been published. Tab 2.1 lists a selection of DT definitions from science and industry that show a large variety. A review on DTs from Liu et al. [40] lists 21 different published definitions that come from all sorts of application fields and focus on different aspects such as the required high accuracy of the virtual model, a real-time data exchange, the adaption of either real or virtual space to the other space or the modeling of the whole life cycle of an object. However, due to the hype around DT, there are also definitions, such as the one by the Centre for Digital Built Britain at the University of Cambridge, that just renamed technology that has existed for years. An interesting aspect is highlighted by the definition of Arup [35]. Due to the bidirectional feedback loop, machine learning and artificial intelligence have great potential to improve the DT. According to their definition, the aim of the DT is not only to react to a new situation but to take action because artificial intelligence expects a situation to be avoided.

Michael Grieves, who significantly developed the early concepts for DTs, also distinguishes between different subtypes of DT: a digital twin prototype (DTP) and a digital twin instance (DTI)[33]. The DTP refers to an object or product in development where a physical object does not necessarily exist. To manufacture a physical instance, the DTP contains all the information on design, parts, processes, etc. The model can also optimize all parts in the DTP. Overall, the DTP can thus also be regarded as a rebranding of existing methods. The DTI, on the other hand, describes a physical object to which an individual digital twin remains connected throughout the entire life cycle. Therefore, it could be necessary to update the virtual space due to changes in the real space. Those changes are, e.g., registered by sensors that send data to the virtual space and update it.

Source	Definition from science
Cambridge Centre for Digital Built Britain [32] *Academia*	A digital twin is a realistic digital representation of something physical.
Grieves et al. [33] *Academia*	Digital twin is a set of virtual information constructs that fully describes a potential or actual physical manufactured product from the micro atomic level to the macro geometrical level.
Madni et al. [34] *Academia*	A digital twin is a virtual instance of a physical system (twin) that is continually updated with the latter's performance, maintenance, and health status data throughout the physical system's life cycle.
	Definition from industry
Arup [35] *Construction*	A digital twin is the combination of a computational model and a real-world system designed to monitor, control and optimize its functionality. Through data and feedback, both simulated and real, a digital twin can develop capacities for autonomy and to learn from and reason about its environment.
Deloitte [36] *Consulting*	A digital twin is a near-real-time digital image of a physical object or process that helps optimize business performance.
General Electric [37] *Conglomerate*	A digital twin is a living model that drives a business outcome.
IBM [38] *Software*	A digital twin is a virtual representation of a physical object or system across its lifecycle, using real-time data to enable understanding, learning and reasoning.
Siemens [39] *Conglomerate*	A digital twin is a virtual representation of a physical product or process, used to understand and predict the physical counterpart's performance characteristics.

Table 2.1: Overview on different DT definitions from science and industry (from [35] and [40]).

2.2 From Digital Model to Digital Twin

A difficult question in the field of DT is how to differentiate a digital model from a DT. Wright et al. [41] answer this with the mandatory requirement of the physical twin and real-time bidirectional communication between the two spaces. If this connection lacks an automated data flow in one direction Kritzinger et al. [42] propose three subtypes: digital model, digital shadow, and digital twin, and refer to the three types as different levels of integration.

Digital Model The authors refer to a digital model as "a digital representation of an existing or planned physical object that does not use any form of automated data exchange between the physical object and the digital object" [42] (cf. Fig. 2.2). For a digital model, definitions from

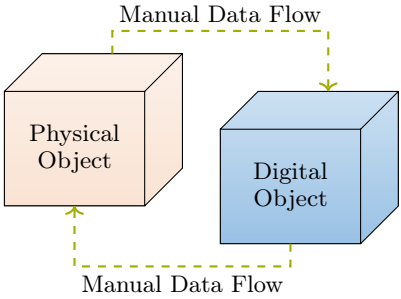

Figure 2.2: Definition of Kritzinger et al. [42] for a digital model.

model theory are applicable. Banks [43], e.g., describes a model as a simplification and, therefore, an abstraction of a system. Nevertheless, the model must be complex enough to fulfill its purpose, for example, to answer questions about the system's behavior in a specific situation and simulate it with sufficient accuracy. Kritzinger et al. [42] also proposes that a digital model can exchange data between physical and digital objects but only manually, such that a change in the state of one object has no direct effect on the other object.

Digital Shadow The digital shadow is based on the previous definition of a digital model with the extension of an automated one-way data flow from the physical object to the digital object (cf. Fig. 2.3). This means that a change of the physical object registered, e.g., by sensors, directly leads to changes in the digital object, but not vice versa. Another definition of the Fraunhofer-Gesellschaft [44] for a digital shadow (with manufacturing background) emphasizes the sufficiently accurate image of the real processes to create a real-time evaluation basis of all relevant data.

Digital Twin Kritzinger et al. [42] define the digital twin with a fully integrated and automatized data flow between physical and digital

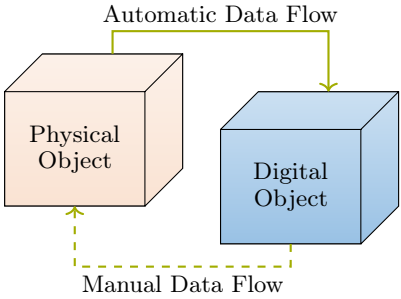

Figure 2.3: Definition of Kritzinger et al. [42] for a digital shadow.

objects in both directions (cf. Fig. 2.4). Thus, it is a digital shadow plus the ability to directly apply changes in the digital model on the physical one, e.g., use the digital model as a controlling or optimization instance of the physical object. Wright et al. [41] further elaborate that "the model used in a digital twin needs not be a data-driven model, but it should produce results that are directly equivalent to a measured quantity (so that the model updating process is data-driven), and the model will likely take in other measured quantities as boundary conditions, loads, or material properties." Also a validated digital model in the authors understanding is only a snapshot and a DT "can extend the use of that model to timescales over which the object and its behavior will change significantly" [41], so, in other words, is continuously validated by data.

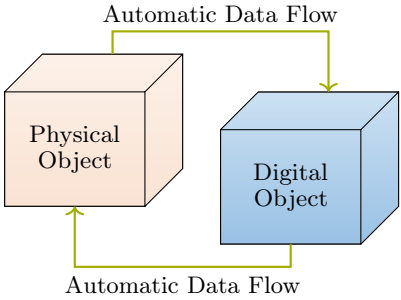

Figure 2.4: Definition of Kritzinger et al. [42] for a digital twin.

The concept of DTs is applied in various industry fields nowadays, and numerous publications and reports exist. The same terminology is used in the context of very different framework conditions. The bidirectional data flow is way easier for machines that regulate themselves with digital twins

than in the built environment. When thinking, for example, of a bridge, it is questionable how the built, static structure could adapt due to results, optimization, etc., from the virtual model. Nevertheless, the DT concept is also applied for large-scale constructions ([45–47]). It is usually referred to as a DT, although according to the definition of Kritzinger et al. [42], it is a digital shadow. This thesis follows the generic understanding that a DT is present as soon as the real and virtual space are connected. To differentiate between the capabilities, complexity, and connectivity of the digital twin, a differentiation by capability levels is used in this thesis. It is presented in a report of the construction company Arup [35] and further elaborated by Wenner et al. [3] (cf. in Fig. 2.5). Here, the descriptive level 1 is equivalent

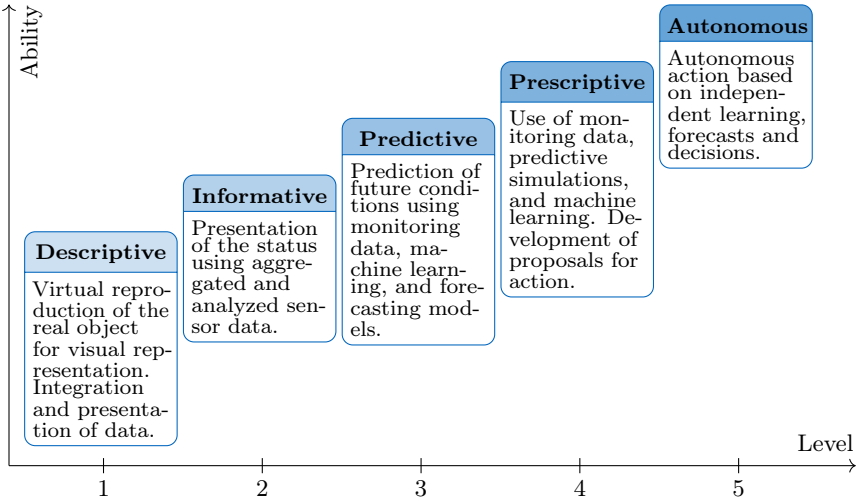

Figure 2.5: Capability levels of digital twins (adapted from [3]).

to the digital model. The informative level 2 is equivalent to a digital shadow. According to the definition, the predictive level 3 and the prescriptive level 4 have a unidirectional data flow with increasing intelligence due to machine learning. However, they would still be a digital shadow according to Kritzinger et al. [42]. Only at level 5, where autonomous decisions also have automatic real-time transfer back to the real space a true DT is achieved.

2.3 Digital Twin in Civil Engineering

The concept of DTs also found its way into the large variety of civil engineering. A good overview of implemented DTs in the build environment can be found in a report by Arup [35]. The report also differentiates 5 different types of DT in civil engineering that are further elaborated by Wenner et al. [3]:

Asset Twin An asset twin is the digital representation of an object, such as a bridge or building. The object thereby consists of several parts. The focus is, however, not on individual parts but the whole object and its overall performance and functionality. The individual parts would be called component twins, and the interactions are called system twins. An example of an asset twin is, e.g., a bridge. It exists of several parts such as supports, main girder, pylons, cables, etc. Thereby, the role of a component twin would be to monitor a specific part, e.g., the cables. The role of the asset twin would be to collect all data, structure and analyze it, and draw a conclusion about the overall operational state.

Component Twin As mentioned in the asset twin, a complex system can be differentiated by detail and overall focus. A component twin is an individual part of particular interest within a larger object. In the bridge example, a component twin could be a cable in a cable-stayed bridge. The elongation of such cables can be measured with strain gauges and set in relation to calculated values in a component twin.

System Twin A system twin refers to interconnected objects. It is closely related to asset twins as both consist of multiple parts. System twins focus on controlling the relations and dependencies of all the different parts. An example from the built environment is smart home automatization. The house is the object, and automated technical equipment with sensors such as air conditioning, sun protection, and heating systems are the individual parts. All the mentioned parts can affect the temperature within the house. The goal of a system twin would be to find an optimized setting such that, in the end, a pleasant living environment is obtained and the parts do not work against each other.

Process Twin A process twin monitors physical processes or sub-processes in real-time. Processes can also be optimized, and problems can be quickly identified and rectified. Wenner et al. [3] name the maintenance process of transport infrastructure as an example from civil engineering. The process twin manages from the recording of damage until maintenance measures the whole lifecycle of objects, assigns responsibilities and deadlines, and controls cost-effectiveness.

Network of Systems The case that various types of DTs from different domains are connected is called a network of systems. An example is a city where residential buildings, factories, energy and water systems, public transport systems, and infrastructure all communicate [48].

A concept closely related to the one of DT in civil engineering is building information modelling (BIM). The aim of BIM is to bundle all relevant

building data and related processes in a digital model. The close connection to DTs is therefore obvious. Kaewunruen et al. [49–51] even state that "BIM is digital twin" [40]. A report by the Federal Ministry for Digital and Transport in Germany classifies the two in relation to each other as follows: "The most important component of the DT is the BIM model. This fundamental data source is the basis for navigation in the visualization, locating data sources, and mapping the building taxonomy. In addition, important information from the building inspection, building diagnostics, and, depending on the degree of maturity, from the building monitoring is located and visualized within the BIM model. Other condition-relevant data (e.g., satellite images, vehicle or smartphone data) can also be included. At higher capability levels, the heart of the digital twin is automated data processing, which processes the raw data into aggregated condition information and can be used as a basis for forecasting conditions. However, non-aggregated information from third parties can also be imported (embedded data) or linked (linked data) within the digital twin. All this information is made available to users in a structured, needs-based, and intuitive way via a human-machine interface. While BIM has so far mainly been used for the planning and construction of infrastructure structures, the digital twin now also enables the BIM method to be transferred to construction operations."[3] (translated from German). Summarized, one can say that the BIM model is part of the DT. However, overall functionalities of DTs due to real-time sensor data with data analysis and possibilities of simulation and prognosis that lead to forecasting models and decisions extend the ideas of BIM (cf. Fig 2.6).

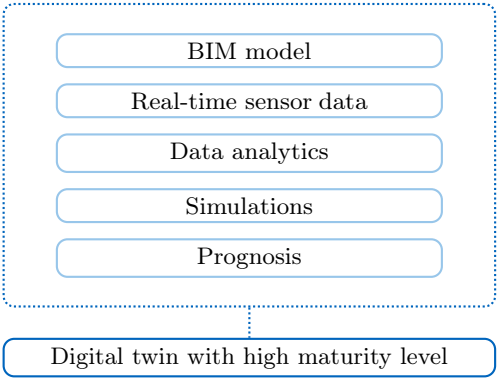

Figure 2.6: BIM and digital twin (adapted from [3]).

This thesis focuses on the monitoring of large structures in civil engineering. The aforementioned report by the Federal Ministry for Digital and Transport in Germany [3] gives a good overview of how a DT of bridges looks like in its contribution to the digital twin Federal Trunk Roads Master Plan (cf. Fig. 1.1). Another example of how an asset twin of a bridge could be structured is given in Fig. 2.7.

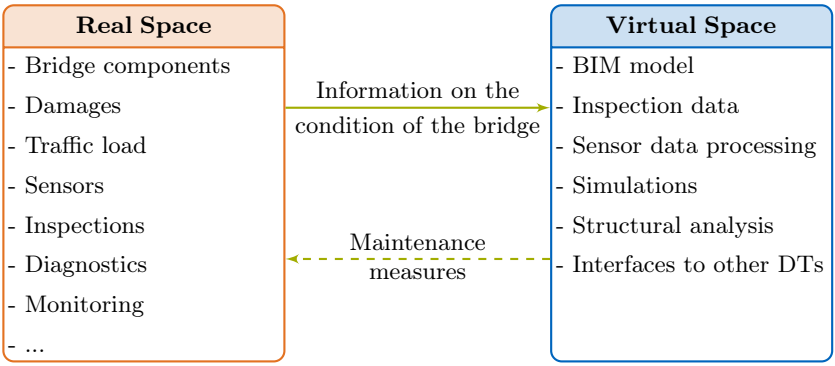

Figure 2.7: Digital twin for bridges.

The report also gives an overview of the current state of DTs for bridges in Germany. At the moment, very few DTs of capability level 2 exist that, in certain aspects, behave and react as the represented asset. Grabe et al. [45], Wenner et al. [46], and Lazoglu et al. [47] give further insights into the mentioned projects in Germany.

The work presented in this thesis contributes to a component twin of a bridge part that is monitored. Ch. 5 deals with method development, validation, and improvement for the SHM with coda waves. With a virtual model that can describe the behavior of ultrasound in concrete structures, it is possible to image changes such as damage. Applying the same DT ideas to combine measurements and simulations is also done with structural models in Ch. 7, where computed displacements are compared with measured ones. Using the differences between simulation and reality, one can identify changes with an inverse problem from computational model updating. Further work in this field with similar methods is done by Airaudo et al. [52] and Löhner et al. [53]. Another significant benefit of DTs in structural analysis is the continuous validation due to the feedback between structural models and reality, which significantly improves confidence in a virtual model and is a key to forecasting models. The presented methods are required to analyze measurement data and draw conclusions about the structure's actual state. They are, therefore, essential to get from an informative level 2 DT to a predictive level 3 DT and beyond.

Chapter 3

Solution Strategies for Ill-Posed Inverse Problems

This thesis deals with system identification based on measurement data. For this purpose, a model that allows system information to be related to measurement data is used. The big challenge is to determine the model's input parameters so that the computed responses have the closest possible match to the measurement data. This problem of finding the best solution is the typical case of an inverse problem that, in this case, is ill-posed. The mathematical fundamentals, as well as strategies to solve the problem, are discussed in this chapter. Fig. 3.1 gives an idea of a typical inverse problem for imaging with CWI measurements (cf. Ch. 5).

3.1 Ill-Posed Problems

The fundamental problem that arises in system identification applications can be expressed with a function $f : \mathbb{R}^n \mapsto \mathbb{R}^m$:

$$f(\mathbf{x}) = \mathbf{y} \tag{3.1}$$

The challenge of an inverse problem is to find $\mathbf{x} \in \mathbb{R}^n$ with given $\mathbf{y} \in \mathbb{R}^m$ such that the residual $\mathbf{r}$ is zero:

$$\mathbf{r} = \mathbf{y} - f(\mathbf{x}) = \mathbf{0} \tag{3.2}$$

The function $f(\mathbf{x})$ is non-linear in most application fields. To solve the inverse problem with the gradient-based Newton method, $f(\mathbf{x})$ is linearized in $\mathbf{x}_k$ with a Taylor series of first order:

$$f(\mathbf{x}) \approx f(\mathbf{x}_k) + \nabla f(\mathbf{x}_k)^T (\mathbf{x} - \mathbf{x}_k) \tag{3.3}$$

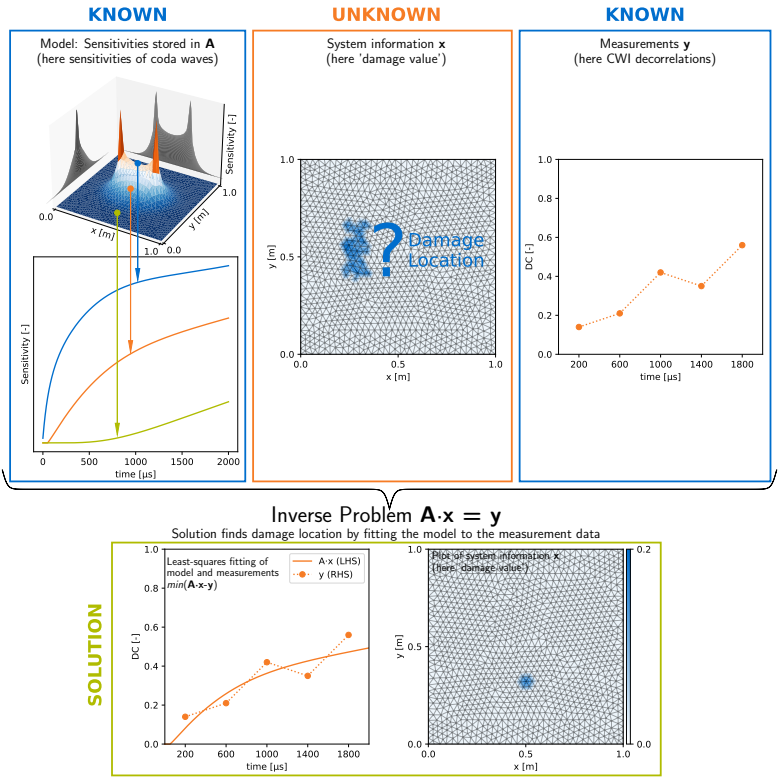

Figure 3.1: Visualization of a typical inverse problem for system identification with measurement data.

The nabla operator (∇) refers to the gradient of $f(\mathbf{x})^T$ in $\mathbf{x}_k$ and in mathematics is known as the Jacobi matrix referred to with $\mathbf{A}$ in this thesis.

The explanations on ill-posed problems start with the linear case and are in Sec. 3.5 extended to the non-linear case. For the linear case, the Taylor series approximation of $f(\mathbf{x})$ in Eq. 3.3 is independent of the linearization point $\mathbf{x}_k$. A linearization in $\mathbf{x}_k = \mathbf{0}$ leads to

$$\tilde{f}(\mathbf{x}) \approx \mathbf{y}_0 + \mathbf{A}\mathbf{x} \tag{3.4}$$

As a simplification, $\mathbf{y}_0$ is chosen as zero, which is valid for the case that in the zero-state ($\mathbf{x} = \mathbf{0}$) measurements $\mathbf{y}$ are also zero. This is,e.g., the case for the imaging with coda waves pictured in Fig. 3.1 where one can say that if nothing changes, so no damage $\mathbf{x}$ appears, nothing is measured. With Eq. 3.4 inserted into Eq. 3.2 one obtains the following linear inverse problem:

$$\mathbf{A}\mathbf{x} = \mathbf{y} \qquad \text{with } \mathbf{A} \in \mathbb{R}^{m \times n}\,,\, \mathbf{y} \in \mathbb{R}^m \tag{3.5}$$

A problem as in Eq. 3.1 or the simplified linear relation in Eq. 3.5 has three requirements to be classified as a well-posed problem [54]. A solution $\mathbf{x}$ of the problem exists (existence), there is at most one solution (uniqueness), and it depends contentiously on the data (stability). For the practical application case of a fit of a numerical model to real measurement data, these requirements are not fulfilled. Due to noise and modeling errors, there is a lack of a solution that reduces the residual to zero, which means the problem is inconsistent. In case of fewer measurements than parameters to be adjusted, it is also underdetermined, which conflicts with the uniqueness requirement. The stability requirement ensures that small errors in the data cause only small errors in the solution. Kress [55] names the condition number κ of a matrix as a measure for the degree of well-posedness or stability. For a rectangular matrix $\mathbf{A} \in \mathbb{R}^{m \times n}$ it can be computed as follows

$$\kappa(\mathbf{A}) = \frac{\sigma_{\max}(\mathbf{A})}{\sigma_{\min}(\mathbf{A})} \tag{3.6}$$

where $\sigma_{\max}(\mathbf{A})$ and $\sigma_{\min}(\mathbf{A})$ are maximal and minimal singular values of $\mathbf{A}$, respectively. In the present cases of this thesis, the condition numbers are significantly larger than 1, which means the matrix is ill-conditioned.

The lack of a unique, stable solution requires reformulations for numerical treatment. For the present case of an ill-posed problem, the additional assumption of a smooth solution, also referred to as regularization, is introduced. A standard method for regularization used in this thesis is the Tikhonov regularization (Sec. 3.3).

3.2 Least-Squares Optimization Problem

An optimization problem generally tries to find the best solution from all feasible solutions. As shown in the example of Fig. 3.1 in the plot on the bottom left, no solution fits the model to the measurements without remaining error, which means the problem is inconsistent. Thus, the standard approach for solving the inconsistent linearized problem of Eq. 3.5 known as the Gauss-Newton method is a reformulation to a least square optimization problem that minimizes the residual of Eq. 3.2:

$$\min_{\mathbf{x} \in \mathbb{R}^n} \|\mathbf{y} - \mathbf{A}\mathbf{x}\|_2^2 \qquad \text{with } \mathbf{A} \in \mathbb{R}^{m \times n} \text{ , } \mathbf{y} \in \mathbb{R}^m \tag{3.7}$$

This expression is also called the optimization problem's objective function. The solution of this quadratic extreme point problem is found by setting the gradient to zero:

$$\begin{aligned} \nabla \|\mathbf{y} - \mathbf{A}\mathbf{x}\|_2^2 &= \mathbf{0} \\ \nabla (\mathbf{y} - \mathbf{A}\mathbf{x})^T (\mathbf{y} - \mathbf{A}\mathbf{x}) &= \mathbf{0} \\ \mathbf{A}^T\mathbf{A}\mathbf{x} - \mathbf{A}^T\mathbf{y} &= \mathbf{0} \end{aligned} \tag{3.8}$$

$$\mathbf{A}^T\mathbf{A}\mathbf{x} = \mathbf{A}^T\mathbf{y} \tag{3.9}$$

The term of Eq. 3.9 is also called normal equation because geometrically, the residual is orthogonal to the range of $\mathbf{A}$ at the solution $\mathbf{x}$. Eq. 3.9 can be used to solve for $\mathbf{x}$:

$$\mathbf{x} = \underbrace{(\mathbf{A}^T\mathbf{A})^{-1}\mathbf{A}^T}_{\text{Moore–Penrose inverse } \mathbf{A}^+} \mathbf{y} \tag{3.10}$$

The term of Eq. 3.10 contains the Moore-Penrose inverse $\mathbf{A}^+ = (\mathbf{A}^T\mathbf{A})^{-1}\mathbf{A}^T$ [56, 57]. It is also known as pseudoinverse as it is a generalization of the inverse matrix to singular and non-square matrices.

Another way to compute the Moore-Penrose inverse that is numerically more stable uses the singular value decomposition (SVD). The compact SVD decomposes the matrix $\mathbf{A} \in \mathbb{R}^{m\times n}$ in the two orthogonal matrices $\mathbf{U} \in \mathbb{R}^{m\times r}$ and $\mathbf{V} \in \mathbb{R}^{n\times r}$ and a diagonal matrix $\mathbf{\Sigma} \in \mathbb{R}^{r\times r}$ where $r \leq \min\{m, n\}$ is the rank of $\mathbf{A}$.

$$\mathbf{A} = \mathbf{U}\mathbf{\Sigma}\mathbf{V}^T = \sum_{i=1}^{r} \sigma_i \mathbf{u}_i \mathbf{v}_i^T \tag{3.11}$$

The diagonal matrix $\mathbf{\Sigma} = diag(\sigma_1, ..., \sigma_r)$ contains the singular values σ_i ordered by magnitude on its diagonal and scaled such that $\sigma_1 > \sigma_2 > ... > \sigma_r > 0$. The columns of $\mathbf{U}$ are the left singular vectors of $\mathbf{A}$, and the columns of $\mathbf{V}$ are referred to as the right singular vectors. With the matrices of the SVD, the pseudoinverse can be computed as follows:

$$\mathbf{A}^+ = \mathbf{V}\mathbf{\Sigma}^+\mathbf{U}^T \qquad \text{with } \sigma_{ii}^+ = \begin{cases} 0, & \text{if } \sigma_{ii} = 0, \\ \frac{1}{\sigma_{ii}}, & \text{else.} \end{cases} \tag{3.12}$$

When using the components of the SVD, only the diagonal matrix is inverted, which is numerically more stable than inverting a full matrix.

3.3 Tikhonov Regularization

For the Tikhonov regularization that was independently introduced by Phillips [58] in 1962 and Tikhonov [59] in 1963, a regularization term is included in the minimization:

$$\min_{\mathbf{x}\in\mathbb{R}^n} (\|\mathbf{y} - \mathbf{A}\mathbf{x}\|_2^2 + \|\mathbf{\Gamma}\mathbf{x}\|_2^2) \tag{3.13}$$

The regularization is performed by adding the Tikhonov matrix $\mathbf{\Gamma}$. The standard choice for $\mathbf{\Gamma}$, which is also used in this thesis, is as a scalar α multiplied with the identity matrix $\mathbf{I}$:

$$\mathbf{\Gamma} = \alpha\mathbf{I} \tag{3.14}$$

The Tikhonov matrix can be understood as a penalty term that regularizes the solution by, at the same time, providing a small residual of the initial problem as well as a moderate value of the penalty term. If the problem is not regularized, large oscillations usually appear in the solution. These large

values are penalized in the Tikhonov regularization, and a smooth solution is obtained with a good choice of α. With the regularization parameter α, the confidence in the model can be controlled. In the case of a very small value, the problem is very close to the original one, and instabilities have to be expected. If the value is chosen too large, there is only little connection to the original problem. A method of finding a good regularization parameter is the L-curve method by Hansen [60] (cf. Sec. 3.4).

When searching the minimum of Eq. 3.13, the gradient is set to zero as in Eq. 3.8. This leads to the following expression containing the Tikhonov matrix:

$$\mathbf{x} = (\mathbf{A}^T\mathbf{A} + \mathbf{\Gamma}^T\mathbf{\Gamma})^{-1}\mathbf{A}^T\mathbf{y} \tag{3.15}$$

In a Bayesian interpretation, $\mathbf{\Gamma}^T\mathbf{\Gamma}$ can be understood as the inverse covariance matrix of the solution $\mathbf{C}_X^{-1}$ that, as Link [61] describes, is used to constrain the variation of the solution [62]. In case of more knowledge about the solution, one can replace the identity matrix $\mathbf{I}$ in $\mathbf{\Gamma}$ with a different one. For the application case of imaging with coda waves, Planès et al. [23], for example, use the discrete mesh's geometry information in a matrix containing an exponential correlation term between the discrete nodes.

Using the SVD representation of $\mathbf{A}$, Eq. 3.15 can be rewritten. Note that $\mathbf{\Gamma} = \alpha\mathbf{I}$ is already inserted in the following expression:

$$\mathbf{x} = (\mathbf{V}\mathbf{\Sigma}\mathbf{U}^T\mathbf{U}\mathbf{\Sigma}\mathbf{V}^T + \alpha^2\mathbf{I})^{-1}\mathbf{V}\mathbf{\Sigma}\mathbf{U}^T\mathbf{y} \tag{3.16}$$

Considering the orthogonality of the singular vectors, the expression can be further simplified as follows [63]:

$$\mathbf{x} = \sum_{i=1}^{r} \frac{\sigma_i \mathbf{u}_i^T\mathbf{y}}{\sigma_i^2 + \alpha^2}\mathbf{v}_i \tag{3.17}$$

This expression can be used to extract a filter function that helps to understand how the Tikhonov regularization works [63]:

$$\mathbf{x} = \sum_{i=1}^{r} f(\sigma_i^2)\frac{\mathbf{u}_i^T\mathbf{y}}{\sigma_i}\mathbf{v}_i \qquad \text{with } f(\sigma_i^2) = \frac{\sigma_i^2}{\sigma_i^2 + \alpha^2} \tag{3.18}$$

When looking at the filter function $f(\sigma_i^2)$, one can see that it is ≈ 1 for singular values much larger than the regularization factor α. The filter function is approximately zero for values much smaller than α. Since the singular values are in descending order, the Tikhonov regularization is thus damping the influence of the small singular vectors known to have a highly oscillating influence. This filtering is similar to another common regularization method, the truncated SVD that cuts small singular values and corresponding singular vectors with a Heaviside function. See Weber et al. [63] for a further comparison of how the two regularization methods can be expressed with filter functions.

3.4 L-Curve Method

As mentioned above, the biggest challenge with regularization is to find a good regularization parameter α. Hansen [60] introduces a method of determining the parameter for discrete ill-posed problems. In order to do so, the problem must be solved several times, and each time the parameter is varied. When plotting the residual sum of squares (RSS) of the solution $\|\mathbf{x}\|_2^2$ against the RSS of the residual $\|\mathbf{Ax}-\mathbf{y}\|_2^2$ in log-log scale, one obtains an L-shaped curve. Fig. 3.2 shows an exemplary L-curve for the laboratory experiments of Sec. 6.2. As one wants to obtain a small residual, the optimal result of α should

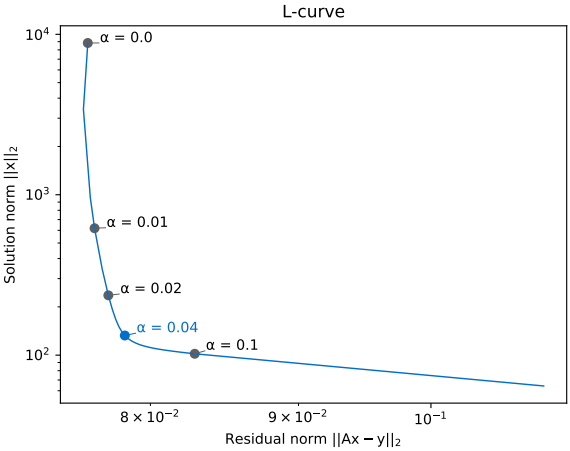

Figure 3.2: L-curve for the laboratory experiments of Sec. 6.2 evaluated at load step 8.

be as left as possible. The part of the L-curve going to the right is created by the penalty term taking over and limiting precise imaging. However, without regularization, the solution contains large oscillations that increase $\|\mathbf{x}\|_2^2$, which must also be avoided. Therefore, Hansen [60] describes the kink of the L-shape as an optimal choice. In case the kink of the L-shape is smooth, the point of maximum curvature is the recommended choice. In the L-curve of Fig. 3.2, this would be $\alpha = 0.04$.

3.5 Non-Linear Ill-Posed Problems

The previous explanations were based on the linear inverse problem of Eq. 3.5 where gradients are independent of the linearization point $\mathbf{x}_k$. For the non-linear case, the Taylor series approximation of Eq. 3.3 changes depending on the linearization point $\mathbf{x}_k$ and can be written as follows where the notation with x_k as a subscript of $\mathbf{A}$ indicates that it is the gradient at $\mathbf{x}_k$.

$$f(\mathbf{x}) \approx f(\mathbf{x}_k) + \mathbf{A}_{x_k}(\mathbf{x} - \mathbf{x}_k) \tag{3.19}$$

When inserting into the residual formulation of Eq. 3.2 and minimizing with the least-squares formulation of Eq. 3.7, one obtains

$$\min_{\mathbf{x}\in\mathbb{R}^n}(\|\mathbf{y} - f(\mathbf{x}_k) - \mathbf{A}_{x_k}(\mathbf{x} - \mathbf{x}_k)\|_2^2) \tag{3.20}$$

With the zero setting of the gradient as in Eq. 3.8, one obtains the normal equation

$$\mathbf{A}_{x_k}^T\mathbf{A}_{x_k}(\mathbf{x} - \mathbf{x}_k) = \mathbf{A}_{x_k}^T(\mathbf{y} - f(\mathbf{x}_k)) \tag{3.21}$$

that leads to the explicit solution known as a Gauss-Newton iteration step:

$$\mathbf{x}_{k+1} = \mathbf{x}_k + (\mathbf{A}_{x_k}^T\mathbf{A}_{x_k})^{-1}\mathbf{A}_{x_k}^T(\mathbf{y} - f(\mathbf{x}_k)) \tag{3.22}$$

For the linear case $\mathbf{x}_k$ is zero and $f(\mathbf{x}_k = \mathbf{0}) = \mathbf{0}$ is assumed. Applying these simplifications at Eq. 3.22, one obtains the solution for the linear problem of Eq. 3.10. The similarity is due to the linearization of the non-linear function $f(\mathbf{x})$.

For a general non-linear problem, one can apply the same regularization techniques as in Sec. 3.3. Thereby, it is essential to first linearize the problem and then regularize by penalizing the change of the solution $\mathbf{x} - \mathbf{x}_k$ in the iteration step. Otherwise, the solution is determined with the first iteration step [64].

$$\min_{\mathbf{x}\in\mathbb{R}^n}(\|\mathbf{y} - f(\mathbf{x}_k) - \mathbf{A}_{x_k}(\mathbf{x} - \mathbf{x}_k)\|_2^2) + \|\mathbf{\Gamma}(\mathbf{x} - \mathbf{x}_k)\|_2^2) \tag{3.23}$$

By setting the gradient of the argument in Eq. 3.23 to zero in order to solve for the extreme point, one can again solve for an explicit solution $\mathbf{x}_{k+1}$. With the inverse covariance matrix $\mathbf{C}_X^{-1}$ instead of $\mathbf{\Gamma}^T\mathbf{\Gamma}$, one obtains the following expression:

$$\mathbf{x}_{k+1} = \mathbf{x}_k + (\mathbf{A}_{x_k}^T\mathbf{A}_{x_k} + \mathbf{C}_X^{-1})^{-1}\mathbf{A}_{x_k}^T(\mathbf{y} - f(\mathbf{x}_k)) \tag{3.24}$$

With a scalar multiple of the identity matrix chosen for $\mathbf{C}_X^{-1}$, as done in this thesis, Eq. 3.24 is known as Levenberg–Marquardt algorithm [64–66]. This solving algorithm is later applied in the practical applications presented in this thesis (cf. Ch. 8). With $\mathbf{C}_X^{-1} = \alpha^2\mathbf{I}$ and the SVD of $\mathbf{A}$, the Levenberg–Marquardt algorithm can be written as follows:

$$\mathbf{x}_{k+1} = \mathbf{x}_k + \sum_{i=1}^{r}\frac{\sigma_i\mathbf{u}_i^T(\mathbf{y} - f(\mathbf{x}_k))}{\sigma_i^2 + \alpha^2}\mathbf{v}_i \tag{3.25}$$

For the sake of completeness and in order to highlight the potential for improvement, a further generalization is mentioned here. Next to knowledge about the solution which the covariance matrix of the model $\mathbf{C}_X$ contains, further knowledge about correlation in the measurement data can be respected. This is done by weighting the rows of $\mathbf{A}$ with the inverse covariance matrix of the measurement data $\mathbf{C}_Y^{-1}$. Based on Tarantola et al. [67], this leads to the following objective function that is minimized:

$$\begin{gathered}\|\mathbf{y} - f(\mathbf{x}_k) - \mathbf{A}_{x_k}(\mathbf{x} - \mathbf{x}_k)\|_Y^2 + \|\mathbf{x} - \mathbf{x}_k\|_X^2 = \\ [\mathbf{y} - f(\mathbf{x}_k) - \mathbf{A}_{x_k}(\mathbf{x} - \mathbf{x}_k)]^T \mathbf{C}_Y^{-1} [\mathbf{y} - f(\mathbf{x}_k) - \mathbf{A}_{x_k}(\mathbf{x} - \mathbf{x}_k)] + \\ (\mathbf{x} - \mathbf{x}_k)^T \mathbf{C}_X^{-1} (\mathbf{x} - \mathbf{x}_k)\end{gathered} \tag{3.26}$$

Here $\|\cdot\|_Y^2$ and $\|\cdot\|_X^2$ refer to the squared Euclidean norm weighted with $\mathbf{C}_Y^{-1}$ and $\mathbf{C}_X^{-1}$, respectively. When solving the minimization problem by setting the gradient to zero, one gets the following solution for $\mathbf{x}_{k+1}$, which is also referred to as generalized Tikhonov regularization [62]:

$$\mathbf{x}_{k+1} = \mathbf{x}_k + (\mathbf{A}_{x_k}^T \mathbf{C}_Y^{-1} \mathbf{A}_{x_k} + \mathbf{C}_X^{-1})^{-1} \mathbf{A}_{x_k}^T \mathbf{C}_Y^{-1} (\mathbf{y} - f(\mathbf{x}_k)) \tag{3.27}$$

As mentioned above, $\mathbf{C}_Y$ is the covariance matrix of the measurement data. A correlation between different measurements is neglected in this thesis. For the application case of CWI, Planès et al. [23] calls this assumption reasonable for distant sensors and non-overlapping measurement time windows. $\mathbf{C}_Y$ is a diagonal matrix for non-correlated measurements. If it is the identity matrix, it is also referred to as the Markov estimator that yields the best linear unbiased estimate [68]. However, with larger or smaller values, specific measurements could be over- or under-weighted depending on the confidence in its accuracy, for example. Planès et al. [23], weights the rows of $\mathbf{A}$ with the magnitude of the measurement value. Another possibility for the CWI application in this thesis would be a relation to the source-receiver distance, as there is a larger modeling error for short source-receiver distances and, thus, most likely a bigger discrepancy to measurement values.

To conclude this section, the Gauss-Newton algorithm for a least-squares problem is compared to the standard Newton method for non-linear problems. For solving an optimization problem, one needs the Jacobi matrix $\mathbf{A}$ with first-order derivatives and the inverse Hessian matrix $\mathbf{H}$. The iteration step for finding an extreme point with the Newton method then looks as follows:

$$\mathbf{x}_{k+1} = \mathbf{x}_k - \mathbf{H}_{x_k}^{-1} \mathbf{A}_{x_k} \tag{3.28}$$

Comparing the Newton step to the Gauss-Newton step of Eq. 3.22, one can see that with the transformation of the problem to a least-squares one, the Hessian matrix $\mathbf{H}$ with second order derivatives, that are usually difficult to obtain, is approximated with $\mathbf{A}_{x_k}^T \mathbf{A}_{x_k}$. The first order derivatives $\mathbf{A}_{x_k}$ of the Newton method become $\mathbf{A}_{x_k}^T f(\mathbf{x}_k)$.

3.6 Constrained Optimization

When searching for the solution of the inverse problem, one can introduce the assumption that values of the solution field can only be positive, so $\mathbf{x} \geq \mathbf{0}$. This special type of a constrained least-squares problem is referred to as non-negative least squares (NNLS):

$$\min_{\mathbf{x}\in\mathbb{R}^n} \|\mathbf{y} - \mathbf{A}\mathbf{x}\|_2^2 \qquad \text{subject to } \mathbf{x} \geq \mathbf{0} \tag{3.29}$$

Lawson et al. [69] developed an active-set method for solving an NNLS problem. The method transforms, when activated, the inequality constraint (here $x \geq 0$) into an equality constraint (here $x = 0$) that is easier to handle. A generalization of the NNLS is the bounded-variable least squares (BVLS) algorithm by Stark et al. [70]. It extends the non-negativity constraint to a more general one with a lower and upper bound: $l \leq x \leq u$. The two algorithms are introduced and published as Fortran implementations. In this thesis, the programming language Python limited required modifications such as adding a regularization term, and thus, two different implementations are used, presented in the following.

3.6.1 Projected Gradient Descent Method

The projected gradient descent method is a simple algorithm directly applicable to the gradient descent algorithm of Eq. 3.24 to ensure all parameters x are in the feasible domain. In the first step of the algorithm, the unconstrained gradient descent iteration step of Eq. 3.24 is performed. In the second step, values outside the feasible domain are projected back onto it. For the non-negativity constraint, this is done by truncating negative values and setting them to zero in each iteration step. The complete algorithm is also shown in the flowchart in Fig. 3.3. It is used in the computational model updating of a structural-mechanical model in Sec. 8.2.

3.6.2 Trust Region Reflective Algorithm

For imaging with coda waves, an algorithm introduced by Branch et al. [71] as "a subspace, interior, and conjugate gradient method for large-scale bound-constrained minimization problems" is used. Compared to classical gradient methods as steepest descent, conjugate gradient methods converge in fewer iteration steps but at the cost of more computational effort during each step. For gradient descent methods such as the used steepest descent, the number of iterations is commonly proportional to the condition number $\kappa(A)$, whereas, for conjugate gradient method, it is typically determined by a square root of the condition number, i.e., is much faster [72]. With huge condition numbers for the inverse problem, the conjugate gradient method can significantly reduce computation times. Due to its high mathematical complexity, a modified version of the `lsq_linear` algorithm of the open-source package for scientific programming with Python, `scipy`[1], is used. In

[1] github.com/scipy

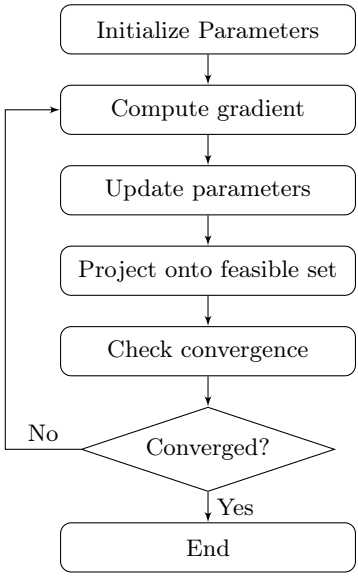

Figure 3.3: Flowchart of the Projected Gradient Descent Method.

its documentation, the algorithm is described as follows: "The algorithm iteratively solves trust-region subproblems augmented by a special diagonal quadratic term and with trust-region shape determined by the distance from the bounds and the direction of the gradient. This enhancements help to avoid making steps directly into bounds and efficiently explore the whole space of variables. To further improve convergence, the algorithm considers search directions reflected from the bounds. To obey theoretical requirements, the algorithm keeps iterates strictly feasible. [...] For large sparse Jacobians, a 2-D subspace approach of solving trust-region subproblems is used [71, 73]. The subspace is spanned by a scaled gradient and an approximate Gauss-Newton solution delivered by `scipy.sparse.linalg.lsmr`. [...] The algorithm works quite robust in unbounded and bounded problems [...]."[74]

3.7 Remarks on the Implementation

The projected gradient decent method is manually implemented in Python. The trust region reflective algorithm of Sec. 3.6 is a `scipy` implementation For the linear problem where $\mathbf{A}$ is independent of $\mathbf{x}$, numerically expansive computations of the projected gradient descent method as inverting or SVD of $\mathbf{A}$ only need to be performed once, which is advantageous and speeds up computations during each iteration step if computed in advance. Two modifications have been manually implemented for the trust region reflective algorithm. One is the addition of a regularization by including the damping

term of the Tikhonov regularization in the algorithm. The second modification is an enforcement of iterations for the algorithm. As it is originally a linear solver, a solution for the first iteration step in the feasible domain is regarded as optimal and a stop criterion. This check was modified to enforce further iterations that significantly improved the result. Fig. 3.4 compares the two algorithms at an application of the laboratory experiment of Sec. 6.2 at load step 8. One can see that the obtained solutions in blue appear very similar. Also, the obtained residual and solving times are very comparable. Thus, both methods are comparable and deliver good results.

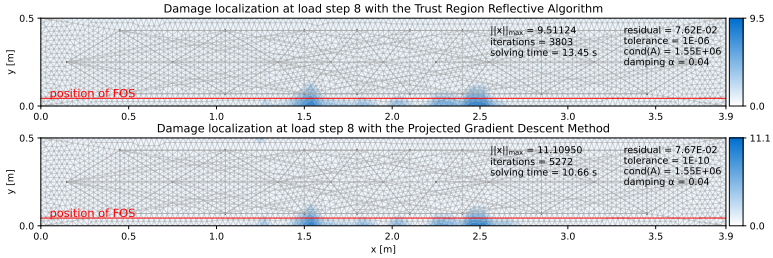

Figure 3.4: Comparison of the result (in blue) for the two different solving algorithms.

Chapter 4

Basics of Coda Wave Interferometry

4.1 Overview on Non-Destructive Testing and Structural Health Monitoring

Monitoring of structures is an essential part of guaranteeing their safety. In Germany, the national code DIN 1076 [2] defines the review of the actual condition of the bridge structure to ensure its stability and safe use for traffic. Inspections can be divided into different levels. The most common method is a visual inspection that only provides surface information. Different NDT methods exist that allow further structure evaluation. The applicability strongly depends on the structures' material. The majority of built infrastructure is made out of reinforced concrete. Compared to a homogenous material such as steel, concrete is very complex due to an inhomogeneous mix of aggregates, cement, and steel reinforcement. For concrete structures, established NDT methods are electrical methods, ground penetrating radar, impact-echo testing, and ultrasonic testing, to name a few. A good overview of NDT methods can be found in Lee et al. [75] and McCann et al. [76] and for ultrasonic methods in Schiebold [77]. The opposite of NDT methods are destructive methods such as core sampling. Non-destructive and destructive testing methods have in common that the result is typically on-demand local information. Thus, inspecting large structures such as bridges is costly and typically does not detect sudden events or trends. A permanently installed monitoring is thus desirable and addressed by the field of SHM. Standard fixed sensors measure displacements, strains, accelerations, and environmental conditions such as temperature and humidity. Also, some of the NDT methods are applicable for permanent monitoring, e.g., acoustic emission and ultrasound methods. An overview of used sensors and their associated algorithms can be found in Yoder et al. [78]. The typically obtained information is global,

e.g., eigenmode information. Local NDT methods, which sometimes work in a sensor network, can be extended to the entire structure but usually require an unfeasible number of sensors due to the small sensing areas. Next to the size of structures, environmental variations are a significant challenge for permanent monitoring systems. Environmental variations can significantly influence the measured data depending on the measurement technology. The main challenge is to distinguish natural variations due to the environment from permanent ones that are caused by damage.

In order to ensure structural integrity and safety, all SHM methods aim to detect damages. Damage here can be described as irreversible changes, but there are still different levels to distinguish. Worden et al. [79] propose the following taxonomy:

- **Defect:** Inherent in the material and statistically all materials will contain a known amount of defects. This means the structure will operate optimally if the constituent materials contain defects.
- **Damage:** When the structure is no longer operating in its ideal condition but can still function satisfactorily, i.e., in a sub-optimal manner.
- **Fault:** When the structure can no longer operate satisfactorily. If one defines the quality of a structure or system as its fitness for purpose, it suffices to define a fault as a change in the system that produces an unacceptable reduction in quality.

With this classification, the aim is to detect faults and damage that could lead to a fault. The detection of damage can be distinguished into different levels. Established SHM applications are often limited to localization or classification of the following classification by Worden et al. [79] and Rytter [80]:

- **1. Detection:** The method gives a qualitative indication that damage might be present in the structure.
- **2. Localization:** The method gives information about the probable position of the damage.
- **3. Classification:** The method gives information about the type of damage.
- **4. Assessment:** The method gives an estimate of the extent of the damage.
- **5. Consequence:** The method offers information about the structure's safety, for example, estimates residual life.

4.2 Overview on Concrete

Concrete is a highly heterogeneous composite of cement, aggregates, and water. After a hydration process in which water and cement form a matrix around the aggregates, a hard and resistant material is created that can be seen in Fig. 4.1. The properties of concrete strongly depend on several factors,

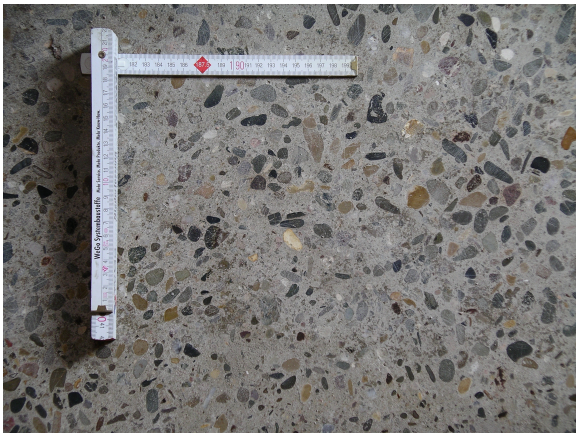

Figure 4.1: Structure of concrete [81].

such as the cement used, the water-cement ratio, and the additives used. The compressive strength of concrete is typically more than ten times higher than its tensile strength. Therefore, concrete is usually combined with steel reinforcement. Compressive strengths of concrete range from $10\,\mathrm{N/mm^2}$ to over $100\,\mathrm{N/mm^2}$. With increasing compressive strength, the average Young's modulus increases from $27000\,\mathrm{N/mm^2}$ to $45000\,\mathrm{N/mm^2}$. The used aggregates can also have significant differences in size. Fine ones typically have diameters $< 4\,\mathrm{mm}$ while coarse ones can have 1-3 cm diameters. Reinforcement bars also often have diameters of 1-3 cm and in the case of pre-tensioning, this can further increase. While the distribution of aggregates is uniform within the material, the distribution of reinforcement strongly depends on the position in the material. Thus, not only can the characteristics of different concrete specimens strongly differ, but also, within one concrete specimen, the local cross-sections can have large differences. It is, therefore, very challenging to investigate existing concrete structures with NDT technologies.

Under load, concrete deforms. For reinforced concrete, two states differ: before and after cracking. Until the concrete tensile strength is reached, the material behaves linear-elastically. This means that deformations are fully reversible. In this domain, stress and strain are linearly related by Hookes law. Once the tensile strength is exceeded, the material begins to crack, and the steel reinforcement is activated to carry the tensile forces. Cracks are typically irreversible changes in the medium but not necessarily unwanted damage. In an economical structure design, cracking is often planned. However, cracks reduce the protection of the reinforcement, making the material more vulnerable. An overview of crack classifications and the influence of cracks on ultrasound can be found in Wolf [82].

4.3 Overview on Wave Properties

The fundamental properties of a wave are wavelength λ, frequency f and wave speed c that are related as follows:

$$\lambda = \frac{c}{f} \tag{4.1}$$

Depending on the particle movement, one can distinguish two main types of body waves shown in Fig. 4.2. One is compressional waves with body motion

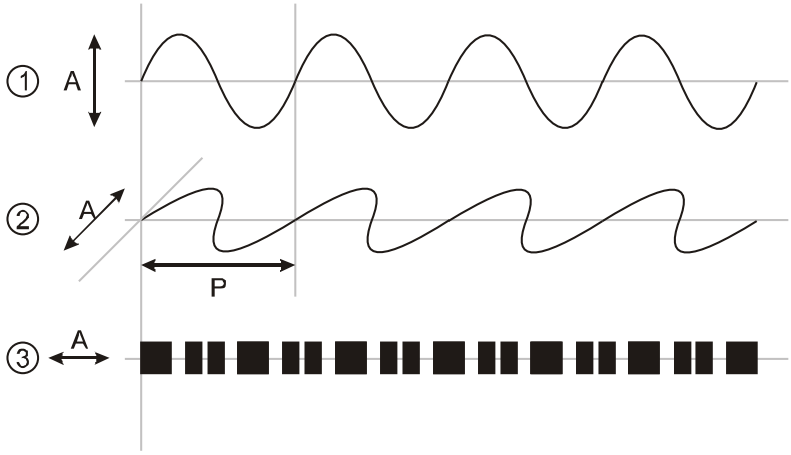

Figure 4.2: Types of body waves: 1. and 2. shear waves (S-waves), 3. compressional wave (P-waves)[83].

in the longitudinal direction, referred to as primary waves (P-waves), and the other is shear waves with particle motion in the transversal direction, referred to as secondary waves (S-waves). Next to body waves, there are also different types of surface waves, with the Rayleigh waves being the most important ones. The used transducers in the presented experiments emit energy as P-waves. However, mode conversion into an S-wave or vice versa is possible during a scattering event. After many scattering events when a diffuse wave field is obtained, the P-wave energy and S-wave energy ratio is as follows [84]:

$$\frac{E_p}{E_s} = \frac{1}{2}\left(\frac{c_s}{c_p}\right)^3 \tag{4.2}$$

The wave speed in concrete depends, among other factors like cement paste, aggregates, and water ratio, significantly on the concretes Young's modulus. Typical are wave speeds of the P-wave in concrete in the range of 3500 m/s - 4500 m/s. Also, P-waves are approximately 1.7 times faster than S-waves.

Consequently, this means that S-waves contain approximately 90 % of the energy in the diffuse wave field.

Next to the properties of Eq. 4.1, the sound pressure p is another fundamental property of ultrasound. In a wave signal, the sound pressure p is represented by the amplitude. In the free field, the sound pressure of body waves decreases proportionally to the second power of the distance r to a point source (spherical divergence):

$$p \sim \frac{1}{r^2} \tag{4.3}$$

The wave is reflected or refracted on boundaries and heterogeneities in the medium. The ratio of reflection and transmission depends on the difference in acoustic impedance Z of the materials that depend on the wave speed c and material density ρ:

$$Z = c * \rho \tag{4.4}$$

The acoustic impedance is related to the sound pressure by the velocity v of the particles around their rest position:

$$Z = \frac{p}{v} \tag{4.5}$$

In addition to the spherical divergence, which reduces the sound pressure, the ultrasound is also attenuated. Attenuation consists of scattering, intrinsic absorption, and diffraction. Often, scattering is the dominant reason for attenuation [85]. The scattering behavior of ultrasound is typically investigated in polycrystalline media [86–89]. One can differ from three types of scattering that depend on the ratio of wavelength λ and scatterer sizes d [90]:

- Rayleigh scattering: $\lambda/d >> 1.0$
- Stochastic scattering: $\lambda/d \approx 1.0$
- Diffusive scattering: $\lambda/d < 1.0$

Ultimately, the scattering behavior and, thus, the attenuation is frequency-dependent and increases significantly with the frequency. Different defined scattering regimes for concrete are given in the following section.

4.4 Properties of the Coda Wave in Concrete

Coda waves travel in heterogeneous media and are backscattered by inhomogeneities. Historically, they are typically investigated in seismology [91, 92]. Heterogeneities distributed uniformly in the earth's crust backscatter earthquake waves, creating a signal containing a diffuse tail. This tail that typically starts after the direct, ballistic wave is called coda. In terms of the multiple uniformly distributed heterogeneities, concrete has many similarities to the earth's crust. With a scaling of the frequency to the ultrasonic regime due to the different dimensions, the evaluation of coda waves is thus transferable to concrete. The wave is scattered mainly by aggregates, pores, and

reinforcement in concrete. As previously mentioned, the scattering behavior is frequency-dependent. Planès et al. [4] define four overlapping scattering regimes for ultrasound in concrete. The delineation is done by the average number of scattering events of a wave from the source to the receiver.

- stationary wave regime: $f < 20kHz$ (no significant scattering)
- simple scattering regime: $10kHz < f < 150MHz$ (one scattering event on the way from source to receiver)
- multiple scattering regime: $100kHz < f < 1MHz$ (multiple scattering events on the way from source to receiver)
- attenuation regime: $f > 500kHz$ (not applicable to large scale concrete structures)

The multiple scattering regime is the most important since coda waves are characterized by multiple backscattering at heterogeneities. Planès et al. [4] describe that in received multiple scattered signals, the direct wave is highly attenuated and sometimes no longer visible. In contrast, the direct wave of signals in the simple scattering regime is visible. However, the simple scattering regime signals often contain a coda part after the ballistic part. Experiments presented in Ch. 6 use signals with a central frequency of 60 kHz. Two signals of the experiment presented in Sec. 6.2 that have the same source but different travel distances in the medium are shown in Fig. 4.3. For the

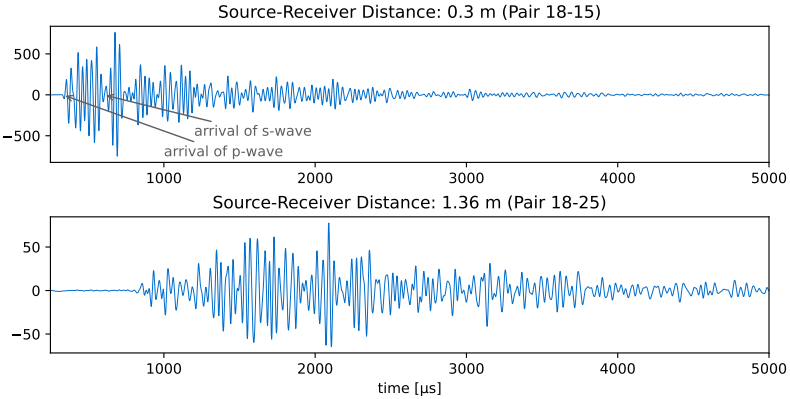

Figure 4.3: Comparison of two 60 kHz signals with different travel distances in the medium.

signal with the short travel distance of 0.3 m, one can see peaks in the signal that indicate the arrival of the direct wave. Two arrivals are visible: the one of the p-waves (first) and the one of the s-waves (second). After the first peaks, there is a long diffuse tail called the coda part. Thus, there must also be multiple backscatterings at this short source-receiver distance. With

increasing source-receiver distance, as in the bottom signal of Fig. 4.3 (pair 18-25), the scattering events increase, and the direct wave is no longer visible. According to Planès et al. [4], the frequency of 60 kHz with wavelengths of $\lambda_{p-wave} \approx 0.07m$ and $\lambda_{s-wave} \approx 0.04m$ belongs to the simple scattering regime. However, the evaluation of the waveforms in Fig. 4.3 suggests that travel distances in the medium play a significant role in the scattering characterization.

This goes along with two measures for describing the scattering behavior: the scattering mean free path l, and the transport mean free path l^*. The scattering mean free path describes the distance between two successive scattering events and thus is a measure of the heterogeneity of the material. The transport mean free path describes the distance after which the wave has lost the memory of its initial direction of propagation. After this distance, the wave propagation is no longer directional but a superposition of countless random paths that create a diffuse spread of the wave field. In case scattering is isotropic, the two measures are the same. In case the wave has traveled less than the transport mean free path, the direct wave parts are visible as that is the part containing information about the initial direction of propagation. The two signals of Fig. 4.3 suggest that this experiment's transport mean free path must lay between the two evaluated source-receiver distances. Further investigations on this problem are performed in Sec. 6.2.4.2.

Most applications of coda waves in concrete use frequencies in the range of 100 kHz to 1 MHz, which is in the multiple scattering range. In this thesis, the multiple scattering-based techniques are applied to signals with a central frequency of 60 kHz as they also show a diffuse coda part created from multiple backscattering. The smaller frequency also leads to reduced attenuation. Thus, transmitting the signal over longer source-receiver distances is possible, which is beneficial for the application in large concrete structures.

Due to the diffuse spreading of the ultrasound into the concrete, the coda part is also very sensitive to changes in the medium because a change affects not only the tiny part of the ballistic wave but multiple random wave paths that interfere with a change. Thus, little changes have increased visibility in the signal.

4.5 Evaluation of Coda Waves

The comparison to a reference measurement is essential for evaluating coda waves. Therefore, the NDT method with coda waves is typically referred to as coda wave interferometry (CWI). The comparison to a reference cancels influences on the scattering of a signal by geometric boundaries, aggregates, and pores of the concrete and reinforcement bars. This means coda signals with their diffusive tail can be reproduced as long as no external influences affect the specimen. The diffuse tail of the signal is especially sensitive to tiny changes because many random paths of the wave cross a small change and superpose in the tail, creating amplified visibility. The CWI is multi-layered, and the parameters examined are discussed in more detail below.

4.5.1 Cross Correlation

The actual measurement value in CWI is a cross-correlation coefficient (CC) for a time frame of length T in the signal φ at time t that is computed as follows [93, 94]:

$$CC(t) = \frac{\int_{t-T/2}^{t+T/2} \varphi_{ref}(t)\varphi(t)\,dt}{\sqrt{\int_{t-T/2}^{t+T/2} \varphi_{ref}^2(t)\,dt \int_{t-T/2}^{t+T/2} \varphi^2(t)\,dt}} \tag{4.6}$$

For two identical signals, the CC is one. The larger the changes, the lower the CC. When putting the focus on changes in the waveform, the decorrelation coefficient (DC) is investigated that is closely related to the CC, in fact:

$$DC = 1 - CC \tag{4.7}$$

4.5.2 Evaluated Time Frames

The time frames of length T for evaluating a CC or DC can be divided into two types. One is the overall (long) time frame, and one is successive shorter ones for evaluation of a DC development (cf. Fig. 4.4).

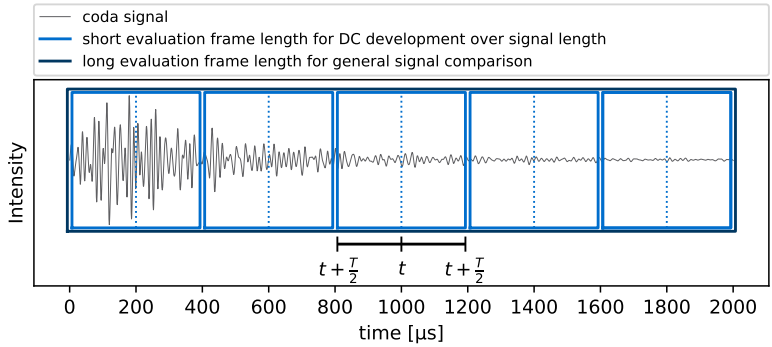

Figure 4.4: Exemplary time frames for the correlation evaluation of a coda signal.

The coda technology primarily uses the diffuse tail of a signal. Thus, the overall time frame should be long enough. With decreasing signal intensity, the signal-to-noise ratio, however, increases, and the overall signal length should be limited. The shorter time frames for the DC development evaluation should be chosen long enough to avoid substantial deviations but short enough to be able to document development.

4.5.3 Phase Shifts

One can generally distinguish two types of changes in the coda signal. One is a phase shift of the signal that comes from a change of the wave speed δv, and one is a change in the waveform that typically comes from new scatterers. As described later in Sec. 4.6, there are multiple reasons for a change in the wave speed. With a pure change of the wave speed and no waveform deformation, the signal changes are, in theory, revertible by stretching the signal along the time axis with a factor ε [95]. The stretching technique assumes that with the linear increasing time of the signal in the specimen, the signal's phase shift also increases linearly. With a reduction of the wave speed, e.g., due to compression, the stretching can also be negative.

The stretching factor ε is obtained by stretching the signal multiple times, and the ε that creates the largest CC is chosen as the best stretching factor for the measurement. In the presented work, each signal is stretched in successive short time frames, and therefore, one can document a stretching development over the signal's length. Figure 4.5 visualizes the phase shifts over the signal's length that is linearly interpolated within the evaluation frames.

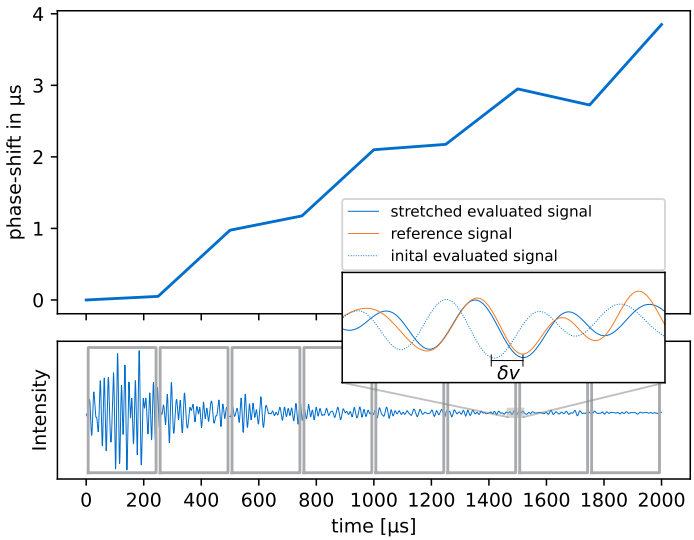

Figure 4.5: Evaluated phase-shift over the signal length.

4.5.4 Decorrelation Development

Next to the phase shift of the signal, the waveform itself can also change. This change is typically measured with the DC. Due to the scattering in the medium, a certain point is passed not just once by the wave but multiple

times by randomly scattered wave paths. Thus, adding a new scatterer into the medium, e.g., due to a crack, does not change the signal at just one position but several positions. These multiple waveform changes in the signal create a characteristic DC development over the signal's length. This DC development is shown in Figure 4.6 and tends to increase in later parts of the signal because more random wave paths cross the new scatterer and create various interferences with other wavefronts that all add up to an increased decorrelation. This superposition also explains the high sensitivity of CWI to tiny changes. The described increasing development of DC is very characteristic of the relative position of the new scatterer to the source-receiver pair and is modeled with sensitivities of the coda wave (cf. Sec. 5.2.1).

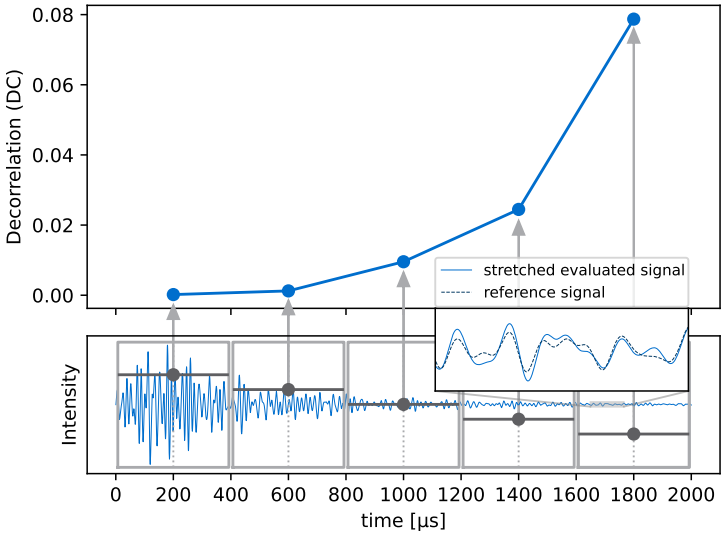

Figure 4.6: Exemplary decorrelation evaluation of measurement in five consecutive non-overlapping windows of length 400 μs after the arrival of the first wave (time-of-flight (tof)).

4.6 Influences on Coda Waves

When applying CWI as a SHM, it is important to understand influences on the signal that creates decorrelation. Especially due to the high sensitivity of coda waves to small changes, environmental variations can significantly change the coda signal. Below is an overview of the most important influences:

Temperature With significant variations on a daily and yearly scale, temperature has an enormous environmental influence on concrete structures. With increasing temperature, the wave speed of ultrasound increases.

Since the wave speed is not obtained from a time-of-flight evaluation but with CWI that analyses the little phase-shifts within the signal, the sensitivity of detecting temperature changes with CWI is immense. This vast potential is documented by several studies [10, 96, 97] investigating the effect of temperature on coda waves. With CWI, even changes in the magnitude of one degree become visible in the later parts of the coda waves. Wang et al. [98] compares different studies that evaluate the phase shifts from temperature. Results show significant variations in the relation of phase shifts to temperature change. The main factors are probably the significant variation of the concretes Young's modulus described in Sec. 4.2 and different source-receiver distances and specimen dimensions. The temperature development in the specimen is also highly non-linear, which means that the temperature variation can affect similar source-receiver combinations in the same concrete structure differently.

Moisture The moisture change in concrete is closely coupled with temperature change. Ju et al. [11] investigates the effect of moisture content in a cement mortar on the ultrasound velocity. The study shows that the wave velocity slightly increases with increasing moisture, and the signal attenuation also increases.

Stress Changes In elastic materials, the ultrasound velocity is related to the stresses in the medium. The relation is called the acoustoelastic effect discovered by Brillouin [99]. The effect describes a decrease in ultrasound velocity with increasing pressure and, vice versa, faster ultrasound velocities with increasing tensile stress. The acoustoelastic effect involves a non-linear extension of the constitutive relationship between the mechanical stress and the resulting strain. See, e.g., Lillamand et al. [8] and Guyer [100] for further information on non-linear elasticity. The effects of stress on the ultrasound velocity are material-specific and described with material constants that depend on the Lamé and Murnaghan coefficients. In a controlled environment, CWI allows recovering the relative velocity change dv/v with a precision of 10^{-5} according to Larose et al. [7]. This precision allows structures to be monitored at a stress level well before cracking. One obtains a near-linear relation at low-stress levels when plotting the ultrasound signal's relative velocity change dv/v against the mechanical stress change. From the slope of the linear regression of this relationship, one can obtain the acoustoelastic constants of the material. For concrete, values from the literature differ in a wide range. Planès et al. [4] reports a range of 0.1×10^{-3} to 2×10^{-3} MPa^{-1} for healthy concrete. Studies [101–104] also find that the acoustoelastic constant increases with increasing damage. Thus, with good calibration, the acoustoelastic constant could be a tool to detect altered concrete. However, Zhang et al. [104] also report increases of the acoustoelastic constant with load cycles. Direct damage detection from obtained acoustoelastic constant is problematic for a long-term SHM application, where temperature also affects the relative velocity change.

Cracks Cracks are cuts in the medium of micro- or macroscopic scale. There are different types of cracks, which are strongly related to the cause of cracking. Microcracks are not visible to the naked eye. They can form as a natural part of the cement hydration process but also due to thermal or mechanical loading. Under mechanical loading, one can observe a memory effect of concrete (Kaiser effect). It describes the effect of additional microcracking when stresses exceed the historical maximum [6]. Under pressure, it can also be observed that micro-cracks close [105]. One can distinguish bond, mortar, and aggregate cracks depending on the location. Microcracks connect to macrocracks with excitation of the concrete tensile strength or under dynamic loading. However, macrocracks are not necessarily problematic depending on the reinforced concrete exposure. In an economical design of the structural members, steel reinforcement is used to bridge the cracked parts. Nevertheless, it is essential to monitor the development of micro- and macrocracks. Wolf [82] describes three main effects of cracks on the ultrasound signal: A change in ultrasound velocity, sound pressure, and scattering behavior. The effects of the acoustoelastic effect usually superpose with the effects on the ultrasound velocity. Shortly before macrocracks appear, Shokouhi et al. [106] report a decrease in the ultrasound velocities. Regarding sound pressure, studies [106, 107] report a loss in amplitude with increasing damage. With cracks being a discontinuity in the medium, each new crack marks a new scatter, and thus, the overall scattering behavior changes. Larose et al. [12] have shown that locating small changes in a multiple scattering such as concrete is possible. The localization is based on a waveform distortion due to the additional scatterers that can be measured with a DC evaluation of consecutive time frames within the signal. As described in Sec. 4.5.4, the DC increases towards later parts of the signal. The increase is very characteristic of the relative position of the new scatterer to the source-receiver pair and is modeled with sensitivities of the coda wave (Sec. 5.2.1). With an equivalent model, locating the small changes is possible.

4.7 Signal Processing for Damage Localization

The signals themselves are processed before applying CWI on coda signals. In practical applications, a measurement is typically repeated several times within a few milliseconds, and the average signal is used. This is done to improve the reproducibility of the coda signals and increase the signal-to-noise ratio by reducing white noise. The next step filters specific frequencies with a bandpass filter to reduce the signal's noise. Also, the start of the signal is dependent on the travel distance between the source and the receiver. Thus, the start of the signal is cut off depending on the estimated time-of-flight (tof) of the signal. After this constant signal processing, the CWI is performed.

As mentioned above, there are various influences on a coda signal. With a focus on damage localization, influences from temperature, moisture, and

the acoustoelastic effect are regarded as noise to be filtered. These influences mainly create a phase shift due to ultrasound velocity changes. Due to typically inhomogeneous changes in temperature and stress over the specimen domain, there can be variations in the phase shifts. Typically, it is assumed that the phase shift increases linearly and can be compensated by stretching the signal. With several consecutive time-frames for stretching, it is also possible to compensate for non-linear developments of the phase-shift over the signals' length (cf. Sec. 4.5.3). After stretching, it is assumed that all effects that affect the ultrasound velocity are filtered out, which means only influences that distort the signal remain. Thus, in theory, only the effects of cracks on the signals' scattering behavior remain after stretching.

4.8 Used Hardware for Coda Waves

For CWI, ultrasound transducers are used as source and receiver. The typical type of application for ultrasound used for CWI is a surface mounting of transducers. Niederleithinger et al. [108] describes three substantial disadvantages of the surface installation. Namely, there are difficulties in a constant coupling over time, the significant influence of external effects such as temperature, and the danger of harm in a permanent field installation. The authors thus use sensors developed by Acoustic Control Systems, Ltd. (ACS, Moscow, Russia) in cooperation with the Bundesanstalt für Materialforschung und -prüfung (BAM) that are shown in Fig. 4.7 and also used the experiments presented in this thesis. The sensors contain a hollow piezoceramic cylinder

Figure 4.7: Photo of the used embedded ultrasound transducer [108].

of 20 mm diameter and 35 mm length that converts the electronic signal into an ultrasonic wave. Together with metallic clips at the piezo's ends, the total length of the cylinder-shaped transducer is 75 mm. The embedded installation is ideally done before casting the concrete. In this work's laboratory experiments, the sensors are attached to the reinforcement with 3D-printed plastic clips that ensure a safe mounting position. It is also possible to install sensors at existing structures. For this purpose, core drillings are made, sensors are

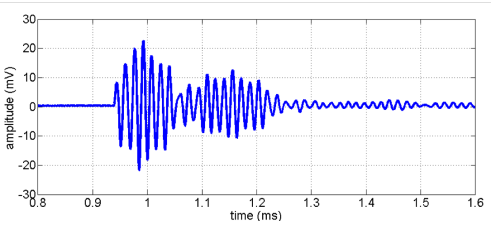

Figure 4.8: Response of the transducer to a short electrical impulse ($2\,\mu$s), recorded by a second, identical one with no distance in between them [108].

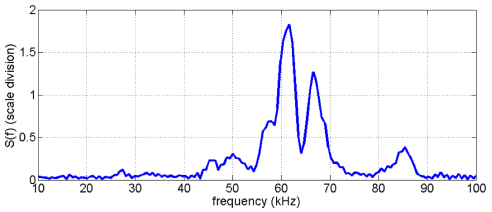

Figure 4.9: Frequency spectrum of signal from Fig. 4.8 [108].

inserted, and the holes are filled with grout. Further information on the installation and detailed signal characterization can be found in Niederleithinger et al. [108]. For this work, the characterization of the signal with a description of the excitation in time and frequency domain shown in Fig. 4.8 and Fig. 4.9 is sufficient. Despite the short excitation of $2\,\mu$s, the signal in Fig. 4.8 shows a long reverberation. Also, the frequency domain shows several peaks, with the most prominent one around 62 kHz. For CWI, the lack of sharp cuts in the time or frequency domain is unproblematic. For CWI, the most essential requirement of the ultrasound transducers is excellent signal reproducibility over a longer period, which is the case for the used sensors.

At this point, some simplifications in the numerical modeling of the sensors should also be pointed out. Despite the cylindric shape with a length of 75 mm, the transducers are treated as point sources in the numerical models. Also, the simulations neglect any directivity pattern and assume a uniform signal spread in all directions. The signal is furthermore referred to as a 60 kHz signal.

The discussion on the hardware used for reference measurements is kept short as it is specific for each experiment. A good overview of the used strain measurement techniques for reinforced concrete structures is given by Clauß et al. [109], who also performed the experiments of Sec. 6.2.

Chapter 5

Finite Element Based Imaging with Coda Waves

Parts of this chapter are taken from Grabke et al. [110].

5.1 Simulation of Coda Waves

Describing observed measurements with a model is generally required for successful damage localization. Since the measurements come from a signal processing of coda waves, the behavior of ultrasound in concrete needs to be simulated. As described in chapter 4, coda waves are very complex ultrasonic waves whose waveform is created from multiple scattering. This phenomenon can be modeled with equivalent high-fidelity simulations or simplified simulations that use homogenizations. The following subsections compare the different types of simulations for the coda problem and apply a finite element formulation to the problem.

5.1.1 High Fidelity Simulation

The high-fidelity simulation tries to describe the occurring physical processes as precisely as possible, which requires a very fine discretization in space and time. Fine spatial resolution is required to model the heterogeneity of concrete containing aggregates and pores that scatter the ultrasound. The fast-moving, high-frequency ultrasound wave requires fine discretization in time. For numerical stability in one dimension, the relation of mesh size Δx and time Δt also depends on the propagation velocity v and is known as

Courant-Friedrichs-Lewy condition (CFL Condition) [111]:

$$C = \frac{v\Delta t}{\Delta x} \tag{5.1}$$

The CFL Condition should generally be lower than 1 to ensure an accurate physical representation of the process. For n dimensions Eq. 5.1 changes as follows:

$$C = \Delta t \left(\sum_{n}^{i=1} \frac{v_{x_i}}{\Delta x_i} \right) \tag{5.2}$$

This work uses high-fidelity simulations to generate synthetic coda signals for numerical experiments. However, the later described imaging with CWI is working with simplifications (cf. Sec. 5.1.2). In order to generate the synthetic coda signals, a simulation is performed for every ultrasound transducer to generate a reference measurement. Then, synthetic damage in the form of a new scatterer is added to the model, and the simulation is repeated to generate the evaluated measurements. These simulations were performed by colleagues from Prof. Dr. Erik H. Saenger's team at the Bochum University of Applied Sciences. More information on the performed simulation of coda waves can be found in Finger et al. [112]. The code for seismic wave propagation uses a rotated staggered-grid finite difference scheme. In order to ensure numerical stability, time steps are chosen such that $C < 0.8$ (Eq. 5.2).

5.1.2 Simplifications

Modeling coda waves as precisely as possible requires fine discretization in space and time. This makes a large, structural-scale simulation computationally extremely expensive and thus infeasible for real-world problems. Therefore, the CWI typically uses a significant approximation by Ryzhik et al. [113], who have shown that the spread of a wave's energy in a random media as concrete can be approximated with a diffusive spread in a homogeneous medium. This relation can be seen in Figure 5.1 where the absolute values of the received signal are shown next to the solved diffusion equation at the receiver's position R for a spread from source S. One can see that the diffusion solution forms an envelope around the signal and, therefore, is a valid approximation for the energy contained in the signal. This approximation that homogenizes the material drastically reduces the complexity of the simulation because, unlike wave propagation simulations, the model used for solving the problem does not contain any scatters. Thus, mesh sizes and time steps can be increased. Additionally, the diffusion problem is a well-known parabolic partial differential equation (PDE) whose analytical solution for point sources exists. Also, the problem is well known in FEM. Thus, an application of FEM, a very versatile technique in terms of geometry and boundary conditions to the coda problem, is possible.

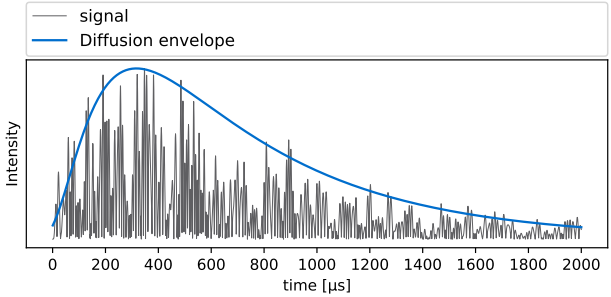

Figure 5.1: Envelope fitting of a signal (60 kHz) in concrete with the solved diffusion equation.

5.1.3 Analytical Solutions for the Coda Problem

Most probably due to its roots in geophysics, previous studies on imaging with CWI, e.g., Zhang et al. [21] and Planès et al. [23] use analytical solutions to describe the coda waves' intensity. The analytical solution for the just mentioned diffusion approximation in an infinite two-dimensional space with a point source that is active at $t = 0$ reads as follows [114]:

$$I_{Diffusion,2D}(r,t) = \frac{1}{4\pi Dt} e^{\frac{-r^2}{4Dt}} \tag{5.3}$$

The analytical solution that is valid for an infinite space needs to mirror a source at boundaries where energy is reflected. More recent publications [23, 115] used a different PDE to describe the wave energy spread. The solution of the radiative transfer equation (RTE) is similar to the solution of the diffusion PDE except for a part in the RTE that represents the ballistic wave. It is referred to as a more accurate representation of the actual coda wave and is expected to improve the results. Paasschens [116] gives an analytical solution of the RTE for similar boundary conditions as in Eq. 5.3:

$$I_{RTE,2D}(r,v,t) = \frac{e^{-r/l}}{2\pi rv}\delta(t-\frac{r}{v}) + \frac{\sqrt{1-\frac{r^2}{v^2t^2}}}{4\pi Dt} e^{\frac{1}{l}\sqrt{v^2t^2-r^2}}\Theta(vt-r) \tag{5.4}$$

In both analytical solutions, r stands for the distance to the source, t is the time, and D represents the diffusivity of the medium. In Eq. 5.4, δ represents the Dirac delta, Θ is a Heaviside function, and v is the wave speed. The first summand of Eq. 5.4 represents the ballistic wave and is "activated" by the Dirac delta for the time of the wave passing the location ($t = r/v$). It is referred to as the coherent term. The second summand of Eq. 5.4 is very similar to Eq. 5.3 and represents a diffusive spread of the scattered wave. Further insight into the RTE is given in Sec. 5.1.5.

5.1.4 Finite Element Formulation for the Coda Problem

FEM is an universal method for solving a given PDE. The derivation of the finite element (FE) formulation for the coda wave behavior with its analogy to a diffusive spread is described following Ottosen et al. [117] and Zienkiewicz et al. [118] that are both standard works of FEM. FEM subdivides the large solution field into smaller finite elements. The solution is approximated for each element with predefined functions (called shape functions) whose derivatives are also known in advance. This is done by transforming the PDE (here given in Eq. 5.5), which is also referred to as strong form, into a weak form that satisfies the PDE not at every position $\mathbf{x}$ but over the domain Ω in a weak sense. Based on the mentioned authors [117, 118], the strong form of the coda problem using the diffusion analogy can be formulated as follows:

$$-\nabla^T(D\nabla\mathbf{I}) + \mathbf{Q} = \frac{\partial \mathbf{I}}{\partial t} \tag{5.5}$$

where D is the diffusivity of the medium, $\mathbf{I}$ is the wave energy concentration, and $\mathbf{Q}$ describes sources or sinks, which in the context of the coda technology are the ultrasound transducers. The weak form is obtained using the weighted residual method (Galerkin method) and satisfies Eq. 5.5 over a domain Ω:

$$\int_\Omega \mathbf{v}\left[\frac{\partial \mathbf{I}}{\partial t} + \nabla^T(D\nabla\mathbf{I}) - \mathbf{Q}\right] d\Omega = 0 \tag{5.6}$$

$\mathbf{v}$ refers to a weighting function (also called test function) that is weighting the residual such that the unnoticed compensation of positive and negative contributions is avoided. FEM then approximates the solution $\mathbf{I}$ with predefined shape functions $\mathbf{N}$.

$$\mathbf{I} = \mathbf{N}\mathbf{u} \tag{5.7}$$

Here $\mathbf{u}$ contains the wave energy concentration at the discrete points which connect the elements. These nodes are also referred to as control points. In the Galerkin method, the shape functions that describe $\mathbf{I}$ are also used to describe the weighting function $\mathbf{v}$. The weak form is then integrated by parts, and the approximations with shape functions are inserted. Zienkiewicz et al. [118, Ch. 5] give the result as

$$\mathbf{C}\dot{\mathbf{I}} + \mathbf{K}\mathbf{I} = \mathbf{f} \tag{5.8}$$

with the following element contributions whose integrals need to be evaluated and assembled into the global matrices of Eq. 5.8:

$$\begin{aligned} \mathbf{C}_e &= \textstyle\int_{\Omega_e} \mathbf{N}^T\mathbf{N} d\Omega \\ \mathbf{K}_e &= \textstyle\int_{\Omega_e} \mathbf{B}^T D\mathbf{B} d\Omega \\ \mathbf{f}_e &= \textstyle\int_{\Omega_e} \mathbf{N}^T\mathbf{Q} d\Omega \end{aligned} \tag{5.9}$$

$\mathbf{B}$ contains the derivatives of $\mathbf{N}$ such that

$$\nabla\mathbf{I} = \mathbf{B}\mathbf{u} \qquad \text{with } \mathbf{B} = \nabla\mathbf{N} \tag{5.10}$$

Note that compared to Zienkiewicz et al. [118, Ch. 5] the terms referring to the energy flux at the boundary Γ have been omitted because it is assumed that the ultrasound signal is reflected at boundaries with negligible energy loss. To solve the transient problem, the time domain must also be approximated. The Crank-Nicolson method [119] is an unconditionally stable problem-solving method. The following explanation is based on Taler et al. [120]. The method uses a generalized trapezoidal approximation of the time domain to obtain the wave energy concentration at the time step n + 1:

$$\mathbf{I}^{n+1} = \mathbf{I}^n + \left[(1-\theta)\dot{\mathbf{I}}^n + \theta\dot{\mathbf{I}}^{n+1}\right]\Delta t \tag{5.11}$$

where Δt is the time step between time steps n and $n+1$. The Crank-Nicolson method uses $1/2$ as the temporal parameter θ, making it a semi-implicit method. Multiplying both sides of Equation 5.8 with θ for time step $n+1$ and with $1-\theta$ for time step n and algebraically adding both terms then leads to:

$$\mathbf{C}\left[(1-\theta)\dot{\mathbf{I}}^n + \theta\dot{\mathbf{I}}^{n+1}\right] + \mathbf{K}\left[(1-\theta)\mathbf{I}^n + \theta\mathbf{I}^{n+1}\right] = (1-\theta)\mathbf{f}^n + \theta\mathbf{f}^{n+1} \tag{5.12}$$

Combining Equation 5.11 and Equation 5.12 and rearranging to a form of $\mathbf{K}^*\mathbf{I}^{n+1} = \mathbf{f}^*$ that lets one solve for the unknown $\mathbf{I}^{n+1}$ leads to the final problem to be solved:

$$\left(\frac{1}{\Delta t}\mathbf{C} + \theta\mathbf{K}\right)\mathbf{I}^{n+1} = \left[\frac{1}{\Delta t}\mathbf{C} - (1-\theta)\mathbf{K}\right]\mathbf{I}^n + (1-\theta)\mathbf{f}^n + \theta\mathbf{f}^{n+1} \tag{5.13}$$

The explained steps for deriving a FE formulation apply to any given PDE. If a different PDE is found that describes the scattering behavior of coda waves better, the FEM methodology is an ideal candidate for solving the problem. Due to its weak formulation, the used shape functions only approximate the exact solution. Those functions are, in general, exchangeable. The FE solution can be improved by increasing the polynomial order of the used functions. The flexibility of FEM can be applied to the dimensionality and element geometry. For 2D geometries, a very versatile formulation is based on triangles, and for 3D geometries, it is based on tetrahedrons. The analytical solution that is valid for an infinite space needs to mirror a source at boundaries where energy is reflected. The boundary conditions in FEM can respect that reflecting behavior which is especially useful for complex geometries without a clear mirror axis.

Compared to the analytical solution of a PDE that is valid for only one specific case, the FE solution has advantages because all kinds of boundary conditions in terms of geometry or the time of the source being active can be handled.

Fig. 5.2 and Fig. 5.3 show the results of the FEM simulation for the experiment of Sec. 6.1. One can see the diffusive spread from transducer 4 (cf. Fig. 6.1) at different timesteps that illustrate how the energy spreads into the medium.

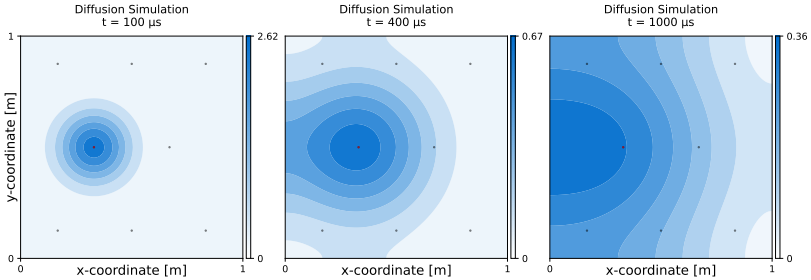

Figure 5.2: FEM simulation results for the diffusive spread from one transducer (cf. experiment of Sec. 6.1).

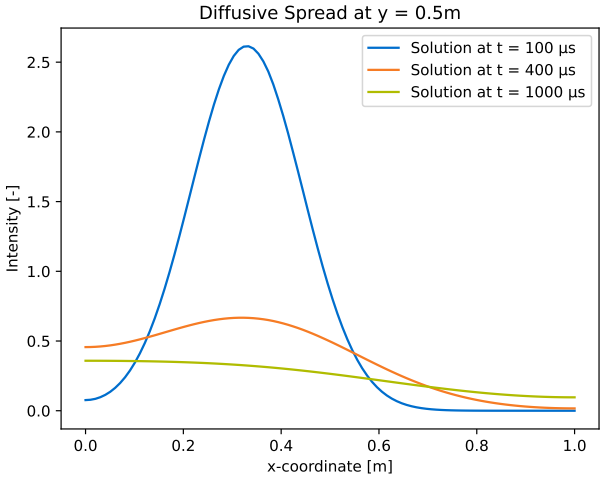

Figure 5.3: Diffusive spread of Fig. 5.2 at cutting plane y = 0.5 m.

5.1.5 Combination of Finite Element Based and Analytic Approach

As mentioned in Sec. 5.1.3 recent publications [23, 115] describe the RTE of Eq. 5.4 as more suitable for simplifying the coda problem. The main reason is the coherent term that represents the ballistic wave. The ballistic wave is increasingly important, especially for frequencies in the transition range of single and multiple scattering. A second main difference between Eq. 5.4 and the classic diffusion problem is the Heaviside function limiting the diffusive spread to the wave speed, which physically makes sense. In order to improve

the FEM solution of the diffusion problem, the two described improvements of the RTE are applied to the FEM solution in a post-processing step.

$$I_{\text{FEM+Analytic}}(r,v,t) = \underbrace{\frac{e^{-r/l}}{2\pi r v}\delta(t-\frac{r}{v})}_{\text{coherent term}} + I_{FEM}(r,v,t) \quad \underbrace{\Theta(vt-r)}_{\text{Heaviside function}} \tag{5.14}$$

For applying the Heaviside condition on the FEM solution, the p-wave speed v is used. The coherent term representing the ballistic wave is added to the solution. For discrete meshes and time steps, the Dirac delta $\delta(t-\frac{r}{v})$ creates difficulties. Generally speaking, it activates the corresponding term for the exact moment of the wave passing. This activation happens at the time step closest to the time passing a corresponding node for the used discrete meshes. In order to represent border reflections, the transducers are mirrored at the borders.

Another discontinuity occurs at the source position because the distance to the source appears in the denominator in Eq. 5.14. Thus, a modification at the source position is left out. This, unlike at all other nodes, ultimately does not increase the sensitivities at the source position. However, this is neglected since the sensitivity at transducer positions is significantly larger than in other areas, and the modification would only affect the first time step.

Fig. 5.4 and Fig. 5.5 compare the improved diffusion simulation to the standard FEM results from Fig. 5.2. One can see how the Heaviside function

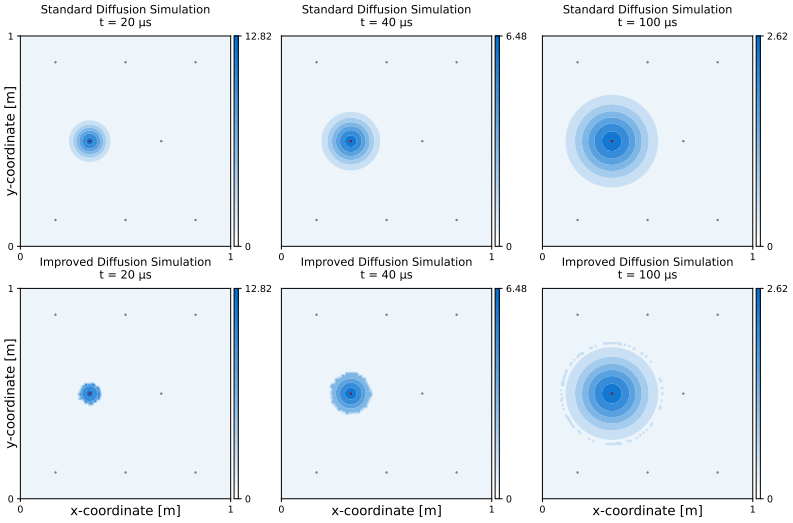

Figure 5.4: FEM simulation results for the diffusive spread from transducer for the experiment of Sec. 6.1.

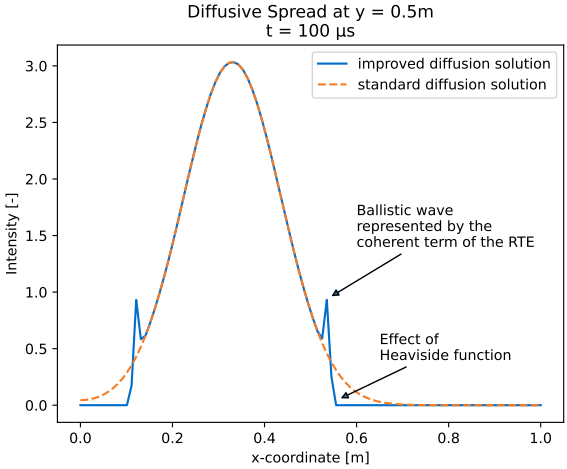

Figure 5.5: Diffusive spread of Fig. 5.4 at cutting plane y = 0.5 m.

limits the radius of the diffusive spread. For $t = 100\,\mu s$, the additional coherent term RTE is more visible. Note that the inconsistencies in the circle in Fig. 5.4 result from treating the Dirac delta in discrete meshes. Also, for the early time steps, the spread is no longer a perfect circle, which is also due to the behavior of a Heaviside function in discrete meshes. However, these are only cosmetic issues. Due to the exponential influence, the improvements only change the diffusive spread at early time steps where the energy spread close to a transducer is simulated. Therefore, the boundary reflections of the ballistic wave, represented by the coherent term, are not visible. For an improved understanding, Fig. 5.6 shows only the coherent term without the main diffusive spread.

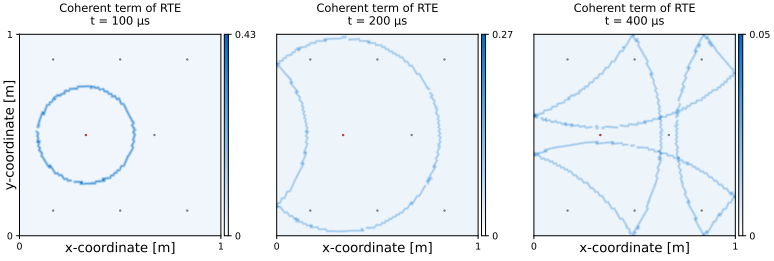

Figure 5.6: Spread of the ballistic wave (= coherent term in Eq. 5.14).

5.1.6 Choice of the Homogenization Parameter Diffusivity

The main parameter when using the diffusion analogy to approximate the signal's energy spread is the diffusivity D of the medium. The larger the diffusivity, the faster energy moves away from the source. It depends on several parameters, such as the number of scatterers in the medium and their size compared to the wavelength of the initial signal. In case the distance on which the waves lose all the information about their initial direction due to scattering (referred to as mean scattering free path l^*) is known, Sheng [121] gives the formula to compute the diffusivity D depending on the dimensionality d of the model and average velocity of the transport of energy ν:

$$D = \frac{\nu l^*}{d} \qquad \text{with} \begin{cases} d = 2 \text{ for plane problems ,} \\ d = 3 \text{ for volumetric problems.} \end{cases} \tag{5.15}$$

5.1.7 Envelope Fitting

The diffusion coefficient can also be obtained with an envelope fitting of the signals' absolute values I_{Signal} using the solved diffusion problem shown in Figure 5.1. Due to its simple and fast evaluation, the analytic diffusion solution of Eq. 5.3 is used. In order to describe the actual signal as precise as possible, a part describing the energy dissipation is added to Eq. 5.3 with $\mathcal{D}$ as the dissipation factor:

$$I_{Diffusion,2D}(r,t,D,\mathcal{D}) = \frac{1}{4\pi Dt} e^{\frac{-r^2}{4Dt}} e^{-\mathcal{D}t} \tag{5.16}$$

To give an outlook: The previous neglect of dissipation does not affect the imaging with CWI described in Sec. 5.2 since the term vanishes in Eq. 5.19. Thus, as a simplification, the dissipation is only respected for the envelope fitting. With time t and source-receiver distance r being fixed for a signal, the tunable parameters for the envelope fitting are the diffusivity D and the dissipation factor $\mathcal{D}$. The two parameters are found in an iterative process. First, the time of the signal's maximum is searched. It is obtained by averaging the time of the signal's three maximum amplitudes. As shown in Fig. 5.1, the envelope forms a maximum at this point. To find D, the derivative of Eq. 5.16 with respect to t is set to zero, and with known t_{max} of the extreme point from the actual signal, one can solve for D:

$$\begin{aligned} \tfrac{d}{dt} I(r,t,D,\mathcal{D}) &= \underbrace{\frac{1}{4\pi Dt} e^{-\frac{r^2}{4Dt}} e^{-\mathcal{D}t}}_{\neq 0} \underbrace{\left(-\frac{1}{t} + \frac{r^2}{4Dt^2} - \mathcal{D} \right)}_{=0} = 0 \\ \text{solve for } D\text{:} \qquad D(t_{max}) &= \tfrac{r^2}{4t_{max}(\mathcal{D}t_{max}+1)} \end{aligned} \tag{5.17}$$

In the next step, an envelope connecting the peaks of the second half of the signal ($t \geq T/2$) is formed, as the dissipation strongly influences the intensity

loss. The dissipation factor $\mathcal{D}$ is found with a least-squares fitting:

$$\min_{\mathcal{D}\in\mathbb{R}} \|I_{Signalenvelope}(t) - I_{Diffusion,2D}(\mathcal{D},t)\|_2^2 \qquad \begin{array}{l}\text{with } t \geq T/2 \\ \text{subject to } \mathcal{D} \geq 0\end{array} \tag{5.18}$$

Since the dissipation factor influences the position of the maxima, the search for D and $\mathcal{D}$ is repeated iteratively.

5.2 Imaging Problem

The simulation described in Section 5.1 approximates the waves' energy spread. The evaluated measurement, however, is a decorrelation development of two compared signals. In order to transfer the wave simulation to a model representing the signal decorrelation, sensitivities of the coda wave are computed.

5.2.1 Coda Wave Sensitivities

Sensitivities are, in general, gradient information, so information from the first-order partial derivatives of a function. They are needed in the Gauss-Newton algorithm that is applied applied to solve inverse problems (cf. Ch. 3). For coda waves, the sensitivities describe how an input variation δx that in the case of CWI is something that affects the wave, e.g., little damage occurring, changes the response value y, that in the case of CWI is, e.g., a DC measurement. With the assumption that the wave information, which is the waveform, is created from multiple scattering, Pacheco et al. [122] applies a model of random paths to compute the sensitivities of the coda wave. The sensitivities depend on the position x at which a scattering event can occur during a travel time t from source S to receiver R:

$$K(S,R,x,t) = \frac{\int_0^t I(S,x,u)I(x,R,t-u)\,du}{I(S,R,t)} \tag{5.19}$$

In Eq. 5.19 (pictured in Fig. 5.7), $I(position\ 1, position\ 2, t)$ stands for the wave intensity at *position* 2 after time t of a wave starting from *position* 1. Looking at the numerator of Eq. 5.19, one can see that the integral sums up all the time combinations of a wave going from the source position S to position x to the receiver position R in time t. These combinations are also referred to as random paths. Since the waves going through position x are just a fraction of all wave paths arriving at the receiver R, the numerator term is normalized by the general possibility of a wave traveling from source S to receiver R in time t.

Fig. 5.8 gives an example of coda sensitivities in the model from the numerical experiments in Sec. 6.1. One can see that the sensitivities depend on the time evaluated and are very large in areas close to the source or receiver. For the imaging problem, next to the magnitude of sensitivities relative to other positions, the development of sensitivities over time in the signal is crucial.

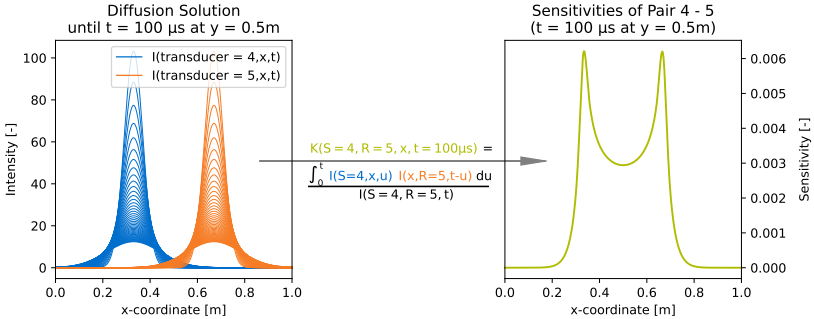

Figure 5.7: Visualization of a the sensitivity computation with Eq. 5.19 (model from Sec. 6.1). *(First 10 time steps not plotted.)*

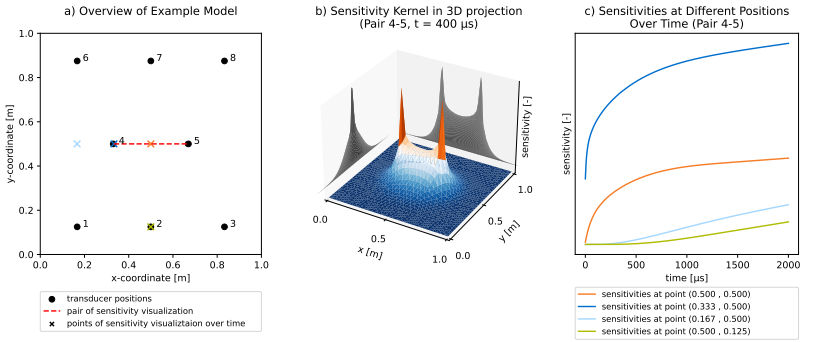

Figure 5.8: Visualization of a typical sensitivity kernel (model from Sec. 6.1).

Since a new scattering event in concrete, that Pacheco et al. [122] assumes in the random paths model, can only be caused by a crack due to filtering of other influences (cf. Sec. 4.7), the imaging problem becomes one specifically for damage localization.

5.2.2 Inverse Problem for Damage Localization

The sensitivity kernel K of Eq. 5.19 is a model that simulates the effects of new scatterers in the propagation medium. It allows to relate coda wave sensitivities to decorrelation measurements that form an inverse problem. The CWI based damage localization with this inverse problem was significantly developed by Larose et al. [12], Rossetto et al. [123] and Planès et al. [23]. With the assumption of small damage, the relation of a change in the medium

x and the corresponding measurement values is assumed to be linear [23]:

$$\mathbf{A}\mathbf{x} = \mathbf{y} \tag{5.20}$$

A is a matrix containing the sensitivity kernel for one pair at a specific time in each row. The vector **y** contains the measured decorrelation in the signal with pair and time matching the sensitivity kernel in the corresponding row. A graphical overview of the problem is given in Fig. 5.9. As CWI is a relative

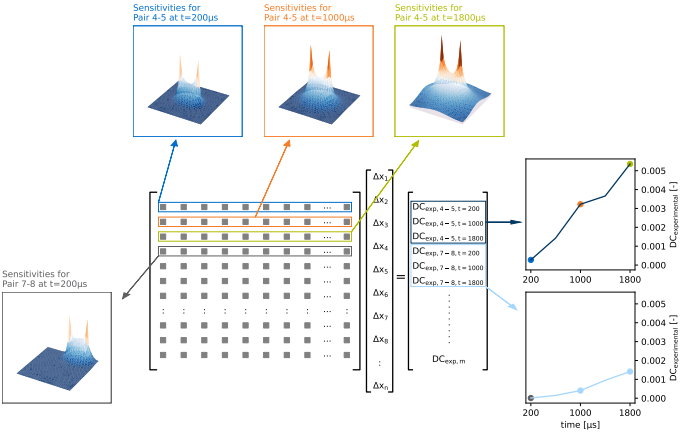

Figure 5.9: Visualization of a typical imaging problem with CWI (model from Sec. 6.1).

measurement technology, the values in **y** are no absolute measurements. They are a measured change $\Delta\mathbf{y}$ coming from a change of the initial state to the current state. The initial state is typically unknown, a classical problem with relative measurements. In Eq. 5.20, vector **x** also does not contain the actual state but only the change $\Delta\mathbf{x}$ to the initial state. These changes $\Delta\mathbf{x}$ are with the model of Pacheco et al. [122] new scatterers. Since the new scattering is assumed to come from new cracks, **x** can be understood as the damage at each mesh node. The size of matrix **A** is $m \times n$, with n referring to the number of nodes in the mesh and m referring to the total number of measurements. Typically, the amount of nodes in the mesh is larger than the number of measurements, and thus the problem is underdetermined. In order to solve the problem of Eq. 5.20, the solution algorithms introduced in Ch. 3 are applied. For the specific case of damage localization based on DC measurements, one can also introduce the assumption that the solution needs to be positive. This is because sensitivities are only positive, and a change Δx can only create a positive DC measurement.

5.2.3 Clipping of Sensitivities

The application of CWI in practical experiments has shown a tendency of damage localization directly at the position of transducers despite the damage appearing in areas away from the transducer. Such a phenomenon can also be seen in experiments from literature (cf. [124, 125]). Drastically greater sensitivities at the position and immediate vicinity of the transducers are a possible cause. These values at transducer positions are many times larger than those that are, e.g., the transport mean free path l^* away from transducers. For solving the ill-posed imaging problem, this immense influence of transducer positions, in the end, leads to localization at these exact positions that, however, should be avoided. The numerical models simplify a transducer as a point source which is a singularity for the FEM model. In reality, the transducer has real dimensions shown in Fig. 4.7. In order to compensate for the numerical singularity in the model, in this study, the sensitivities are modified at the position of transducers by clipping the peaks for the application of CWI in real structures. There are several ways to determine the clipping values. One way would be to use the sensitivity value at a defined distance, e.g., transport mean free path l^*, to the transducer as the limit value. Due to difficulties for transducers close to a border where such a point might be out of the model, open questions due to the different source-receiver distances and a significant uncertainty on the transport mean free path l^* for the given frequency range, a more straightforward approach is used in this study. Sensitivities are limited to a fixed fraction of the maximum value. The clipping of sensitivities for a threshold of $\frac{1}{2}$ of the maximum value is shown in Fig. 5.10.

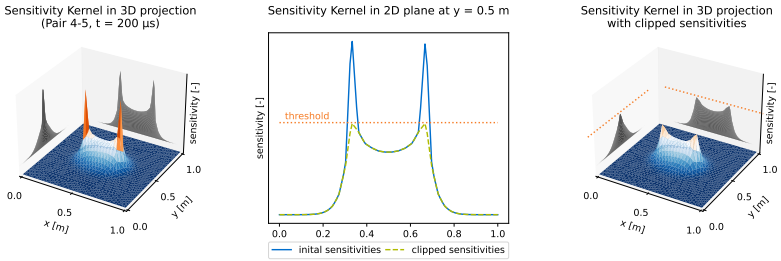

Figure 5.10: Illustration of clipping the sensitivity values at a fraction of 0.5 of the maximum value (model from Sec. 6.1).

A parameter study has shown that reducing the fraction used for the threshold leads to a smoother solution field for real experiments. This comes with a loss in resolution for damage detection but immense improvements in robustness. The clipping of sensitivities can be interpreted as a smoothing of sensitivities known to have a smoothing effect on the solution field.

5.2.4 Remarks on the Solution Space

This section discusses the solution space obtained in more detail for better classification. Known quantities in the imaging problem are the decorrelation measurements stored in the vector $\mathbf{y}$ with $b \in \mathbb{R} : 0 \leq y \leq 1$ and the sensitivities of the matrix $\mathbf{A}$. Note that unlike measured phase shifts in the signal due to a wave speed change δv, there is no clear physical relation for the decorrelation measurements. This lack already indicates the difficulties in interpreting the solution space. A range for the sensitivities is challenging, but values are positive and $<< 1$. Sensitivities relative to each other in space and time are much more crucial for the imaging. The damage vector $\mathbf{x}$ relates the sensitivities linear to the measurements. Due to the sensitivities, which are difficult to interpret in terms of magnitude, the values of the solution space are also not classifiable. However, values must be positive. Values of the solution set should only be compared to each other, and the solution should generally be understood as a binary statement about the damage. Moreover, the node values depend on the mesh refinement (cf. Fig. 6.11), so the sum over a specific range is constant. When localizing damage, it should also be clear whether the result should be as precise as possible or somewhat fuzzier but more robust against mislocalization. These preferences can be controlled with the optimization algorithm's regularization factor α or a constraint limiting the solution space ($x \leq x_{max}$).

In order to improve the imaging problem, calibration is desirable, but it is challenging since one would need to identify the system as precisely as possible. In case a value of x for macro cracks is known, e.g., from laboratory calibration experiments, this threshold can be used to classify a detected damage area as a crack or not. Alternatively, one could introduce a constraint $x \leq x_{crack}$ to the optimization problem, which would increase the detected damaged area, and comparison of results for different load steps might be easier.

Chapter 6

Results on Damage Localization with Coda Waves

Parts of this chapter are taken from Grabke et al. [110].

The FEM based damage localization with coda waves is tested in three experiments. First, a synthetic experiment is performed. Then, the technology is applied to a laboratory's actual large-scale concrete specimen. The last experiment is to see how much the technology can be applied to existing structures. In this three-step scheme, the knowledge and controllability of influencing parameters decrease. Thus, the numerical experiment investigates several numerical input parameters and their sensitivity to the obtained solution. The laboratory experiment is primarily used to investigate the damage development closely. The application at an existing bridge shows the current status of practical applications.

6.1 Damage Localization with Synthetic Data

6.1.1 Experimental Setup

The numerical experiment is based on one presented in multiple publications [23, 115, 126, 127] with variations in the transducer and damage position. The spatial overview of the experiment is shown in Fig. 6.1. The wave propagation simulation uses the same settings as the simulation by Planès et al. [115] with a Gaussian impulse with a central frequency of 500 kHz, 23000 randomly distributed scatterers, a grid step of 333 μm and a time step of 94.2 ns. Each scatter has the size of one grid point, which makes the volume fraction of scatterers 2.55 ‰. The wave propagation simulation was performed by colleagues from the team of Prof. Dr. Erik H. Saenger at

the Bochum University of Applied Sciences (cf. Finger et al. [112] for more information). The wave propagation from every transducer was simulated twice, once without and once with damage in the form of three new scatters added.

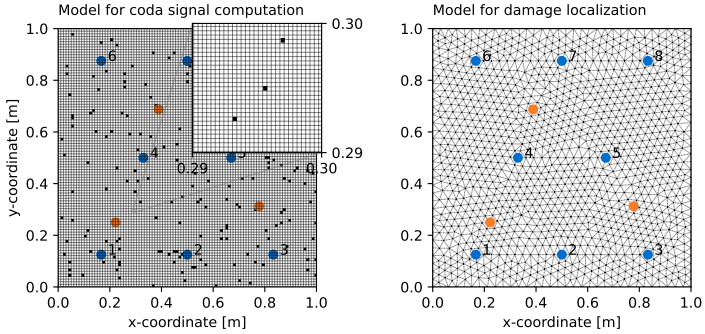

Figure 6.1: Overview of the performed numerical experiment. Left shows the coda signal computation model with scatterers in the form of grid points. The right shows the unstructured mesh used for damage localization. Blue dots mark the transducer positions, and orange dots mark the damage locations.

Each synthetic signal was evaluated in five consecutive non-overlapping windows of length 400 μs after the arrival of the first wave (time-of-flight (tof)) with the correlation evaluation of Eq. 4.7 and 4.6. A total of 56 measurement pairs results in a size of 280 for $\mathbf{b}$ from Eq. 5.20.

An advantage of the numerical experiment is the precisely known damage position and extension to be detected. This knowledge means that in the optimization problem of Eq. 5.20 next to the measurement vector $\mathbf{b}$, the usually unknown damage vector $\mathbf{x}$ is known. For a system calibration, the problem of Eq. 5.20 can be used to find the optimal coda wave sensitivities $\mathbf{A}$ for the given case. With a reformulation to a least squares problem, one can solve for the diffusivity D that represents the heterogeneity of the material, and that is the main parameter influencing the sensitivities:

$$\min_{D\in\mathbb{R}} \|\mathbf{A}(D)\mathbf{x} - \mathbf{b}\|_2^2 \qquad \text{subject to } D \geq 0 \tag{6.1}$$

Solving Eq. 6.1 results in $D = 64.25\frac{m^2}{s}$. Note that computed coda wave sensitivities for a rather large D make it computationally cheap to compute sensitivities of smaller diffusivities. One can see in Eq. 5.3 that D and t always appear in combination. Thus, one can approximate the sensitivities of a different diffusivity by varying the time axis. This procedure of finding

the homogenization parameter for the material is different from the original experiment by Planès et al. [115] that computes the diffusivity as follows:

$$D = \frac{vl^*}{2} \tag{6.2}$$

Next to the wave speed v, the transport mean free path l^* (cf. Sec. 4.4) is required for this approach. Planès et al. [115] gives a formula to compute the scattering mean free path l that in the case of uniform scattering is equal to l^*. However, this formula requires additional computational expansive simulations and is thus less practical. However, the authors end up with a diffusivity of $D = 62.5 \frac{m^2}{s}$, which is in good accordance with the used $64.25 \frac{m^2}{s}$.

The model for damage localization differs from the very fine grid used for the wave propagation simulation. The shown results use an unstructured mesh that can be seen on the right in Fig. 6.1 with an average node distance of 0.03 m. This refinement results in 1284 nodes, the number of unknowns of the inverse problem. The mesh resolution is chosen to be finer than the mean scattering free path l^* that, in this case, is given as 0.05 m by Planès et al. [115]. The mean scattering free path l is referred to as a quantity to what accuracy the CWI can detect damage. A study on the mesh refinement is performed in Sec. 6.1.7.

6.1.2 Finite Element Based Damage Localization

The settings described above create a problem with 1284 unknowns and 280 known measurements. Tab. 6.1 provides an overview of the used parameters. By solving the inverse problem of Eq. 5.20 with the trust region reflective algorithm of Sec. 3.6.2 and the constraint $\mathbf{x} \geq 0$, the solution in Fig. 6.2 is obtained. The solution is very satisfying compared to the previous studies [23, 115, 126, 127] on a comparable setup. For further improvements and parameter investigations, this solution is used as a reference for the following parameter studies. Based on the settings of this solution, one parameter is varied after the other.

6.1.3 Evaluation of the Analytic Solution Based Improvements

The basis solution shown in Fig. 6.2 uses the FEM based solution with the analytic improvements of Sec. 5.1.5. In order to evaluate the effect of these improvements, the solution is compared to a pure FEM based damage localization in Fig. 6.3. As expected, the effect of the analytic solution-based improvements is rather small but positive. Next to the reduced residual, one can see that the improvements allow for even preciser damage localization.

Simulation parameters for damage localization	
Intensity computation	FEM-based (Sec. 5.1.4) + Improvements of Sec. 5.1.5
Specimen dimensions	$1\,\mathrm{m} \times 1\,\mathrm{m}$
Average node distance	$0.03\,\mathrm{m}$
Number of nodes	1284
Simulation time step	$1 \times 10^{-6}\,\mathrm{s}$
Diffusivity	$64.25\,\frac{m^2}{s}$
Evaluated signal length (after tof)	$2000\,\mu\mathrm{s}$
Decorrelation window length T	$400\,\mu\mathrm{s}$
Amount of measurements	280
Solving algorithm	Trust Region Reflective Algorithm (Sec. 3.6.2)

Table 6.1: Overview of the simulation parameters for damage localization at the numerical experiment.

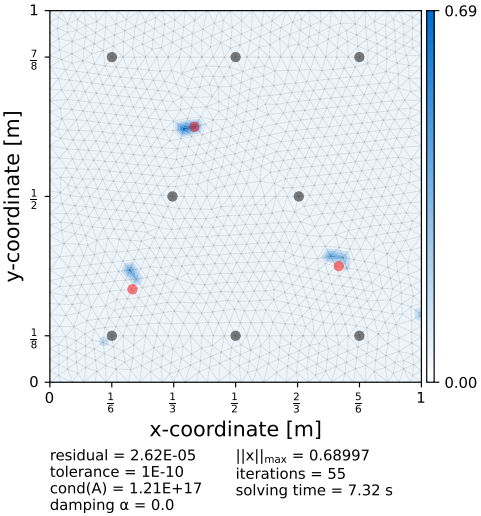

Figure 6.2: Damage localization for the numerical experiment with the settings of Tab. 6.1.

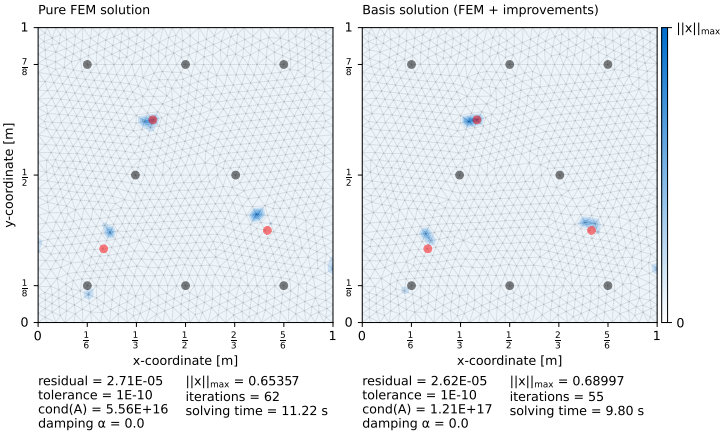

Figure 6.3: Evaluation of the analytic solution based improvements of Sec. 5.1.5.

6.1.4 Comparison of Analytical Solutions to Finite Element Based Damage Localization

The advantages of FEM have already been discussed in Sec. 5.1.4. This section compares the FEM based solution (without improvements) to the more established analytic approaches that have also been used in the original experiment by Planès et al. [115]. The result is shown in Fig. 6.4. Generally, the residual for the given setup is less for the analytic solution. However, the damage localization works very well for all three cases. The residual for

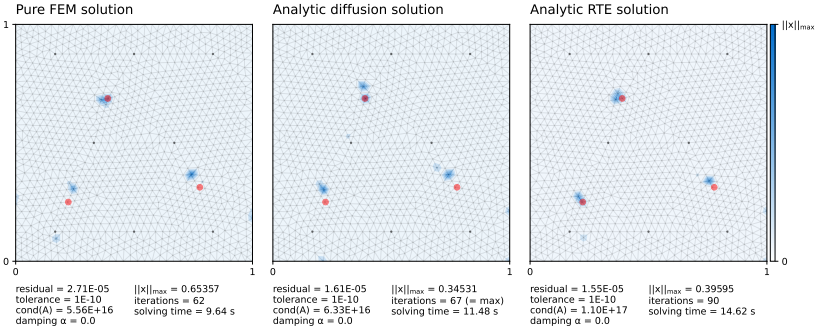

Figure 6.4: Comparison of FEM-based and analytical solution-based damage localization.

the known damage locations was computed for a second evaluation. For this purpose, the damage vector obtained from the solving algorithm was replaced with the known damage positions. The corresponding residuals are shown in Tab. 6.2.

	Pure FEM solution	Analytic diffusion solution	Analytic RTE solution
residual	3.79×10^{-5}	2.79×10^{-5}	2.519×10^{-5}

Table 6.2: Residual for replacing the optimization solution with the known damage vector.

Comparing the values from Tab. 6.2 to Fig. 6.4 contains a surprise. The residual is larger when using the known damage vector. Thus, the expected global minimum, the "perfect" solution, is impossible to find when solving the optimization problem. A probable reason is that the underlying model that relates measurements and sensitivities is based on random paths and has no governing physical law. For the known damage positions, the residual for the analytic solutions is smaller than for the FEM based solution. Keeping in mind that the FEM approach allows computing arbitrary geometries with correct treatment of boundary reflections, the combination of FEM with the two analytic solution-based improvements (Sec. 5.1.5) seems to be an appropriate trade-off. This approach leads when using the known damage position vector to the residual of 3.49×10^{-5} that is in-between the residual of the pure FEM solution and the analytic ones.

6.1.5 Comparison of Different Solution Algorithms

The optimization problem for damage localization is generally inconsistent, large-scale, and ill-posed. The used solution algorithm and its settings are thus of immense influence. The trust region reflective algorithm (Sec. 3.6.2) has proven robust for the previous evaluations. Another option to solve the inverse problem is the manually implemented projected gradient descent method (Sec. 3.6.1) that necessarily requires regularization. For better comparison, the solution of the damped trust region reflective algorithm is also taken into the comparison of Fig. 6.6. In order to obtain a good regularization factor α, the L-curve method of Hansen [60] (cf. Sec. 3.4) is performed (cf. Fig. 6.5).

For the given problem, the damping does not have a significant impact because a satisfying, non-oscillating solution is obtained even without regularization due to further internal regularizations of the `scipy.optimize.lsq_linear` implementation. The L-curve, therefore, has no apparent kink but is a relatively smooth curve. Nevertheless, damping is essential for the real experiments in the following sections.

In the evaluation of Fig. 6.6, one can see that the obtained solutions are very similar for all settings. However, the residuals of the trust region reflective algorithm and projected gradient descent method differ significantly.

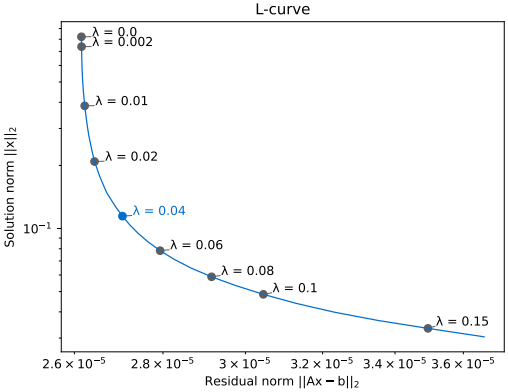

Figure 6.5: L-curve method of Hansen [60] for the trust region reflective algorithm.

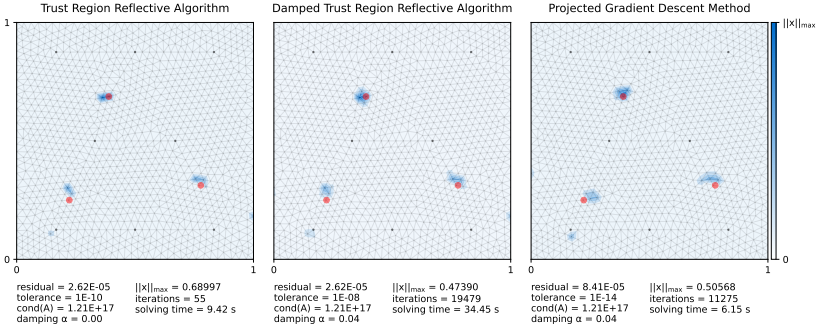

Figure 6.6: Comparison of different algorithms for solving the least-squares optimization problems.

Another difference can be seen in the number of iterations for the undamped solution, which is very little compared to the damped solutions. This is due to the damping that limits the step sizes. However, the computation times per iteration step for the damped algorithms are significantly lower because of an improvement of the problem for numerical analysis by adding the regularization term. Note that the number of iterations significantly influences the extension of the obtained damage region, and the tolerances are thus adjusted individually to obtain comparable damage extensions. Small mislocalizations are seen in all solutions, and in particular, the one near the transducer on the bottom left is common to all. Another comparison of the two different algorithms is shown in Fig. 3.4 with a similar result. Due to

a better performance in obtained residual and general robustness, the trust region reflective algorithm is chosen as a standard algorithm for imaging with CWI in this thesis.

6.1.6 Study on the Used Evaluation Time Frames

The evaluation time frames refer to the window length T to compute the DC. Longer evaluation frames likely create a smoother DC development over the signals' length. However, they reduce the number of measurements. This reduction could affect the optimization problem and lead to worse conditioning. Next to increasing the number of measurements by varying the evaluation frame length, it can also be increased by overlapping the evaluation frames. These parameters are evaluated in Fig. 6.7.

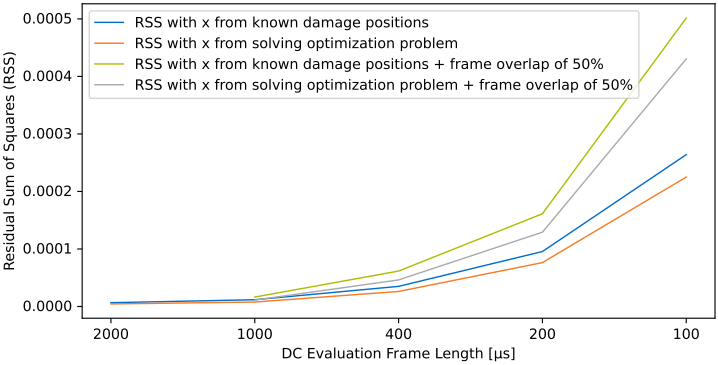

Figure 6.7: RSS for different evaluation frame lengths.

As already seen in Sec. 6.1.4, the solution from solving the optimization problem gives, according to the RSS, a better fit than when using the known damage positions. Contrary to what is indicated above, the optimization problem does not seem to be affected by reducing the number of measurements. In Fig. 6.7, one can see that the RSS is the lowest for the longest evaluation window and the largest for most measurements. This is because, with an evaluation window length of $T = 2000\,\mu s$, fewer summands contribute to the RSS than with shorter window lengths. Thus, the improved evaluation is the average misfit per measurement as shown in Fig. 6.8 and additionally, the imaging solution for three different time frame lengths is shown in Fig. 6.9.

The average error shown in Fig. 6.8 could conclude that an overlap of evaluation frames is the best choice. However, this creates a correlation of measurement values neglected in this thesis (cf. Sec. 3.5). Fig. 6.8 also suggests that a window length of 1000 µs is the best choice. However, the imaging of Fig. 6.9 with $T = 1000\,\mu s$ is not as satisfying as the one for $T = 400\,\mu s$ despite the smaller residual. As the imaging for $T = 200\,\mu s$

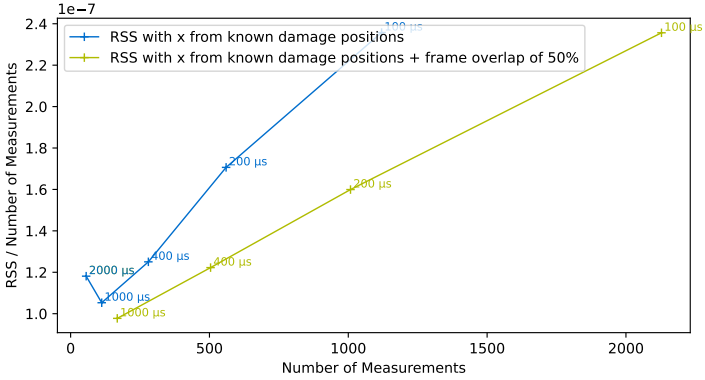

Figure 6.8: RSS per measurement for different evaluation frame lengths that are given in µs with colored numbers in the figure.

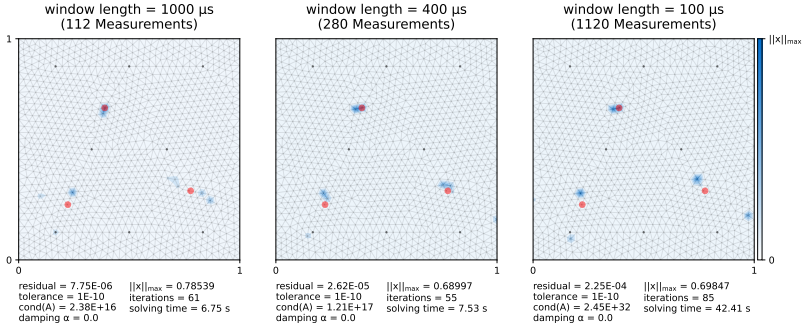

Figure 6.9: Comparison of damage localization for different evaluation frame lengths.

shows more mislocalizations, the frame length of $T = 400\,\mu s$ is chosen as the standard.

6.1.7 Study on Mesh Refinements

In general, a finer mesh allows more precise imaging of a quantity. For the case of damage localization by solving an inverse problem, a refinement, however, also leads to an increase of unknowns. Thus, the previously used refinement orients itself at the scattering mean free path l that Planès et al. [115] describe as a quantity to what accuracy the CWI can detect damage. This assumption should be verified with a study on mesh refinement later used to find appropriate refinement for the practical experiments.

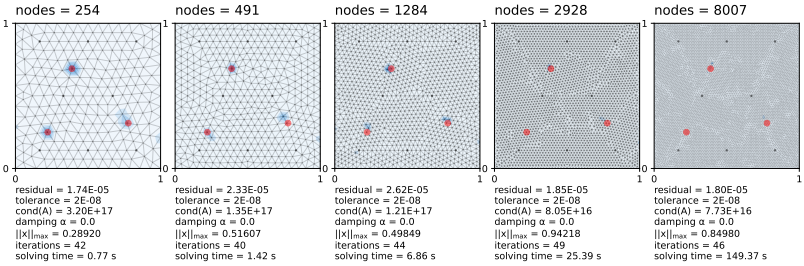

Figure 6.10: Comparison of damage localization for different mesh refinements.

The evaluations of Fig. 6.10 result in similar residuals. Optically, all imaging results also appear very satisfying. However, the extension of the damage region strongly differs and is mesh-dependent as only one or two nodes are identified as damaged. With the real damage being significantly smaller than the mesh sizes, the punctual localization appears to be more precise for the fine mesh. However, real damage most likely has larger extensions, and pointwise localization might only sometimes be desirable. Also, it is desirable to have no mesh dependency. By damping the solution algorithm with the regularization factor α, one obtains an improved solution shown in Fig. 6.11 with less mesh dependency. One can see that the damping has little influence

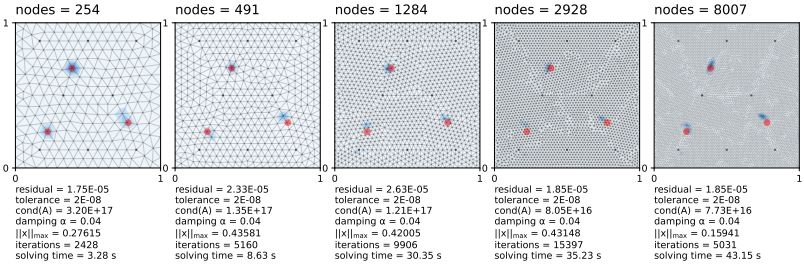

Figure 6.11: Comparison of damage localization for different mesh refinements with damping the trust region reflective algorithm.

on the results of the coarse meshes, but for fine refinements, the result is no longer a punctual localization. One can also see that with increasing mesh refinement, the solving time increases. For the undamped problem, the times increase over-proportionally. For the damped problem, overall solving times are smaller, and the increase of solving times for finer meshes is less.

The model with 491 nodes has an average node distance of 0.05 m, which is also the mean scattering free path l. With the underlying assumption of multiple scattering, l also describes the accuracy of imaging with CWI. The

refinement study supports this assumption, as the finer meshes lead to similar damage extensions. Therefore, a recommended choice is a mesh refinement with node distances equal to or a bit smaller than the mean scattering free path l.

6.1.8 Study on Simulation Time Step

Regarding the simulation time step, it is essential to differ the simulation to obtain the synthetic coda signals and the FEM-based diffusion simulation to obtain coda wave sensitivities in a homogenized material. The performed study investigates the time step for the latter. Usually, the solution is expected to improve with finer discretization in space and time. However, with an inverse problem and a diffuse model relating measurements and simulation, significant post-processing steps can affect an expected improvement with reduced time steps. This can be seen in the results of Fig. 6.12.

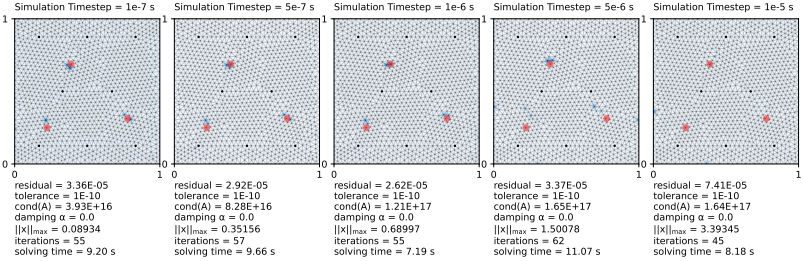

Figure 6.12: Comparison of damage localization for different simulation time steps.

The time step of $t = 1 \times 10^{-6}\,s$ results in the lowest residual. For smaller time steps, the localization also works very well. Only with larger time steps does the solution worsen. A possible reason for the failed localization with $t = 1 \times 10^{-5}\,s$ is a CFL number larger than one for the given setup, which can result in numerical instabilities for the given problem. In order to have an efficient simulation, the time step is chosen as large as possible, and thus $t = 1 \times 10^{-6}\,s$ is an ideal choice for the used diffusivity.

6.1.9 Remarks on the Computational Effort

Computations were performed on a machine with an 8x3.70 GHz CPU and 64 GB RAM. The used open-source project KRATOS Multiphysics [128] for solving the diffusion problem is implemented in C++ with a Python shell. The sensitivity kernel computation is implemented in Python. The diffusion problem must be solved for each transducer to construct the sensitivity kernel. For the numerical experiment, that is eight times solving a problem with 1284 nodes, 2434 elements, and 2216 time steps. Computation times were

11:54 [mm:ss] for the diffusion problem (avg. 89 s per transducer). This expansive computation can be performed in advance.

Compared to values given in Grabke et al. [110], the computation times for the sensitivity kernel reduce drastically. Previous implementations computed sensitivities for every time step of the diffusion simulation, which is not required for the damage localization problem that only requires sensitivities for corresponding DC measurements. The resulting reduced computation time for 280 measurements is 0.524 s. Solving times for the inverse problem are given in each figure and are strongly influenced by parameters such as damping or tolerance, which is the residual change per iteration step.

6.2 Damage Localization at a Real Large Scale Concrete Specimen in a Laboratory

6.2.1 Experimental Setup

This section tests the coda wave-based damage localization in a laboratory experiment. Parts of the results are published in Grabke et al. [110, 129]. Investigated is a real reinforced concrete specimen with a four-point bending test conducted by the Institute of Concrete Structures at the Ruhr University Bochum. The experiment is very similar to the one described in detail by Clauß et al. [130] (cf. Fig. 6.13) except for increased specimen dimensions that can be seen in Figure 6.14. The embedded ultrasound transducers are described in Sec. 4.8 and are installed before casting the concrete with clips attached to the reinforcement bars.

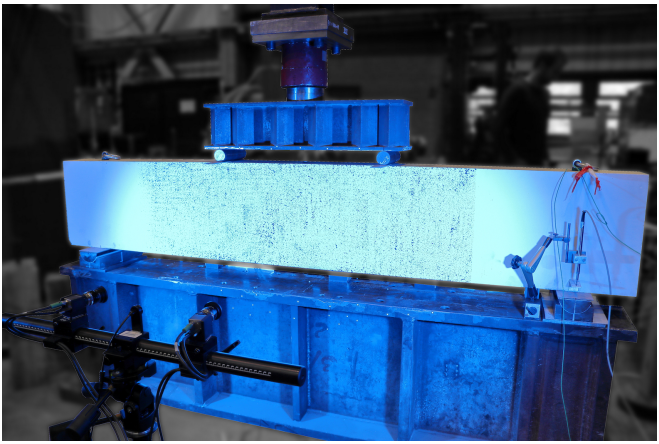

Figure 6.13: Test setup of the very similar four-point bending test conducted by the Institute of Concrete Structures at the Ruhr University Bochum [130].

The loading is stepwise increased. During the first 20 loading steps, the force increases with 5 kN and then with 10 kN until failure. With this setup, the average tensile strength of the used concrete f_{ctm} is exceeded after ten load steps, so cracks should appear around this load step. Next to the CWI, a FOS is used to monitor cracks. Further details on the FOS can be found in Clauß et al. [130] and Sec. 6.2.2.

The ultrasonic signal is a Gaussian pulse with a central frequency of 60 kHz. In order to compensate for phase shifts, e.g., from the acoustoelastic effect [8], the signals are stretched before the correlation evaluation. The CWI evaluation is divided into two types. First, a CC evaluation over the different load steps (Sec. 6.2.3) and then a DC based damage localization for different

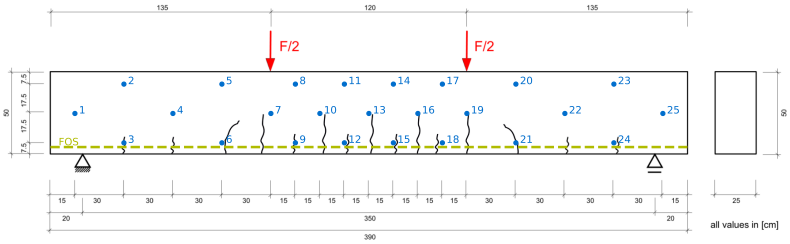

Figure 6.14: Overview of the experimental setup. Blue dots show the 25 embedded ultrasound transducers, and green marks the Fiber Optic Sensor. Black lines on the bottom of the specimen indicate the fully developed crack pattern.

fixed load steps is performed (Sec. 6.2.4). The results for damage localization at all load steps are attached in the appendix.

In total, 25 embedded ultrasound transducers that measure 104 combinations are used. The coda signals, however, immediately showed complications that can appear in real applications. In Fig. 6.15, one can see a bad measurement compared to a typical signal.

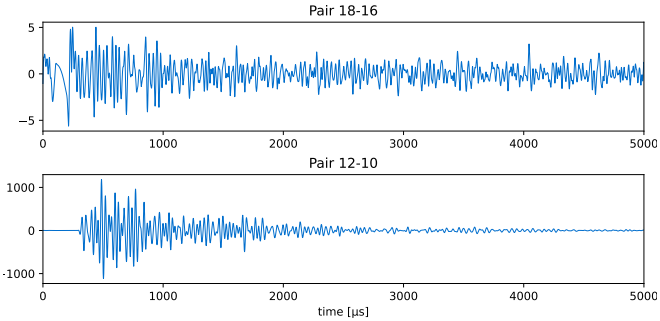

Figure 6.15: Example of a bad signal (pair 18-16) compared to a typical signal (pair 12-10).

Reasons for such failures are often hardware-related and, with transducers embedded into the concrete, are only sometimes fixable. Cracks may also run into the transducer positions during the loading process, which may also degrade the reproducibility of the signal. In this experiment, a malfunction was identified for transducer 16 working as a receiver, and related measurements were thus taken from the data set.

6.2.2 Evaluation of the Fiber-Optic Measurements

FOS is an established strain-measuring technology. In the experiment, a fiber is placed along the reinforcement bars at a height of 44 mm from the bottom. In case of cracking in the concrete, the reinforcement bar is activated and stretched over-proportionally. This stretching can be seen as peaks in the FOS measurements. Thus, the FOS is a sensitive technology for measuring cracks along the x-axis. However, it does not give direct information about the crack width, direction, and extension in the y- and z-direction. The x-coordinates are nevertheless beneficial information to better understand CWI data with increasing load (Sec. 6.2.3) and to verify the damage localizations of Sec. 6.2.4. Fig. 6.16 shows the FOS measurement of selected load steps. The raw measurement data is smoothened with a Savitzky–Golay filter [131] for the visualization.

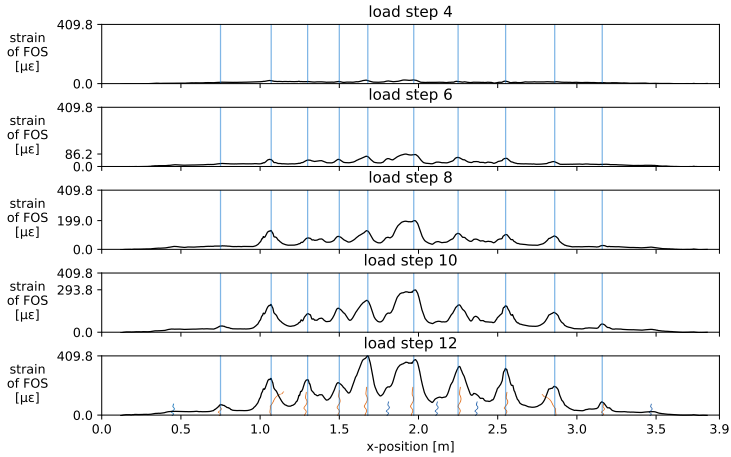

Figure 6.16: FOS measurements of selected load steps.

One can see that the overall strain increases with increased load and that the first indications for the crack positions can already be seen at load step 6. In the figure of load step 12, the final crack pattern is also shown. Orange marks cracks seen in the FOS measurement, and blue marks little cracks that form at later load steps. As explained in the following Sec. 6.2.3, a stepwise updated reference measurement for CWI is used. This means that the reference measurement is always the previous one. Since only changes compared to the reference state are detectable, cracks are most easily detected when they form. If cracks already exist and are, e.g., increasing, they might still be detectable. Fig. 6.17 plots the FOS changes between each load step, which is equivalent to the stepwise CWI measurements.

One can see that the maximum difference in strain increases with the load steps. One can also see that the biggest changes at each load step move from the middle (e.g., load step 10) towards the outside (load step 12). The

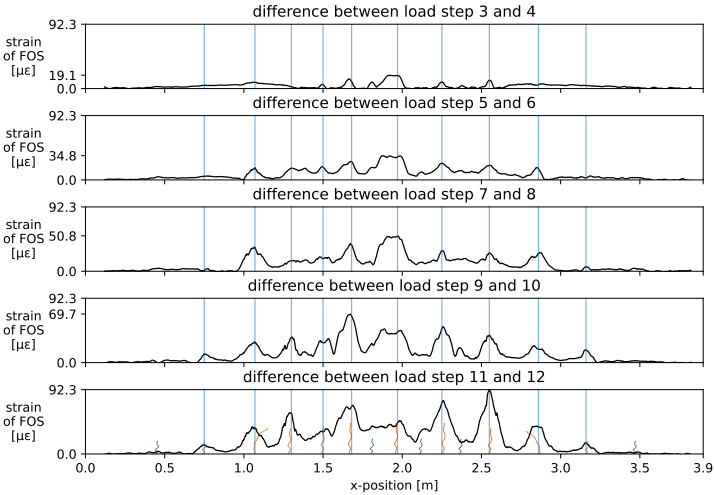

Figure 6.17: Difference in the FOS measurements between selected load steps.

changes at the middle crack near x = 2 m even decrease after load step 10. This decrease indicates that the crack formation is finished, the reinforcement fully activated, and cracks towards the outside increase. Noteworthy is also that in the very early loading phase at load step 4, there are already indications for the five cracks in the middle, which is surprising because the average tensile strength of the used concrete f_{ctm} is exceeded after ten load steps.

6.2.3 Correlation Evaluation over Time

In order to get an overview of the measurement data, the overall signal correlation is evaluated over the time of the experiment. There are two established approaches for computing the CC: a fixed reference and a stepwise updated one. In the stepwise approach, the measurement is always from the previous load step, meaning only cracks and other changes happening in this one load step are detectable. A comparison of the CC evaluation for the two approaches is shown in Fig. 6.18.

One can see that with the fixed reference and increasing load, the CC in general only decreases. This is not true for the stepwise CWI evaluation. Here, maximum changes in the medium appear around load steps 9 and 17. Before load step 9, there are also little CC drops already. For the fixed reference, however, the correlation of selected measurements drops significantly with the first load step. A central assumption of CWI is a good reproducibility of signals, their diffuse tails, and the occurrence of little changes in the medium. With CC dropping down to about 0.2 at selected measurements, the general reproducibility is no longer given. The assumption of little changes is also

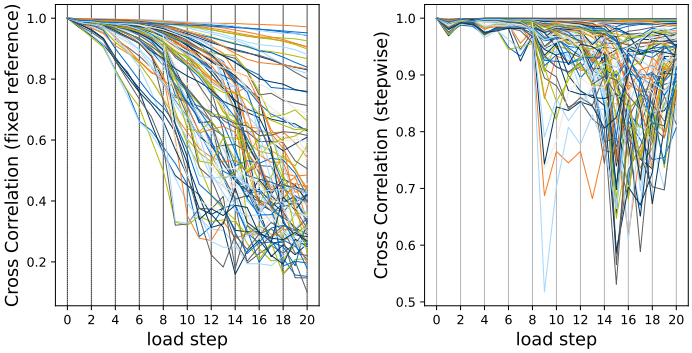

Figure 6.18: Comparison of CC for fixed and stepwise updated reference measurements.

more than questionable, with multiple cracks appearing. Thus, the stepwise updated reference is the only applicable technique for the experiment. Fig. 6.18 also clearly shows the large amount of measurement data. In order to better understand the CC development depending on the position of the measurement pair in the specimen, Fig. 6.19 gives the CC measurements of selected pairs together with an overview that also includes the crack pattern. The selected ten pairs of Fig. 6.19 are chosen such that different positions on the specimen are represented, but the focus is still on the area with cracks developing. Also, pairs are chosen symmetrically except for pair 18-21, whose CC development is special. Overall, the CC developments are comprehensible but contain surprises. Starting with zones far from the damage zone, one can see that the CC of pair 4-1 and 22-25 are nearly unaffected. Pairs 8-17 and 14-11 are in the middle but at the top, show comparable little developments during cracking. However, cracks are noticed around load step 8 and later. Pair 7-19, which is also in the middle but at middle height, shows similar development compared to the pairs at the top, but with cracks developing, shows larger CC drops. The pairs at the bottom outside 12-3 and 24-15 show similarities up to load step 14 and then developments differ. Pair 12-3 shows CC drops to 0.7, whereas 24-15 remains around 0.9. Here, the influence of a crack position in relation to the transducer position is probably significant. This can especially be seen with pair 18-21, which shows a large CC drop at load step 9. One would expect comparable or larger CC drops for the pairs in the bottom middle. However, looking at the crack positions, one can see that a crack is going into the mounting position of transducer 21. This change, close to a transducer, dramatically influences the CC. One can also see this in the sensitivity kernel, which forms sharp peaks at the transducer positions. However, the peak in the sensitivity kernel is so sharp that the value of the measured correlation and the model might still significantly differ, which can lead to problems in the damage localization (cf. Sec. 6.2.4.6). As expected, the pairs in the bottom middle show significant CC changes. The

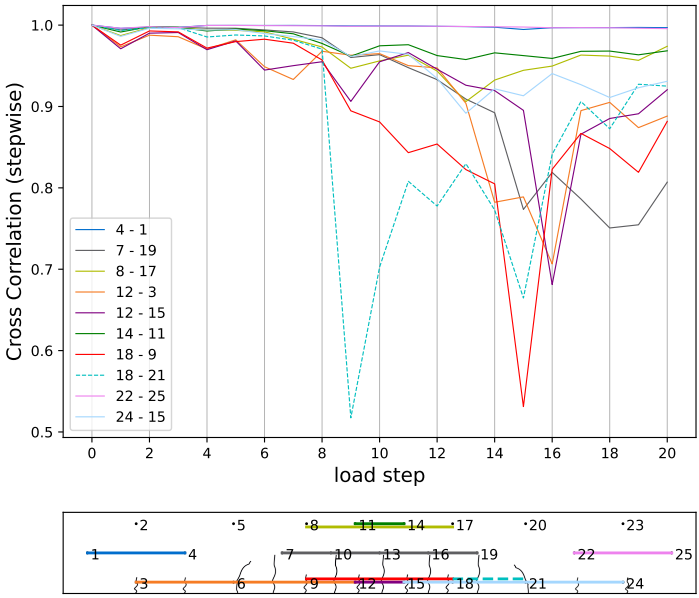

Figure 6.19: CC evaluation of selected pairs with a graphical overview of the position in the specimen below.

pair 18-9 that senses the whole middle third shows a very continuous CC development. There is only one significant drop at load step 15, and since pair 18-21 also shows a significant CC drop, there is most likely a crack going into the mounting position of transducer 18. The same can be seen for transducer 12 at load step 16. Like the FOS measurements, the CWI also detects the first changes in the bottom area around load step 4. This early detection again shows the high sensitivity of the CWI technology and the immense potential that comes with it. However, cracks in the transducers' mounting position strongly influence the measurements and can cause inconsistencies.

6.2.4 Damage Localization

6.2.4.1 Procedure in Previous Publications

The FEM based damage localization procedure is generally based on Grabke et al. [110]. The final result of the study was reproduced with the updated code used for the present evaluations and is shown in Fig. 6.20.

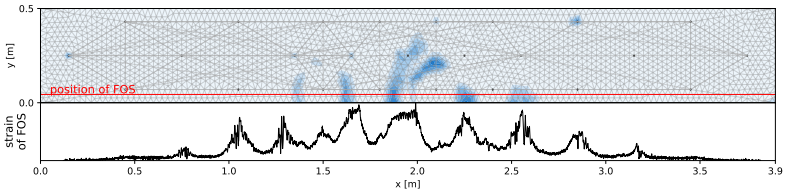

Figure 6.20: Damage localization for the time of crack formation with settings according to Grabke et al. [110]. The blue color shows located damage. The black curve below shows the strain measured with FOS, and peaks indicate cracks.

Of particular note are three changes compared to Grabke et al. [110] that resulted from the ongoing research. One is the manual selection of useable measurement data. This selection was required because using the complete measurement data set would result in damage localization at selected transducer positions. The assumed main reason for this is the cracking into the mounting position of transducers, as discussed in Sec. 6.2.3. In order to avoid data filtering, the sharp peaks of the sensitivity kernel at transducer positions are modified so that damage localization does not tend to transducer positions anymore. Further details are given in the following Sec. 5.2.3. The second specialty was the superposition of several damage localizations at different load steps. This procedure is generally an excellent way to reduce the influence of mislocalization and sharpen the localized crack positions. The procedure is, however, conditionally applicable for practical application, and thus, this thesis tries to avoid such a superposition. A third change is the solution algorithm. In Grabke et al. [110], the `scipy.optimize.lsq_linear` algorithm is applied. As previously indicated, that solver tends to find a punctual localization if not damped. In Grabke et al. [110], the damage region's extension was controlled with a threshold on the solution. This maximum threshold is very individual and requires a calibration performed in Grabke et al. [110] during an early loading state. When adding a damping term, as done in this thesis, the punctual localization can be avoided; thus, an individual calibration is no longer necessary.

6.2.4.2 Diffusivity Evaluation

The diffusivity is the main homogenization parameter describing the intensities of a measurement. For real measurements, the envelope fitting of Sec. 5.1.7

is a good tool for determining the diffusivity. Fig. 6.21 plots the determined diffusivity over the transducer distance.

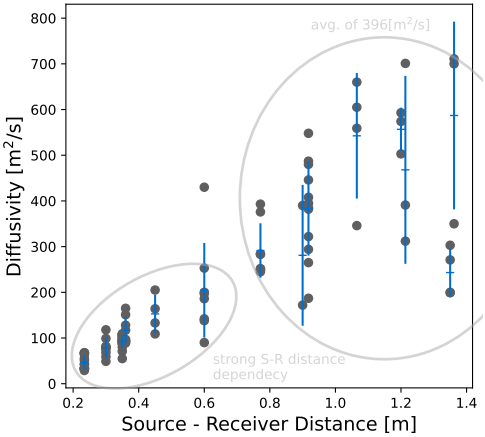

Figure 6.21: Diffusivity from envelope fitting over source-receiver distance. Blue lines show the standard deviation.

One can see a strong dependency on the distance, especially for the short source-receiver distances. That is because of the clearly visible ballistic parts of the waves that can also be seen in Fig. 4.3. Therefore, the envelope fitting does not form an envelope around the peak from diffusion but the peak of ballistic p- and s-waves. Starting around a source-receiver distance of 0.8 m, the variance of the evaluated diffusivities increases, and there is no longer a strong dependence on the source-receiver distance. An explanation could be that for the used concrete combined with a central frequency of 60 kHz, the transport mean free path at which the wave loses all its directional information is around 0.8 m. This distance is equivalent to a transport mean free time of $\approx 190\,\mu s$ for p-waves and $\approx 330\,\mu s$ for s-waves.

Next to the used multiple scattering based coda wave sensitivities Pacheco et al. [132] also define single scattering based coda wave sensitivities. These are based on the assumption of only one uniform scattering from source to receiver. The prevailing physical behavior of 60 kHz ultrasound in concrete is likely no isotropic scattering. Therefore, the transport mean free time in the medium is more critical than the amount of scattering events. After this time, the wave spreads diffusively and creates a state where multiple scattering-based techniques are applicable. The evaluated signals have a length of 2000 µs after arrival, which, together with the transport mean free times given above, means the majority of the signal arriving comes from a diffuse wave field. Therefore, the multiple scattering-based computations of sensitivities should be applicable. For the approximation of all signals with the diffusion problem, a diffusivity of $400\frac{m^2}{s}$ that is following values from

literature (Fröjd [133] used $440\frac{m^2}{s}$ for a 50 kHz signal) is used. This value also matches the average of $396\frac{m^2}{s}$ of all signals above a source-receiver distance of 0.6m̀ (so larger than the assumed transport mean free path).

6.2.4.3 Simulation Settings

It is assumed that the crack development is uniform over the specimen width. Thus, the specimen is simplified to a 2D model, significantly reducing the computational effort. The choice of settings for the damage localization strongly depends on the expectations. The damage localizations in Grabke et al. [110] focused on precision, which is possible for a laboratory experiment with controlled parameters and reference measurements where the expected output is known. Therefore, one can distinguish false results from good ones. In practical applications, reference measurements with increased accuracy and robustness are usually not given. Thus, the CWI must be as robust as possible. A second goal of this experiment is also to find application boundaries. Settings are chosen to avoid manual filtering of the measurement pairs. A complete overview of the used settings for the damage localization presented in the following sections is given in Tab. 6.3.

6.2.4.4 Calibrations at Early Load Steps

In order to find application boundaries of the CWI for damage detection, the evaluation is split into three parts: before, during, and after crack formation. This section investigates load steps 5 and 8 before the computed reach of the concrete tensile strength. As one can see in the FOS measurements of Fig. 6.17, there are already changes happening and indications for the crack positions. In Fig. 6.18, the CC measurements are relatively little, but a slight increase can already be seen in the stepwise evaluation. With the assumption of small changes that can be detected, the early load steps are regarded as the best choice for calibrating the clipping threshold for sensitivities. Fig. 6.22 and Fig 6.23 show imaging results of this parameter study.

In general, one can see a strong effect of the sensitivity manipulation. Without modifications, the position of transducers is located. This problem is avoided by clipping the sensitivities. The lower the threshold is chosen, the larger and smoother the located damage field becomes. By clipping the sensitivities at a specific value, there is a loss of information, but the solution improves until a certain point. This is probably related to the quality of the measurement data and its fit to the simulated sensitivities of the waves. Comparing the different sensitivity thresholds, a clipping at $\frac{1}{6}$ of the maximum value appears to give the visually best solution. This threshold on the sensitivities is also applied to all further investigations. Fig. 6.24 shows sensitivities of the measurement pair 10-16 with a clipping at $\frac{1}{6}$ of the maximum value.

Experiment parameters	
Central frequency of Gaussian pulse	60 kHz
Amount of useable measurements	99
Specimen dimensions	3.9 m × 0.5 m
Range of source-receiver distances	0.23 m - 1.36 m
Simulation parameters for damage localization	
Intensity computation	FEM-based (Sec. 5.1.4) + Improvements of Sec. 5.1.5
Sensitivity modification	values for each measurement clipped to 1/6 of the maximum sensitivity
Average node distance of the mesh	0.03 m
Number of nodes	2473
Simulation time step	1×10^{-6} s
Diffusivity	$400 \frac{m^2}{s}$
Evaluated signal length (after tof)	2000 µs
Decorrelation window length T	400 µs
Reference measurement	step-wise updated
Signal stretching window length T	250 µs
Solving algorithm	Trust Region Reflective Algorithm (Sec. 3.6.2)

Table 6.3: Overview of the simulation parameters for damage localization at the real experiment.

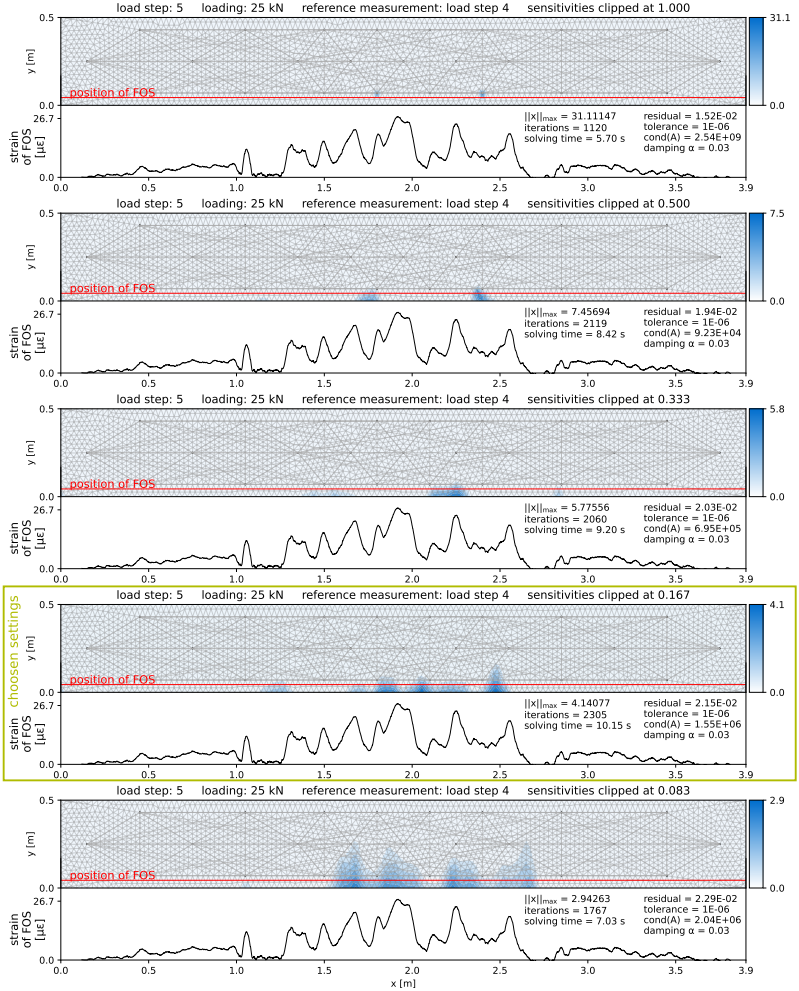

Figure 6.22: Damage localization at load steps 5 with different thresholds on the sensitivity. The blue color shows located damage. The black curve below shows the strain change of FOS measurements compared to the previous load sets. Peaks in the FOS measurements indicate cracks.

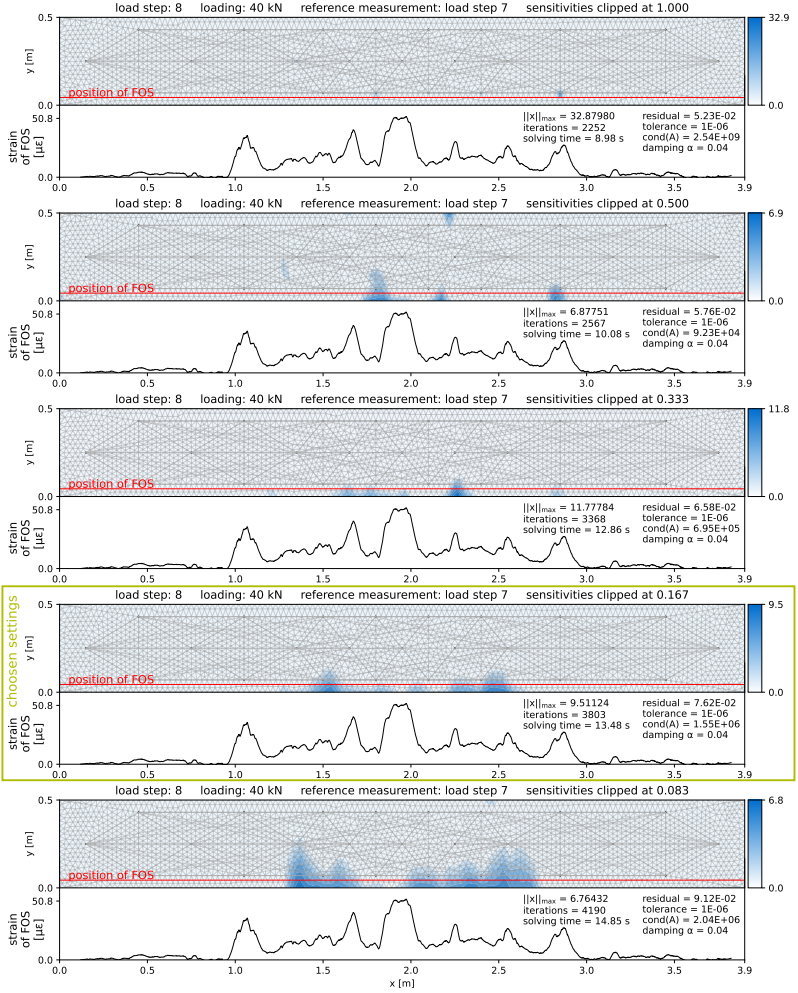

Figure 6.23: Damage localization at load steps 8 with different thresholds on the sensitivity and visualization as in Fig. 6.22.

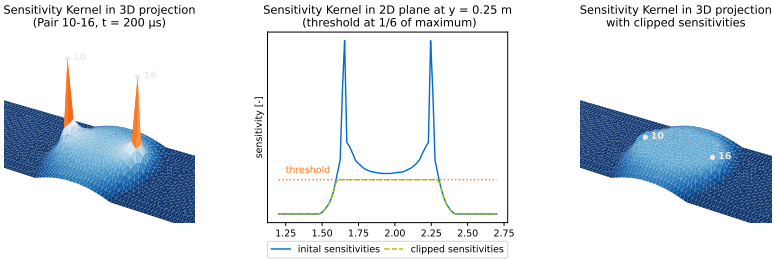

Figure 6.24: Exemplary sensitivities of a measurement pair at the real large-scale concrete specimen.

The characteristic of clipping at a low threshold is a plateau in the direct path region that becomes larger as the evaluation time within the signal increases. The magnitude of the clipping threshold may be related to factors such as central frequency, source-receiver distances, and the density of the measurement network. In this experiment, there is a high density of sensor pairs, which could explain why it is still possible to detect at good accuracy despite losing a lot of sensitivity information due to a low clipping threshold. Another explanation of the effect the clipping has can be described with the typical sensitivity development illustrated in Fig. 5.8. The most crucial factor for the fitting process is the shape of the sensitivity kernel development over time. When comparing the development at the position of the transducer (blue curve) and in the middle of the two transducers (orange curve), one can see that the shapes are both convex and quite similar. The least-squares fitting uses these curves and a scaling factor to match the measurements. In case a measurement develops in a convex way as the blue and orange curves do, it would thus be possible to fit with the blue curve but also the orange curve. The very strong influence of the transducer position in the end leads to pointwise localizations at the transducers. The clipping leads to a similar development of all points on the clipping plateau that, in the end, creates a smoother and more satisfying localization.

Next to a calibration of the sensitivity clipping threshold, the damping of the solution algorithm needs to be adjusted. This is again done with the L-curve method of Hansen [60] (Sec. 3.4). The L-curve of load step 5 with the final settings is shown in Fig. 6.25 and results in a damping of $\lambda = 0.04$. The L-curve method was also conducted at all other load steps, resulting in similar damping factors. This makes sense as the damping primarily affects the sensitivity matrix that is constant for all load steps.

6.2.4.5 Damage Localization in Early Loading Phase

With a completed calibration, the three stages before, during, and after crack formation are now discussed in more detail. This section investigates the green framed plots of Fig. 6.22 and Fig. 6.23 at load steps 5 and 8 that are before the computational reach of the concrete's tensile strength.

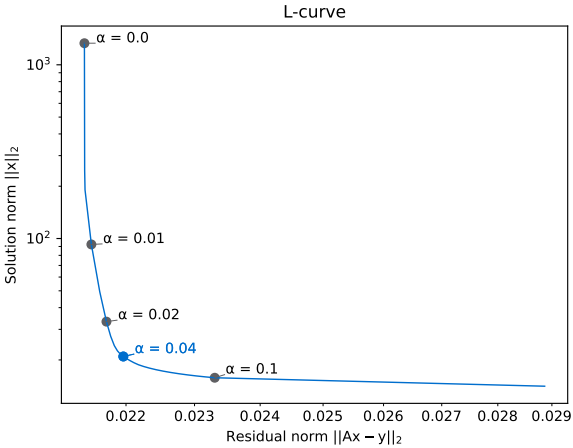

Figure 6.25: L-curve of Hansen [60] at load step 5.

Even though CC measurements are relatively little, the damage localization already leads to surprising results. At load step 5, the damage localization detects a damaged area in the middle third. The extension of this detected area is in good accordance with the peaks of the FOS measurement. Several differences in the damage field indicate multiple cracks and are in approximate accordance with the cracks detected by FOS, which is an excellent result. At load step 8, multiple sharp peaks exist in the FOS measurements. The damage localization correctly identifies the bottom middle area, but the extension towards the sides lacks a crack on each side with the chosen settings. The difference in magnitude of the located damage field also does not match the FOS measurements at all peaks. Especially at x = 1,9 m, a significant damage is not located. Despite missing precision, the localization is nevertheless very robust with the settings. Also, the magnitude of the localization makes sense when comparing values of Fig. 6.22 and Fig 6.23.

The results at the early load steps underline the large sensitivity of coda waves to little changes and consequently the immense potential of CWI as an early damage detection technology. The enormous sensitivity comes from the wave scattering that results in a large sensing area and the evaluation of later parts in the signal where little changes have increased visibility. In this early loading phase, a major requirement for CWI of good signal reproducibility is also fulfilled with CC coefficients larger than 0.9 for all signals.

6.2.4.6 Damage Localization at Time of Crack Formation

At first glance, the time of crack formation is the most interesting because most irreversible changes that should be detected occur. The FOS evaluations

in 6.16 show no clear load step when the cracking happens. The time of crack formation is thus defined here as when the computed tensile strength of concrete is reached, which is at load step 10. Fig. 6.26 shows the CWI damage detection results.

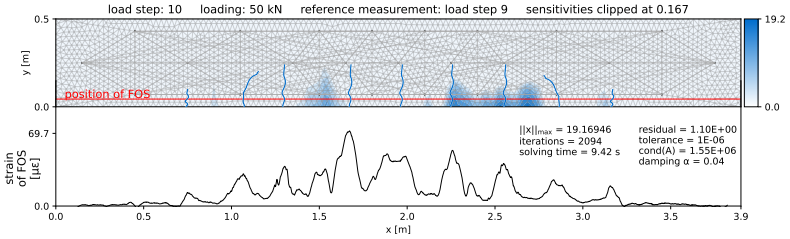

Figure 6.26: Damage localization at load step 10 with content visualized as in Fig. 6.22.

Several parts are correctly detected, but there are also two areas (middle and left) where the damage identification misses a few cracks. The CC in Fig. 6.18 and Fig. 6.19 already indicated that with macro cracks appearing, the quality of selected measurement pairs drastically decreases. These pairs with bad reproducibility of signals are also part of the evaluated data set and can have a strong influence. Therefore, pairs with a CC worse than 0.9 (in total nine pairs) are filtered out for the damage localization in Fig. 6.27.

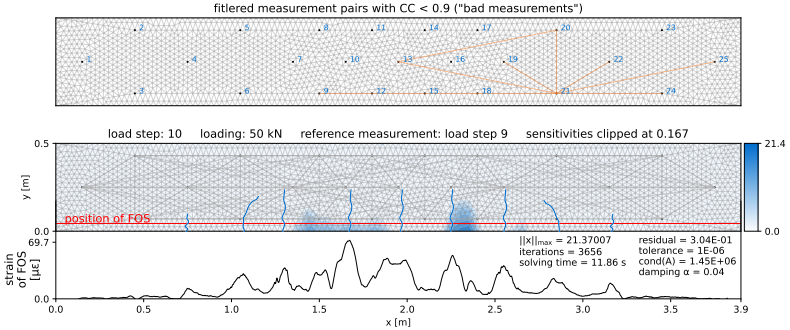

Figure 6.27: Damage localization at load step 10 with content visualized as in Fig. 6.22 and only pairs that have a CC > 0.9.

The simple filter for measurement quality improves the result a little. Despite the cracked area near x = 1.9 m that was also not visible at load step 8, there is a good identification of the damage zone in the middle. Overall, the solution procedure appears very robust, with or without a filter on the measurement quality.

When comparing the magnitude of the maximum value of the solution to load step 8, one can see a clear jump. This also becomes visible when plotting the maximum value of all load steps, as shown in Fig. 6.28. Very important

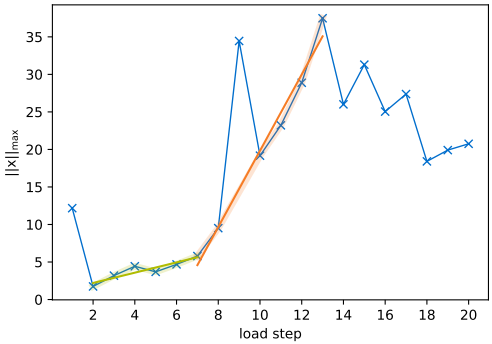

Figure 6.28: Development of $||x||_{max}$ for the first 20 load steps.

for this evaluation is to also take the actual plot of the damage localization into account. All plots are attached in Appendix A. With the actual solution plot and the CC developments of Fig. 6.18, one can, e.g., explain the outlier in Fig. 6.28 at load step 9 with the over-proportionally large decorrelation related to transducer 21. When neglecting the outlier, one can identify two trends highlighted in green and orange. Until load step 7, there is a nearly linear increase with a slope of approximately 0.14 [1/kN]. From load step 7, the trend changes, and until load step 13, the increase is also nearly linear but with a slope of approximately 1.02 [1/kN]. When comparing with the FOS results of all load steps shown in the appendix, one can see that until load step 6, there is a rather diffuse field of cracks, and at load step 7, three sharp peaks become visible in the FOS measurements, which might indicate the first macro cracks. In the FOS data of the appendix, one can also see that after load step 13, the sharp peaks become once again more diffuse, which could explain why the trend from load step 7 to 13 no longer continues. Summarized, one can say that analyzing trends in the $||x||_{max}$ development has immense potential for differentiating micro and macro cracks and, thus, different damage states and should be further investigated. However, this is only possible in a laboratory setting with controlled load increase that is typically not given for a practical field application.

In order to get a feeling about the fit of measurement data and the simulated model, the least-squares fitting is evaluated for selected pairs in Fig. 6.29. What is shown is the left-hand side (LHS) and right-hand side (RHS) of the inverse problem to be solved (cf. Eq. 5.20). The LHS represents the simulated model multiplied with the solution of Fig. 6.27, and the RHS represents the measurement data to be fitted. A good fitting is possible if lines of the same color are close together, indicating a good model. One can see that overall trends in the four curves match, which, together with a satisfying solution,

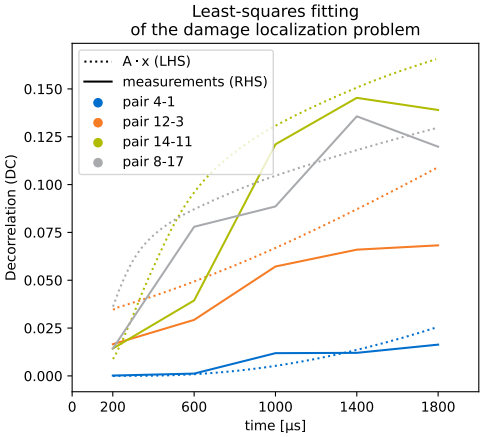

Figure 6.29: Visualization of the least-squares fitting of selected measurement pairs for the damage localization of Fig. 6.27.

proves that it is possible to perform a damage localization with a central frequency of 60 kHz and a model based on the diffusion analogy.

6.2.4.7 Damage Localization After Completed Crack Formation

A major question next to the detection of new cracks is the detection of existing cracks. With a stepwise updated reference, the expectation is that existing damage is not detectable as long as the crack does not extend. This section investigates load steps 15 and 18, and results are shown in Fig. 6.30. At these load steps, the crack pattern in the middle is fully developed, and further cracks develop and increase closer to the supports. The CC values at the two load steps are comparatively small, as one can see in Fig. 6.18 and Fig. 6.19 but unlike load steps 9 and 10 overall plausible.

In the FOS measurements of Fig. 6.30, one can see that the peaks moved to positions further away from the middle area. In the middle, there is sort of a plateau indicating a constant strain, which means cracks are fully developed but open up. The damage localization with CWI shows remarkable results. The damaged area's extension is described pretty well. This is surprising since the relative measurement makes existing damage challenging to detect. At load step 15, one can see good correlation to the tiny peaks in the FOS. Only on the right is a peak that is not located. Instead, a mislocalization appears further to the right.

At load step 18, individual cracks seem no longer detectable. One central assumption of CWI is the appearance of only little cracks, and with many measured correlations dropping down to 0.7, this is most likely no longer fulfilled. Thus, it is more than questionable that the used sensitivities of the homogenized material correctly describe the measured physical phenomena,

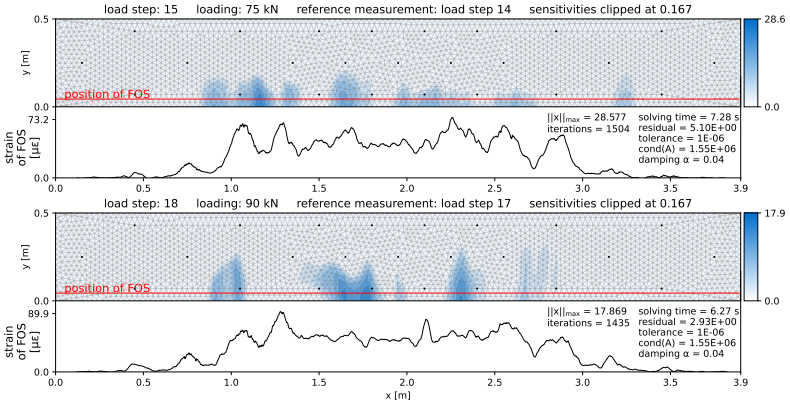

Figure 6.30: Damage localization at load steps 15 and 18 with content visualized as in Fig. 6.22.

which would explain why individual cracks are no longer detectable. Despite a rough description of the damaged area, individual cracks are not detectable, which underlines the application boundary for detecting existing cracks. In general, this is a disadvantage but can be advantageous for structures that are designed to have zones with cracked concrete in certain parts.

Concluding the damage localization at an actual experiment under controlled conditions, the results are promising. With the little modification of clipping the peaks in the sensitivity kernels, the overall goal of a robust CWI based damage detection is fulfilled. It is a significant improvement compared to Grabke et al. [110]. The evaluation at early load steps also shows the immense sensitivity of CWI to slight changes, and the correct identification of damaged regions at late load steps underlines the robustness. The detection of existing damage is identified as an application boundary. All damage localizations are qualitative results. The next step points towards a damage quantification that can trigger an alarm. One possible method shown is the analysis of trends of the solution's maximum value for increasing load.

6.2.5 Further Investigations

6.2.5.1 Influence of the Used Diffusivity

Due to the large variations of the diffusivities obtained from envelope fitting of the signals shown in Fig. 6.21, the used value is further investigated. The used $400\frac{m^2}{s}$ is in accordance to values from literature (Fröjd [133] used $440\frac{m^2}{s}$ for a 50 kHz signal). Different diffusivities are tested to investigate the effect of diffusivity on the final damage localization result. Fig. 6.31 shows the result for a damage localization with $D = 100\frac{m^2}{s}$, $D = 200\frac{m^2}{s}$,$D = 400\frac{m^2}{s}$ and $D = 600\frac{m^2}{s}$ for an evaluation at load step 10.

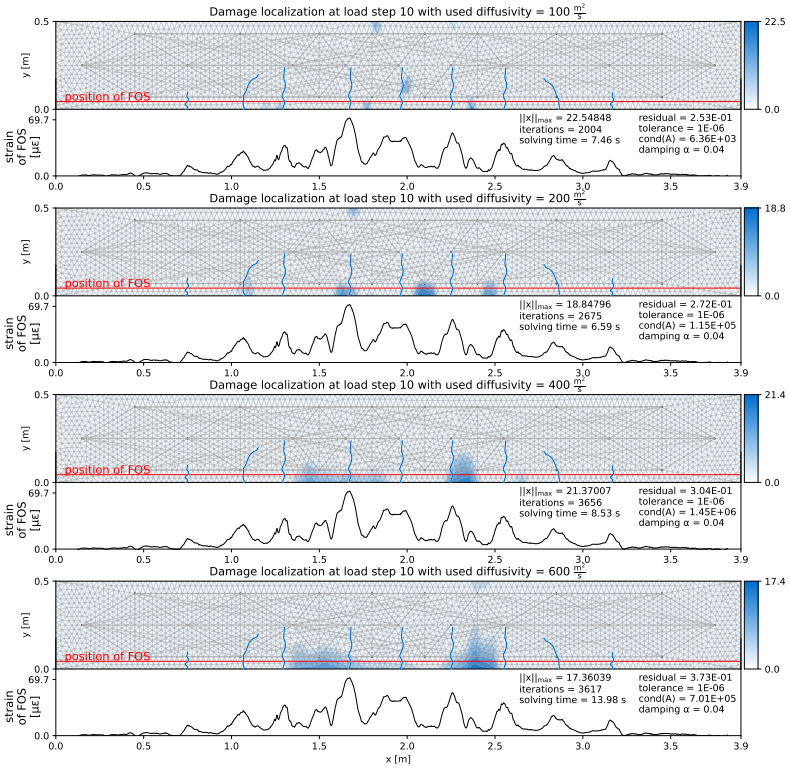

Figure 6.31: Evaluation of the effect of the used diffusivity on the damage localization result at load step 10.

The comparison shows that the used $400\frac{m^2}{s}$ are a good choice, but also, with $200\frac{m^2}{s}$, several cracks are located correctly. Therefore, load step 5 with smaller changes to be detected is also investigated in Fig. 6.32. The diffusivity

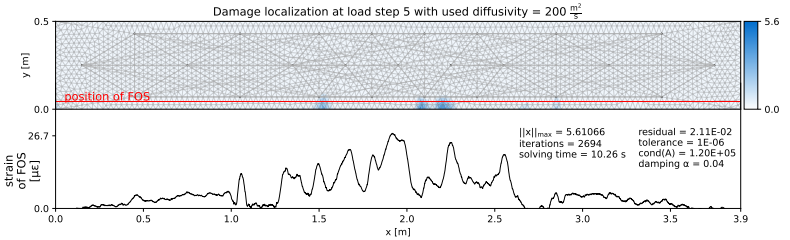

Figure 6.32: Damage localization at load step 5 with content visualized as in Fig. 6.22 and a diffusivity of $200\frac{m^2}{s}$.

study shows that the damage localization also works with $200\frac{m^2}{s}$, but $400\frac{m^2}{s}$ is overall a better choice. The diffusivity used, of course, changes sensitivities. However, in the end, the spatial relation of the sensitivities changes less than the variations in the measurement data, and thus, the solving algorithm still works.

Instead of using a fixed diffusivity, it would also be possible to use the individual diffusivities obtained from envelope fitting for each measurement pair. This use of individual diffusivities is ambivalent. On the one hand, the simplification with a diffusive spread is introduced as a simplified description of the signals' intensities (envelope fitting). However, the actual reason why the diffusion analogy is applicable is that the energy of a multiple scattered signal in a heterogeneous media behaves similarly to a diffusive spread in a homogenous media. Thus, the diffusivity is a quantity describing the material in relation to the used frequency and should, therefore, be constant. The obtained strong relation of diffusivities on the source-receiver distance as seen in Fig. 6.21 is nevertheless a discrepancy that might come from the actual scattering behavior of the used 60 kHz as discussed in Sec. 6.2.4.2. The applicability of a fixed diffusivity should be answered with the damage localization for load steps 8 and 10 using individual diffusivities. The result is shown in Fig 6.33.

Individual diffusivities would, in general, drastically increase the computational effort since each pair requires an individual FEM simulation. Therefore, the sensitivity scaling for different diffusivities described in Sec. 6.1.1 is applied.

The results support the assumption that the diffusion analogy describes the heterogeneous material in relation to the used frequency. The localizations are not wrong but significantly worse than with a fixed diffusivity. At load step 8, multiple mislocalizations are symmetric to the x-axis. This symmetry might come from the overall symmetry of the experimental setup. At load step 10, the unusually high decorrelations related to transducer 21 significantly affect

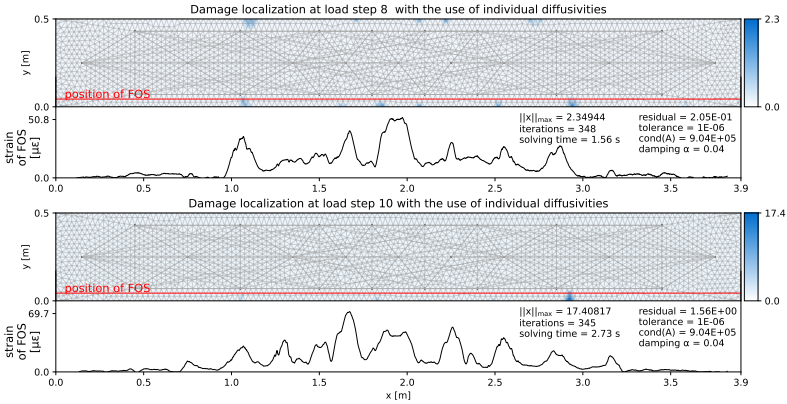

Figure 6.33: Application of individual diffusivities on the damage localization at load step 10.

the result. In total, the diffusivity evaluation shows that the use of a fixed diffusivity is the correct interpretation of the diffusion analogy and for the given setup with a central frequency of 60 kHz, D = $400\frac{m^2}{s}$ is a good choice.

6.2.5.2 Evaluation of Stretching Factor

In general, the coda wave sensitivities explained in Sec. 5.2.1 are a model that describes where the wave most likely obtained its information. As described in Sec. 4.5, there are two main wave phenomena measured in CWI: a phase shift quantified with a stretching factor ε and a waveform distortion quantified with the correlation coefficient CC resp. DC. In the damage localization process, the phase shift is corrected by stretching the signal before evaluating the CC. However, the phase shift can also be regarded as information collected by the signal from source to receiver and, thus, a quantity described by a generalized interpretation of the coda wave sensitivities. This section replaces the DC measurements in $\mathbf{y}$ of Eq. 5.20 with the signals' stretching factor ε. The settings of Tab. 6.3 are used for the damage localization. The only difference is a signal stretching window length of 400 µs to ensure the number of unknowns is identical to the previous damage localization. Fig. 6.34 shows the damage localization results at three of the previous loading stages.

One can see that during the different loading states, the damage localization works. Compared to the results of Sec. 6.2.4, the localization looks even better. Not only is the overall damaged area detected quite accurately, but the detection of nearly all cracks individually works pretty well.

Despite its good correlation with cracks, the damage localization with stretching factors should be cautiously treated. Certain effects are neglected since only measurement data was exchanged, and the rest is identical to the previous localizations. This is because the solving algorithm applies a

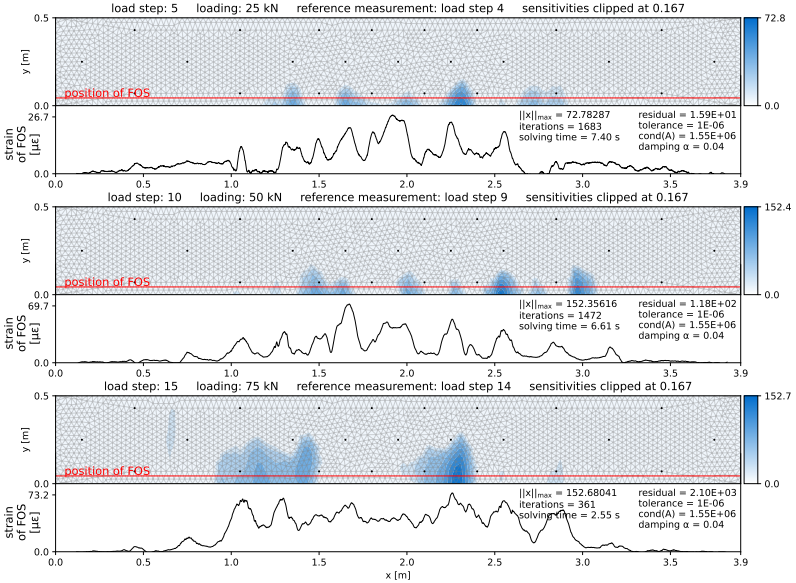

Figure 6.34: Inverse problem-based damage localization at different loading stages with stretching factors ε as measurement data.

positivity constraint on the solution. Since all values are positive, this is valid for DC as measurement data. However, tension and compression areas contribute with a different sign for the stretching. Thus, a solution should also allow negative values. Therefore, the constraint is removed, and the new solution is shown in Fig 6.35. The fact that the results are good despite major neglections raises the question of why the damage localization works. In general, the effects on the stretching factor ε are diverse and not limited to damage but also include phase shifts caused by stress changes. The effects on ε from damages and stress changes are superposed, but since the damage areas are detected, the corresponding effects on ε seem to dominate. In the end, the positivity constraint focuses the solution on the areas under tension whose effects on the signal are dominated by cracked areas. The larger effect of altered concrete compared to healthy concrete is also described by Planès et al. [4].

The damage localization without a positivity constraint in Fig 6.35 gives a plausible solution. The signs of the values change from top to bottom, as is the case with the stresses. The magnitude changes in the tension field are again in good correlation with peaks in the FOS. Only the solution at load step 15 is implausible at three positions where the sign is constant across the cross-section height.

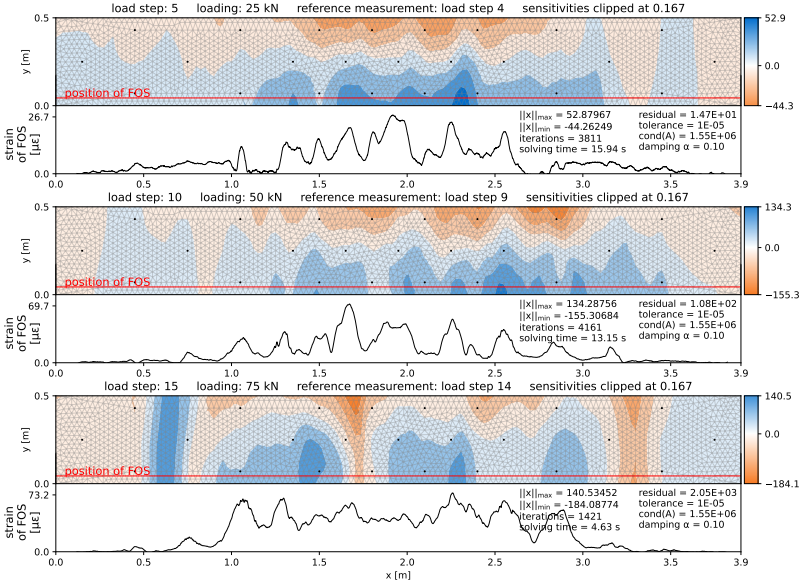

Figure 6.35: Inverse problem-based damage localization at different loading stages with stretching factors ε as measurement data without positivity constraint on solution.

The good results with correct treatment of the solution field underline the high potential of stretching factors as measurement data for damage localization. Since cracks are the main focus, the positivity constraint that focuses the solution towards cracks can be regarded as a beneficial filter. Summarized, the use of the stretching factor evaluated in consecutive time frames as explained in Fig. 4.5 instead of the decorrelation DC is very promising and, together with the underlying generalized interpretation of coda wave sensitivities should be further investigated.

6.2.5.3 Influence of the Measurement Pair Network

The results of Sec. 6.2.4 use a relatively dense net of measurement pairs. In order to investigate the influence of this density on the accuracy of the results, a small study with only a fraction of all active pairs was performed. Fig. 6.36 shows on the top only neighboring pairs in the x-direction active, in the middle only neighboring pairs in y- and diagonal-direction active, and on the bottom a superposition of the top two ones, so all pairs to the neighbor only. Due to the very good correlation of the located damage potions to the FOS measurements, load step 5 is evaluated in this study. The evaluation shows that the damage localization already works with the 21 pairs in the

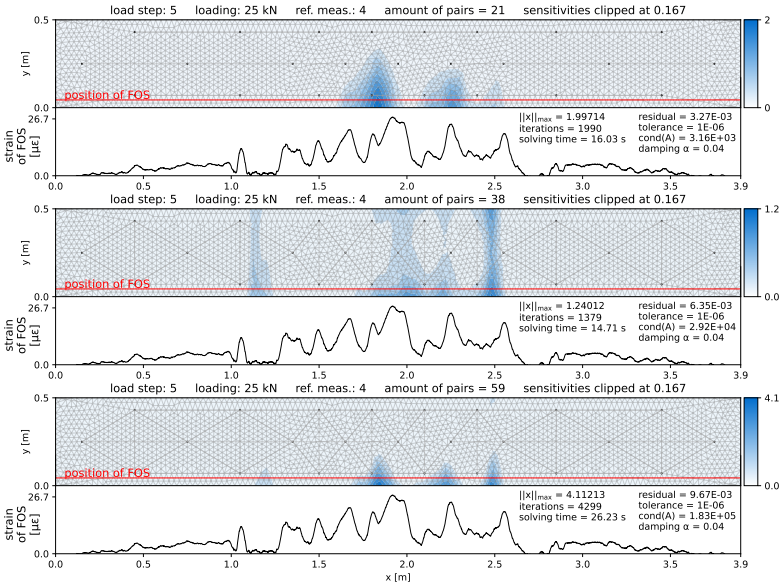

Figure 6.36: Study on the influence of the measurement pair network (short distance measurement network).

x-direction. With only pairs in y- and diagonal directions, the resolution of damage detection over the specimen height is limited. The superposition of all directions sharpens the result of the x-direction-only pairs.

In contrast to the pairs to a neighbor only, Fig. 6.37 uses only pairs to not neighboring transducers in the same subdivision as in Fig. 6.36. The evaluation shows that already, with only nine rather long measurement pairs in the x-direction, a damage localization is possible. The damaged area is accurately described, and even correlations of the solution and the FOS peaks can be seen. Note that the tolerance for this evaluation is decreased by one decimal power. Otherwise, the algorithm would stop after 192 iterations with only rough localization. With the lower tolerance, the algorithm stops after a similar amount of iterations as in the other two pair combinations. The diagonal pairs to non-neighboring transducers are quite flat. Therefore, the difference to the x-direction evaluation mainly lies in the number of measurement pairs and not, as in the previous evaluation, in the directionality. The solution identifies a peak of the FOS that was not detected with the pairs in the x-direction only but misses the correct identification of the damaged area. Combining all directions leads to a promising result, dominated by the solution of the diagonal pairs, as these are in the majority.

When comparing Fig. 6.36 and Fig. 6.37, one can say that the long-distance measurement network identifies the overall damaged region a bit

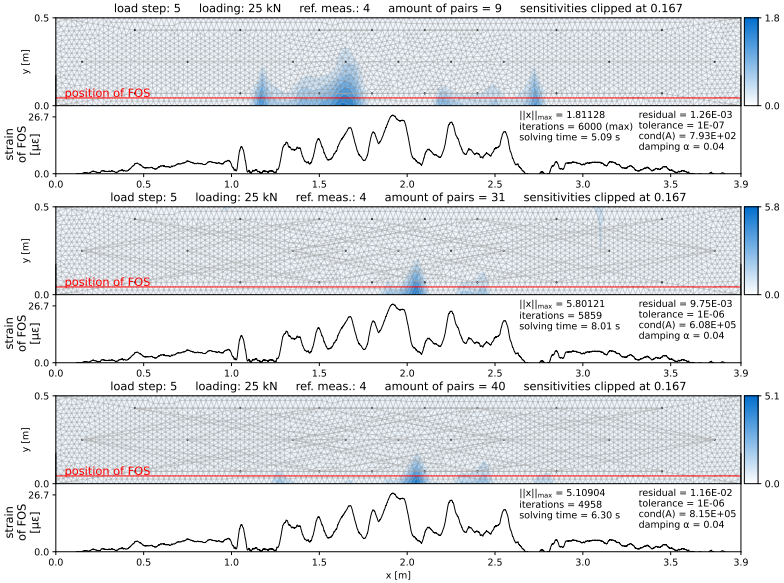

Figure 6.37: Study on the influence of the measurement pair network (long distance measurement network).

better. A possible reason could be that long-distance pairs travel longer than the mean scattering free time and thus fulfill the assumption of the diffuse wave field already at the wave's arrival at the receiver. For short-distance pairs, this is only fulfilled for DC evaluation frames later in the signal. This was also seen in the diffusivity evaluation of Fig. 6.21 that showed a strong source-receiver distance dependency for the short distance pairs. However, the short-distance measurement network also detects several individual cracks quite accurately. Pairs in the x-direction appear more helpful in detecting cracks along the x-axis. This is especially visible with the nine long-distance pairs in the x-direction that allow a good detection of the damaged region. This is remarkable as the inverse problem deals with 2473 unknowns and only nine knowns. Overall, one can say that with more measurement pairs, the solution improves in all cases, and the result of the entire measurement network with 99 pairs (Fig. 6.23) in the end is the best. The study, however, shows the potential of an optimized measurement pair selection in case external factors limit the number of measurement pairs. This is, for example, the case in a practical field application in case a complete measurement set needs to be measured quickly.

6.3 Damage Localization in Large Bridge

6.3.1 Experimental Setup

With the proven applicability of CWI based damage detection at a controlled actual experiment, the next step is applying it to an existing large structure. For this purpose, an approximately 12 m long area in the middle of a large bridge with a span of 82,40 m was instrumented with ultrasound transducers. Fig. 6.38 and Fig. 6.39 give an overview of the bridge and the instrumented area.

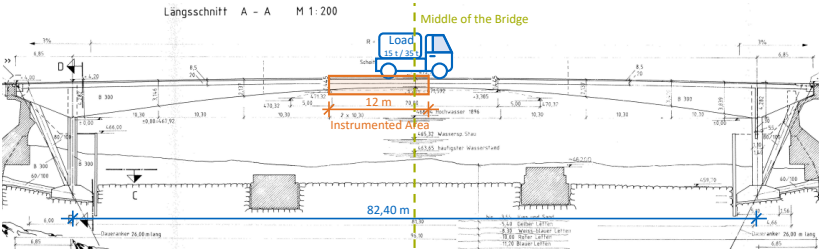

Figure 6.38: Overview of the instrumented bridge (adapted from [134]).

Due to its old age and a known problem with tendon corrosion, the structure is also monitored using different technologies. Müller et al. [134] gives an excellent overview of the bridge's history, status, and monitoring.

For the subsequent mounting of the ultrasound transducers described in Sec. 4.8, core drillings were performed that were filled with the transducers and afterward grouted with concrete. This creates similar conditions compared to the laboratory experiment of Sec. 6.2. Also, compared to gluing onto the surface, the installation has significantly better durability and signal transmission properties, which are essential for long-term monitoring.

The problem with the existing structure is a lack of information on the current state and reference measurements for the CWI results. After the instrumentation of the ultrasound transducers, test measurements were performed. The bridge was closed for this purpose and only loaded with a 15 t and a 35 t heavy truck in the middle of the bridge. Tab. 6.4 gives an overview of the loading process.

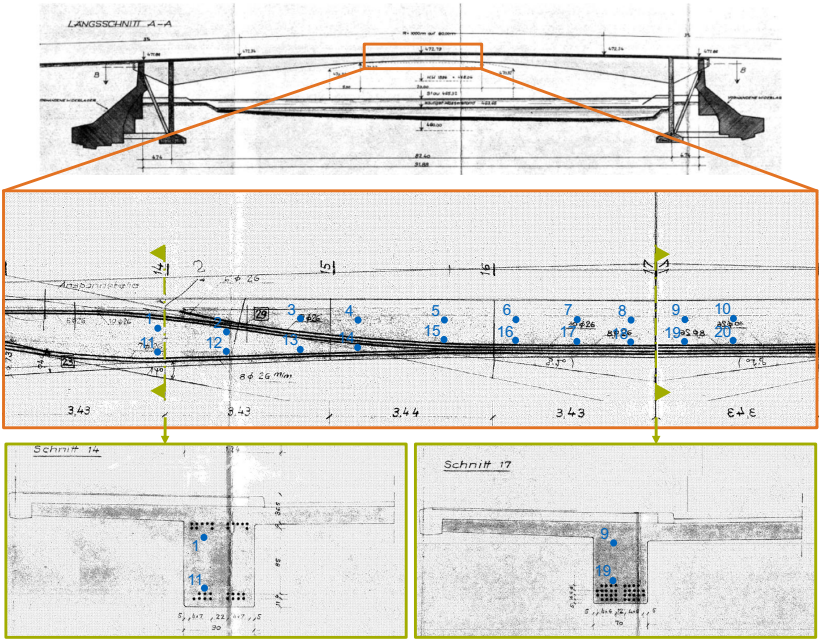

Figure 6.39: Overview of sensor placement (blue dots) and cross-section.

Loading process		
Load step	Loading	Position
1 (reference)	no load	-
2	15 t	middle of the bridge
3	no load	-
4	35 t	middle of the bridge
5	no load	-
6	15 t	middle of the bridge
7	no load	-

Table 6.4: Overview of the loading process at the real bridge.

Since the used central frequency is the same as the laboratory experiment of Sec. 6.2, the used simulation parameters are also as similar as possible. An overview is given in Tab. 6.5. One main difference from the laboratory experiment is using a fixed reference. For the evaluation of load steps 2-7, the measurements at load step 1 are used as the reference measurement.

Central frequency of Gaussian pulse	60 kHz
Amount of useable measurements	81
Range of source-receiver distances	0.41 m - 4.62 m
Simulation parameters for damage localization	
Intensity computation	FEM-based (Sec. 5.1.4) + Improvements of Sec. 5.1.5
Sensitivity modification	values for each measurement clipped to 1/6 of the maximum sensitivity
Average node distance of the mesh	0.15 m
Number of nodes	1746
Simulation time step	1×10^{-6} s
Diffusivity	$400 \frac{m^2}{s}$
Evaluated signal length (after tof)	2000 µs
Decorrelation window length T	400 µs
Reference measurement	fixed reference
Signal stretching window length T	250 µs
Solving algorithm	Trust Region Reflective Algorithm (Sec. 3.6.2)

Table 6.5: Overview of the simulation parameters for damage localization at the real bridge.

6.3.2 Numerical Model

As shown in Fig. 6.39, the instrumented girder has a T-cross section with a varying web height. The beam can thus be regarded as a complex geometry on which the advantages of the FE formulation can be utilized. Even though the FE formulation of the coda problem would allow a precise 3D modeling of the geometry, simplifications are applied to reduce the size of the model. The 3D geometry is reduced to a 2D plane obtained by a vertical cut through the center of the T-cross section. As the results of the laboratory experiment in Sec. 6.2 show, this is possible for a rectangular geometry. For the T-cross

section, the reduction also means the contributions of the flange are neglected. This is justifiable as the amount of wavefronts going from the web (source position) into the flanges and back to a receiver in the web is very small compared to wavefronts going only through the web. In the x-direction, the varying height of the web is modeled with a curved unstructured mesh. To respect a spread of energy away from the instrumented zone into the bridge, the 12 m long instrumented area is expanded by approximately 6 m in the x-direction on each side. The final model with a length of about 24 m and a height of 1.17 m - 1.84 m results after meshing with an average node distance of 0.15 m in a model with 1746 nodes. This is also the number of unknowns for the damage localization problem. The extension of 6 m on each side is performed to correctly model the instrumented area boundaries. To solve the inverse problem, reducing the model to the actual instrumented area could reduce the number of unknowns. However, this was not done in the end due to nearly no effect on the solution.

6.3.3 Usability of the Real Measurement Data

In order to evaluate the usability of measurement pairs, the overall CC of signals at load steps 3, 5, and 7 are evaluated and shown in Fig. 6.40. With load step 1 as the reference measurement, there is no change in the loading, and thus, all CCs should be close to 1, which means no changes in the signal. If there are significant correlation drops, the reproducibility of signals, which is a central underlying assumption, is not given, and thus signals can not be used. A lack of reproducibility of the signals is very often hardware-related and can not be improved or repaired afterward. A good reproducibility of the signals is assumed if the CC does not fall below 0.9. As shown in Fig. 6.40, several signals do not fulfill the CC threshold. Fig. 6.41 gives a graphical overview of the used measurement pairs (top) and the unusable and thus filtered ones (bottom). Most filtered measurement pairs have a long source-receiver distance or are connected to transducer 8 or 18. The longer the transmitting distance, the smaller the received amplitude, and thus, the signal-to-noise ratio increases. The maximum transmitting distance in this application with subsequently installed transducers is around 4 m. However, further investigations on the maximum transmitting distance for the coda signal in real structures are recommended for future research. A malfunctioning of selected transducers also occurred in the laboratory experiment. In total, 29 pairs out of 110 are filtered out due to bad reproducibility. When comparing the CC values with the ones from the experiment in controlled laboratory conditions (Sec. 6.2), one can see that challenges could arise in a practical application due to a generally worse reproducibility.

6.3.4 Evaluation for Different Loadings

Before evaluating the damage localization under load, load steps 3, 5, and 7 without loading are further investigated with a damage localization. Results are shown in Fig. 6.42. This should give a reference for the damage localizations under load and help distinguish if the detected damage is only localized

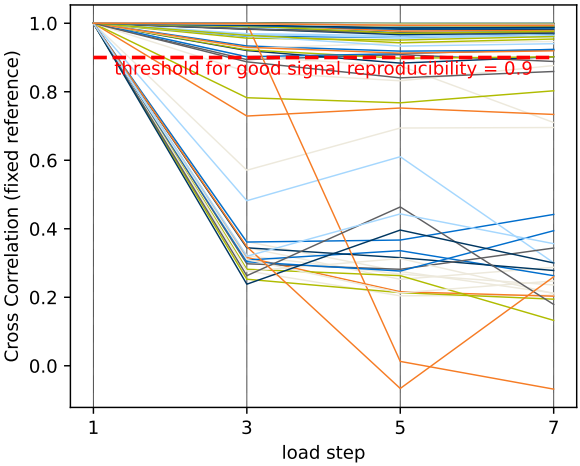

Figure 6.40: CC evaluation at the real bridge for no loading applied.

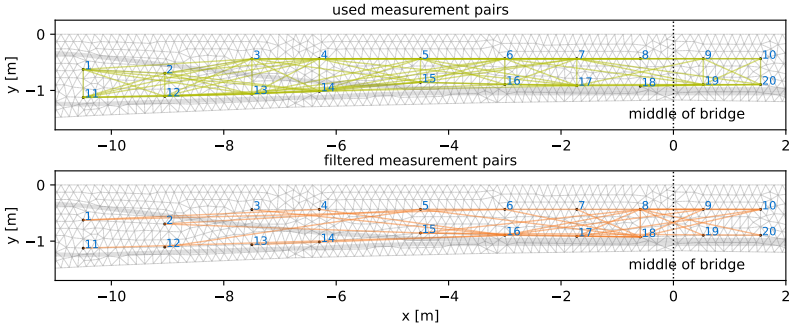

Figure 6.41: Overview of the used measurement pairs. Green pairs are used, and orange ones are filtered out. Thick, light grey lines indicate the position of tendons, and the mesh represents a 2D slice of the bridge geometry.

under load or also without loading. One can see that the resulting damage localization looks very similar for all load steps without loading applied. Also, the change of the reference measurement, as shown in the bottom of Fig. 6.42, has no influence. This is good as it indicates that the choice of the used reference seems to have no big influence, and the detected damage areas most likely come from comparably bad signal reproducibility in that area. As

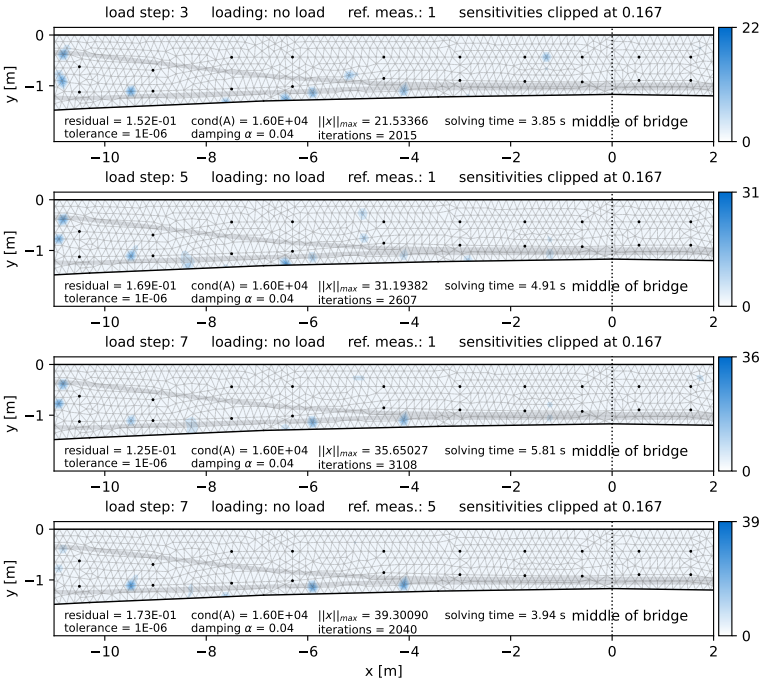

Figure 6.42: Damage localization at the real bridge for load steps without loading applied.

shown in Fig. 6.40, the reproducibility of signals surpassing the threshold of 0.9 still differs. With the zero state evaluation and the knowledge of areas where localized damage might come from bad signals, the damage localization under load is performed. Fig. 6.43 shows the results for increasing loading. Note that the actual loading process of Tab. 6.4 is different from the order of the visualization (where loading increases from top to bottom) but due to the use of a fixed reference has no effects.

The damage localization for the different load steps looks very similar. This reproducibility is an excellent sign and increases the significance of the results. Even though the values of the solutions space have no expressiveness on their own, as discussed in Sec. 5.2.4, a comparison of the values for the different load intensities makes sense. The maximum value of the solution space $||x||_{max}$ increases with increasing loading, which makes sense as the cracks open up with the increased load, and the damage to be detected increases. Under loading, multiple damaged regions are detected. The most important ones are at the bottom near x = -3.0 m, x = -1.2 m, x = 0.0 m and x = +2.0 m (orange circled). Another one is near x = +1.0 m that is detected under 15 t loading

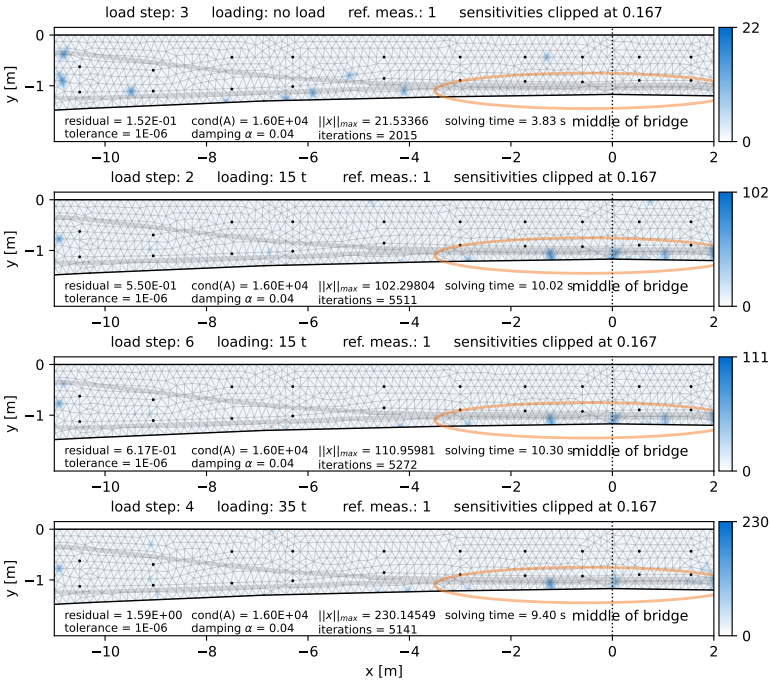

Figure 6.43: Damage localization at the real bridge for increasing loading.

but not under 35 t loading. The other damage localizations at x < -4.0 m show strong similarities to the damage localization with no loading and are thus more likely signal reproducibility related, as discussed before, rather than coming from the actual damage. Due to the relative measurement evaluation, only new damage can be detected. Putting all load steps shown in Fig. 6.42 and Fig. 6.43 in the actual order of Tab. 6.4 underlines the assumption that there are existing cracks that open up under load and close without loading. This phenomenon should be further investigated in laboratory experiments but can be very powerful for detecting existing damage. Note that the closure of cracks with resulting invisibility for the CWI most likely comes from the prestressing. It can also be seen that the detected damage area is directly under the applied forces. For the given structure, the bending moment and, consequently, the stresses originating from the external load are maximum around the position of the load application. This explains why only cracks open up near the position of the load application. Another investigation of the structure on site is advised, but due to the inaccessibility of the affected area, it was not possible so far.

Overall, the results of the CWI damage localization are promising. However,

measuring a complete set of signals for each load step takes several minutes. This duration makes an application under varying traffic loads very difficult. Nevertheless, the given design of the experiment with controlled loading is a practically applicable use case of CWI as non-destructive testing as cracks in a prestressed structure that open up under loading seem to be detectable. It should also be mentioned that since existing damage is hard to detect, the structure can always be in a worse condition than the CWI results suggest. Further research should try to find solutions for an application under varying traffic loads.

6.3.5 Influence of the Number of Measurement Pairs Used

Due to the long time it takes to measure a complete set of signals, the influence of the density of the measurement network is investigated. For this purpose, the evaluation from Fig. 6.43 is repeated with only measurement pairs of neighboring sensors (that fulfill the CC threshold) active. Fig. 6.44 shows the resulting damage localization. Note that compared to Sec. 6.2.5.3, where a

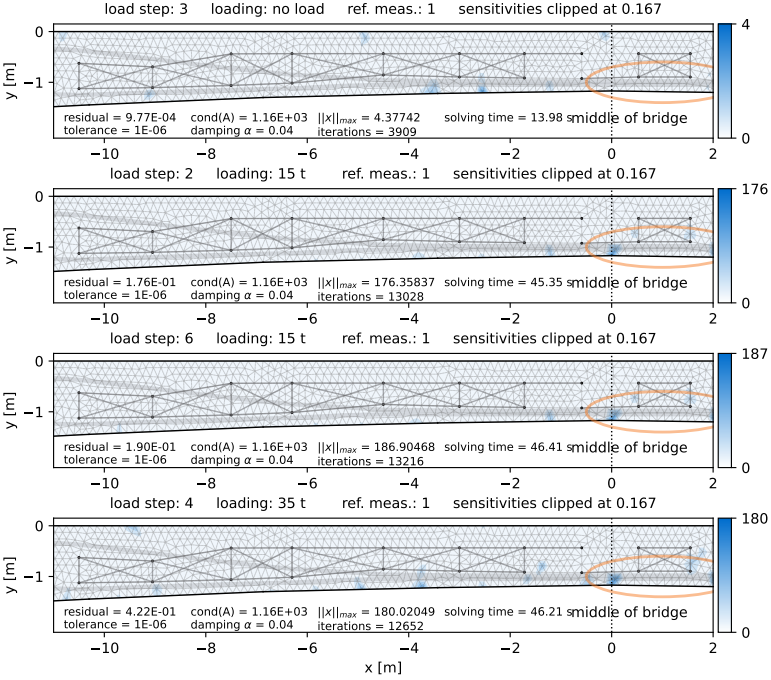

Figure 6.44: Damage localization at the real bridge for increasing loading with only selected pairs active.

similar study was performed, the distances to neighboring sensors are in the range of the study for pairs to not neighboring sensors in Sec. 6.2.5.3 that gave slightly better results.

Compared to the complete measurement network of Fig. 6.43, the result is overall similar to the detected damage near the middle of the bridge. However, mainly results with no load and with 35 t applied are a bit different. There is no longer a magnitude change between 15 t and 35 t. Also, several localizations at 35 t were not seen before. A parameter with strong influence is the clipping threshold for the sensitivities. All previous damage localizations had a very dense measurement pair network. The threshold at 1/6 might be too low for the very sparse measurement pair network. Therefore, the clipping factor is increased to 1/2, and results are shown in Fig. 6.45.

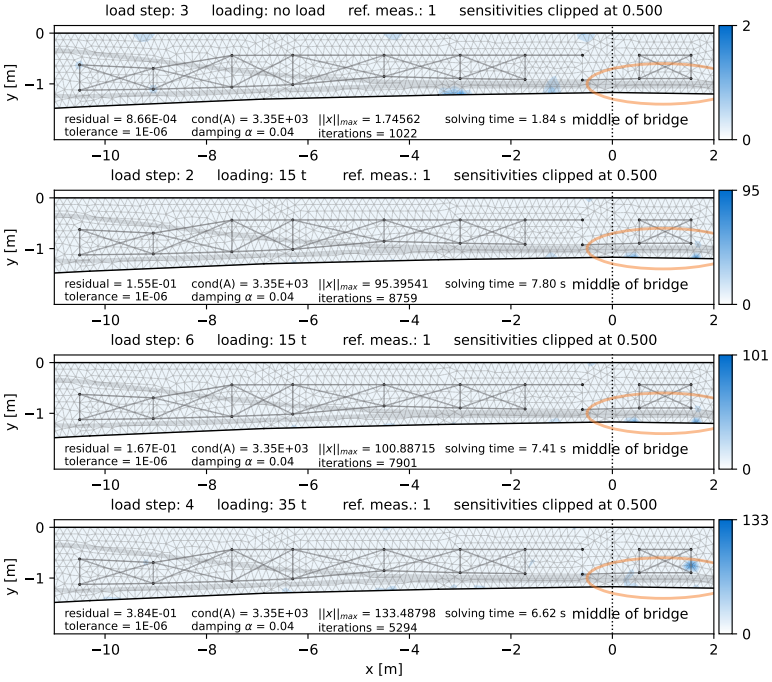

Figure 6.45: Damage localization at the real bridge for increasing loading with only selected pairs active and sensitivities clipped at 1/2.

With the higher threshold, the solution under a load of 35 t improves with fewer localizations that were not seen before and larger values for the located damage compared to the 15 t load state. With 15 t applied in the middle of the bridge, the detected damage locations are again reproducible and strongly

correlate to the results, with the whole measurement network being active. Only the detection of Fig. 6.43 at the bottom near x = -3.0 m is not visible.

Overall, the damage localization gives good results, with only measurement pairs of neighboring sensors being active. The threshold on the sensitivities can be understood as a filter that should be adjusted correctly, and it helps to increase the threshold for coarser measurement pair networks. The more pairs sense an area, the more robust the results are. It could thus be a use case to permanently measure with a selected number of pairs and perform further inspections with a complete measurement network in case of significant changes compared to a defined reference.

6.4 Conclusion on Damage Localization with Coda Waves

This chapter has further developed several aspects of damage localization with CWI. The numerical investigations with multiple parameter studies were used to develop the FEM based imaging. Compared to the established analytic solution-based imaging [20–22], this is an improvement as FEM allows to solve the problem in complex geometries. The analytic solution-based imaging typically uses the RTE that contains next to a part describing the diffusive spread and also one that represents the ballistic wave. In this thesis, the improvements of the analytic RTE are applied to the FEM solution in order to further improve it. The developments were then tested in a laboratory experiment. The major challenge here was successfully applying the previously at higher frequencies (> 100 kHz) used methods to the comparatively low 60 kHz.

One problem that can also be found in experimental results from literature [124, 125] is the strong correlation of the obtained solution with the transducer network. The assumed reason in this thesis is the spatial sensitivity distribution that forms sharp peaks at the transducer positions but, in the time domain, has a convex development that is in shape similar to regions further away from the transducer. Because of this behavior, the applied least-squares fitting needed to solve the inverse problem tends to identify transducers as damaged locations. The dependency on transducer locations is reduced in this thesis by limiting the sensitivities in transducer regions to a fraction of the maximum. By doing so, the obtained results and the robustness to implausible measurements are improved. Justifiable is this approach with the size of the ultrasonic transmitters, numerical singularities of point sources, and the known lack of the model in areas close to the transducer. Ultimately, this modification also allows us to apply the multiple scattering-based imaging techniques to the signals from a 60 kHz impulse.

The laboratory investigations underline the immense sensitivity of coda waves. Even with a loading half the one where the concrete's tensile strength is reached and computational cracking occurs, little changes are detectable and correctly located. When macrocracking occurs, one can see in the measurement data that the imaging is sensitive to cracks occurring very close to transducers. Another difficulty is the narrow space in which many cracks

occur simultaneously. Therefore, it is impossible to correctly identify all cracks individually, but a rough localization of the damaged area is relatively robust. This is also the case after the cracks appear and only open further under increasing load. The thesis also derived a method of fitting the diffusion solution to the ultrasound signals to obtain the material's diffusivity for a frequency of 60 kHz. The results show a large variance and, for short source-receiver distances, a strong correlation to the tof. The problem is most likely related to a travel distance less than the transport mean free path and could be addressed in further research by respecting this implausibility in the solution algorithm in the covariance matrix of the measurement data. In the experiment, the influence of different amounts of measurement pairs was investigated. Due to the limited size of the test specimen, a conclusion is difficult. Ultimately, the best results are achieved with the maximum number of measurement pairs, but localization is also possible with fewer. This finding has the potential for optimizing sensor positions in further research. An open problem of the imaging with CWI is the classification of localized damages. With a stepwise load increase and a gradient analysis of the obtained solution values, the thesis shows a possible indicator for irreversible damage. A novelty is using phase shifts evaluated within the coda signal as measurements instead of DC for the inverse problem. The good identification of stress, tension and damage zones is an excellent result that is very promising for further research.

Applying damage detection with CWI in a field experiment at the Gänstorbrücke showed promising results. Due to the complex, non-cubic geometry with a varying cross-section, it is essential to be able to model the problem with FEM. One restriction, however, is that the experiments miss a crack mapping or reference measurements as validation for the CWI. However, the data was checked for consistency and plausibility in the best possible way. Results suggest that even existing damage could be detectable if the cracks close without loading due to pre-tensioning.

The three conducted experiments underline the benefits and immense potential of CWI. The technology's most significant advantages are its large-scale coverage of the monitored structure and its immense sensitivity. However, this sensitivity to various environmental influences is also the biggest challenge in long-term SHM applications. In a controlled setting, most of the influences are, however, controllable such that CWI can be applied as supporting NDT method for enhanced investigations on a structure.

Chapter 7

Model Updating in Structural Analysis

Computational model updating aims to identify input parameters of a numerical model such that computation results match measurements in the best way possible. This chapter uses local sensitivities that describe the relation of adaptable input parameters and measurable output parameters by derivatives. With the sensitivities appearing in the inverse problem, the problem is an application of gradient-based optimization. This system identification application is mathematically similar to the previously presented imaging techniques with coda waves (cf. Sec. 5.2.2). A specialty of the coda problem is that sensitivities are not determined by derivatives of a problem but with a model based on random paths (cf. Sec. 5.2.1). This chapter uses a structural-mechanical model to show how sensitivities can be calculated by deriving an initial problem. Due to the relation of real quantities to a numerical model that allows calibration, the method is a crucial aspect of DT development. In contrast to the coda problem, the application in structural analysis has the advantage that measurements, e.g., displacements, can be directly linked to the structure's stiffness. This allows localization of structural changes, as well as a quantification of the stiffness change.

7.1 Introduction to Model Updating in Structural Analysis

The basis for model updating in structural mechanics is the analysis of structural behavior. The most popular method to numerically solve structural-mechanical problems is the finite element method (FEM). In principle, the same procedure as in Sec. 5.1.4 is applied. For this reason, references are only

made here to literature that deals extensively with the subject. Standard works for FEM are among others Ottosen et al. [117], Zienkiewicz et al. [118], Hughes [135], and Bathe [136].

In structural analysis, the FEM master stiffness equation relates forces $\mathbf{f}$ to stiffnesses $\mathbf{K}$ and displacements $\mathbf{u}$:

$$\mathbf{K}\mathbf{u} = \mathbf{f} \tag{7.1}$$

The contribution of each element to the master stiffness equation of Eq. 7.1 is computed with the same elemental formulations as in the diffusion problem (cf. Eq. 5.9). Eq. 7.1 and Eq. 5.8 are, in fact, the same for a static case (time derivative vanishes) if $\mathbf{I}$ is replaced by $\mathbf{u}$.

It should be noted that numerical methods are models that can only represent reality partially due to idealization, discretization, solution errors, and erroneous assumptions. In the FEM workflow, they appear as shown in Fig. 7.1.

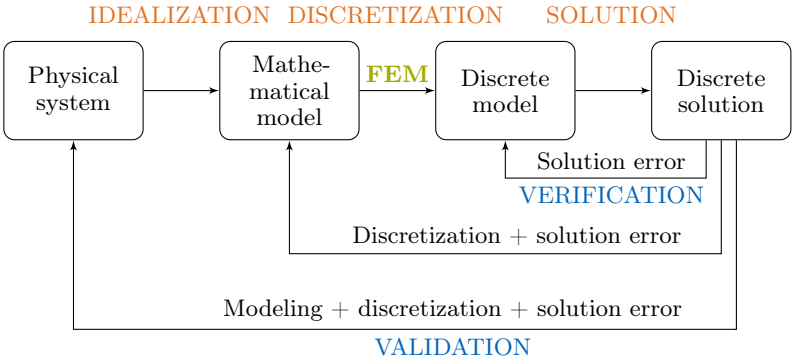

Figure 7.1: Role of FEM in the structural analysis process (adapted from [137]).

An overview of the different errors is given below. The list is not claimed to be exhaustive, and further examples of the errors can be found in Mottershead et al. [138].

1. Idealization errors result from assumptions made to characterize the mechanical behavior of the physical structure [138].

- simplifications of the structure, e.g., a plate is treated like a beam
- FE formulation neglects particular properties, e.g., the influence of transverse shear deformation
- erroneous modeling of boundary conditions, e.g., elastic support is assumed rigid
- non-linear structural behavior assumed linearly

2. Discretization errors results from reducing the mathematical model to a discrete model with a finite number of degrees of freedom [137].

- finite element mesh is too coarse

3. Solution errors due to numerical limitations.

- implementation errors
- limited numerical precision
- choice of the wrong or inefficient solution algorithm

4. Erroneous assumptions for model parameters [138].

- material parameters such as Young's modulus
- cross-section properties of a beam
- erroneous assumptions for the external loads

When computing real structural responses, the aim is to minimize all the listed errors in the FEM workflow. Models that fulfill these requirements shall be called validated models [138].

Computational model updating aims to adapt a set of input parameters of a numerical model such that the computations yield the same results as given measurements. This framework is similar to the DT concept, whereby due to the unidirectional relationship, it is, according to Kritzinger et al. [42], a digital shadow. In the context of model updating, it is also essential to include a **measurement error** as a source of error. In numerical benchmarks that compare with analytical solutions, this error does not appear. Nevertheless, when working with real measurements, the influence of quality and accuracy of measurements is enormous and should always be considered when evaluating results.

7.2 Sensitivity Analysis in Structural Analysis

Model updating aims to adapt input parameters such that the output parameters of a model are matched with measurements. Investigating the relationship between input and output parameters is the classical application of sensitivity analysis. Local sensitivities are gradient information that can be determined using derivatives. A simple way to numerically compute sensitivities is using finite differences (FD) where input parameters are varied with a finite step, and changes in the output are investigated. It is numerically inefficient because FD needs to solve the problem for each input-output relation. More advanced methods are the direct and adjoint sensitivity analysis, which are numerically efficient in investigating the relation of one input parameter to numerous output parameters or numerous input parameters to one output parameter. Input parameters in the structural analysis are, e.g., cross-section properties and Young's moduli that can differ for each element, but also node positions, loads, etc., are input. Output parameters are, e.g., displacements,

stresses, and strains. In case the model updating should be able to modify all elements, so numerous input parameters, the adjoint sensitivity analysis is a numerically efficient choice.

7.2.1 Adjoint Sensitivity Analysis

The explanations below are based on the excellent work of Fußeder [139] in this field. Input parameters are referred to with $\mathbf{x}$ in this thesis, and the solution of the master stiffness equation, which is also referred to as the primal problem, are the state variables $\mathbf{u}$. In order to be able to deal with various kinds of output parameters, not only the state variables $\mathbf{u}$, the general response function y is introduced. It can stand for displacements and other output parameters, e.g., stresses.

$$y(\mathbf{x}, \mathbf{u}(\mathbf{x})) \tag{7.2}$$

The total derivative with respect to an input parameter $x_i \in \mathbf{x}$ of this general response description that can depend on $\mathbf{x}$ as well as $\mathbf{u}$, which itself depends on x_i, then looks as follows:

$$\frac{dy}{dx_i} = \frac{\partial y}{\partial x_i} + \left[\frac{\partial y}{\partial \mathbf{u}}\right]^T \cdot \frac{d\mathbf{u}}{dx_i} \tag{7.3}$$

In order to obtain the total derivative of $\mathbf{u}$ with respect to x_i, the primal problem is derived with respect to x_i. Therefore, the equilibrium of Eq. 7.1 is rewritten as a residual formulation

$$\mathbf{r}(\mathbf{x}, \mathbf{u}) = \mathbf{K}(\mathbf{x})\mathbf{u} - \mathbf{f}(\mathbf{x}) = \mathbf{0} \tag{7.4}$$

and derived with respect to x_i:

$$\frac{d\mathbf{r}}{dx_i} = \frac{\partial \mathbf{r}}{\partial x_i} + \frac{\partial \mathbf{r}}{\partial \mathbf{u}} \cdot \frac{d\mathbf{u}}{dx_i} = \mathbf{0} \tag{7.5}$$

Eq. 7.5 can be solved for $\frac{d\mathbf{u}}{dx_i}$

$$\frac{d\mathbf{u}}{dx_i} = \left[\frac{\partial \mathbf{r}}{\partial \mathbf{u}}\right]^{-1} \cdot \left[-\frac{\partial \mathbf{r}}{\partial x_i}\right] \tag{7.6}$$

and inserted into Eq. 7.3:

$$\frac{dy}{dx_i} = \frac{\partial y}{\partial x_i} + \left[\frac{\partial y}{\partial \mathbf{u}}\right]^T \cdot \left[\frac{\partial \mathbf{r}}{\partial \mathbf{u}}\right]^{-1} \cdot \left[-\frac{\partial \mathbf{r}}{\partial x_i}\right] \tag{7.7}$$

With the partial derivatives of Eq. 7.4 inserted, the expression to evaluate the sensitivity of a response y to a change of an input parameter x_i is obtained:

$$\frac{dy}{dx_i} = \frac{\partial y}{\partial x_i} + \left[\frac{\partial y}{\partial \mathbf{u}}\right]^T \cdot \mathbf{K}^{-1} \cdot \left[\frac{\partial \mathbf{f}}{\partial x_i} - \frac{\partial \mathbf{K}}{\partial x_i}\mathbf{u}\right] \tag{7.8}$$

The partial derivative of y with respect to x_i is generally computationally cheap. The expensive part is the second summand. A specialty is that the term on the left of the inverse stiffness matrix ($\frac{\partial y}{\partial \mathbf{u}}$) is independent of the input parameters x_i and the one on the right ($[\frac{\partial \mathbf{f}}{\partial x_i} - \frac{\partial \mathbf{K}}{\partial x_i}\mathbf{u}$) is independent of the selected response function y. In terms of computational effort, it thus makes a difference in which direction Eq. 7.8 is evaluated as it is possible to separate input parameters from responses. If the analysis is started with an evaluation of $\mathbf{K}^{-1} \cdot [\frac{\partial \mathbf{f}}{\partial x_i} - \frac{\partial \mathbf{K}}{\partial x_i}\mathbf{u}]$ which is the state derivative $\frac{d\mathbf{u}}{dx_i}$, the evaluation is known as direct sensitivity analysis. The state derivative

$$\frac{d\mathbf{u}}{dx_i} = \mathbf{K}^{-1} \cdot \underbrace{\left[\frac{\partial \mathbf{f}}{\partial x_i} - \frac{\partial \mathbf{K}}{\partial x_i}\mathbf{u}\right]}_{\mathbf{f}^*} \tag{7.9}$$

thereby has similarities to the solution of the master stiffness equation $\mathbf{u} = \mathbf{K}^{-1}\mathbf{f}$ and the partial derivative of $-\mathbf{r}$ with respect to x_i is thus denoted as pseudo-load $\mathbf{f}^*$. The pseudo-load only depends on input parameters and is independent of the response. The second analysis step evaluates Eq. 7.3. Since the partial derivative of y with respect to $\mathbf{u}$ can be determined with less effort, it is computationally cheap to evaluate the influence of one input parameter on numerous responses y.

If it is, however, of interest to evaluate the influence of many input parameters, the expensive matrix-vector multiplication should be carried out from right to left. The necessary computation order change is achieved by transposing Eq. 7.8:

$$\frac{dy}{dx_i}^T = \frac{\partial y}{\partial x_i}^T + \left[\frac{\partial \mathbf{f}}{\partial x_i} - \frac{\partial \mathbf{K}}{\partial x_i}\mathbf{u}\right]^T \cdot \underbrace{\mathbf{K}^{-T} \cdot \left[\frac{\partial y}{\partial \mathbf{u}}\right]}_{\boldsymbol{\lambda}} \tag{7.10}$$

The version of Eq. 7.10 is called adjoint sensitivity analysis. Analogous to the direct sensitivity analysis, where the first computation step is summarized in the state derivative $\frac{d\mathbf{u}}{dx_i}$, a special variable is introduced for the adjoint sensitivity analysis: the adjoint displacement $\boldsymbol{\lambda}$. Taking into account that $\frac{dy}{dx_i}$ and $\frac{\partial y}{\partial x_i}$ are scalars and $\mathbf{K}$ is symmetric, the adjoint sensitivity analysis can be rewritten as follows:

$$\frac{dy}{dx_i} = \frac{\partial y}{\partial x_i} + \mathbf{f}^{*T} \cdot \boldsymbol{\lambda} \qquad \text{with} \quad \begin{array}{ll} \text{pseudo-load} & \mathbf{f}^* = \left[\frac{\partial \mathbf{f}}{\partial x_i} - \frac{\partial \mathbf{K}}{\partial x_i}\mathbf{u}\right] \\ \text{adjoint problem} & \boldsymbol{\lambda} = \mathbf{K}^{-1} \cdot \left[\frac{\partial y}{\partial \mathbf{u}}\right] \end{array} \tag{7.11}$$

In Eq. 7.11, the computation of $\boldsymbol{\lambda}$ is the most expensive. Due to the similarity to the solution of the master stiffness equation $\mathbf{u} = \mathbf{K}^{-1}\mathbf{f}$, the partial derivative of response y with respect to the state variables $\mathbf{u}$ is also referred to as adjoint-load. After the adjoint problem is solved, the final evaluation can thus be regarded as a computationally cheap post-processing step. Thus, the adjoint sensitivity analysis is suitable for evaluating the influence of numerous input parameters on a fixed response.

7.2.2 Computational Aspects

The focus of this thesis is on the adjoint sensitivity analysis. It is the basis for the computational model updating below, where all input parameters can, in theory, be adjusted to update the model and, therefore, must be evaluated with adjoint sensitivity analysis. Fußeder [139] mentions aspects regarding the computational effort and an efficient implementation. The computational effort can be reduced due to the sparsity of the pseudo-load. As typical input parameters x_i dealt with in this thesis are element values such as cross-section parameters and Young's modulus, the partial derivative of $\mathbf{f}$ with respect to x_i is zero, and only stiffness entries in the master stiffness matrix $\mathbf{K}$ directly depending on x_i are non-zero values. Therefore, instead of evaluating the whole master stiffness matrix, $\frac{dy}{dx_i}$ can be evaluated by adding the n elemental contributions (^{e}) that are non-zero after the adjoint problem is solved.

$$\frac{dy}{dx_i} = \frac{\partial y}{\partial x_i} + \sum_n \left\{ \left[\frac{\partial \mathbf{f}^e}{\partial x_i} - \frac{\partial \mathbf{K}^e}{\partial x_i} \mathbf{u}^e \right]^T \cdot \boldsymbol{\lambda}^e \right\} \tag{7.12}$$

For evaluating the effect of the Young's modulus E_i of the i-th element on a displacement u_j, Eq. 7.12 simplifies to the following:

$$\frac{du_j}{dE_i} = - \left[\frac{\partial \mathbf{K}^i}{\partial E_i} \mathbf{u}^i \right]^T \cdot \boldsymbol{\lambda}^i \tag{7.13}$$

For evaluating the pseudo-load $\mathbf{f}^*$, one needs to implement the partial derivatives of $\mathbf{K}$ and $\mathbf{f}$ for all input parameters of interest. As these are various, Bletzinger et al. [140] and Gengdong et al. [141] use a semi-analytic sensitivity analysis with FD to evaluate the elements' partial derivative to remain flexible to various input parameters. Masching [142] shows that the semi-analytic approach is even faster.

7.2.3 Graphical Interpretations

In his work, Fußeder [139] shows the close connection of adjoint sensitivity analysis to influence functions. The classic application of influence functions in engineering is the fast, graphical evaluation of the influence of different loading scenarios on a fixed system response. The similarity to adjoint sensitivity analysis is obvious. In his work, Fußeder [139] introduces generalized influence functions that can be used to evaluate arbitrary relations of input parameters and system responses. A complete explanation is out of the scope of this thesis, and the reader is referred to Fußeder [139] and Fußeder et al. [143, 144] for exhaustive explanations. Here, only a graphical example points out the visible relation of the sensitivities dealt with in this chapter and the ones of the coda waves in Sec. 5.2.1.

With the method of generalized influence functions, the spatial relationship between stiffnesses and deformations can be calculated by pointwise multiplication of two functions. This is shown for a beam under line-load p (Fig. 7.2) and single load F (Fig. 7.3) in the figures below.

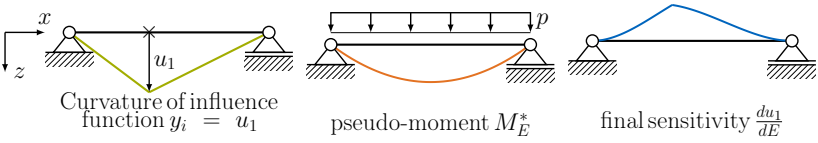

Figure 7.2: Graphical sensitivity analysis for effect of Young's modulus E on displacement u_1 of a beam under line-load p.

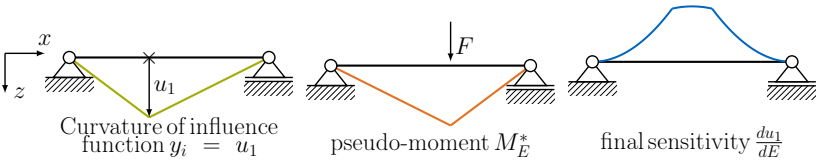

Figure 7.3: Graphical sensitivity analysis for effect of Young's modulus E on displacement u_1 of a beam under single load F.

On the left, the curvature $\kappa_\lambda = -\lambda''$ of the influence function λ for a system response y, here node displacement u_1, is shown. Influence functions of displacements are the system deformation under a unit load equivalent to the evaluated displacement. The curvature is closely related to the moment course with $M = -EI\kappa_\lambda$. Thus, the curvature of the influence function can also be derived from the moment course under the unit load. The second function related to the evaluated input parameter is shown in the middle. For the example of Young's modulus as input parameter, the moment under the given load is of interest and referred to as pseudo-moment M_E^*. The pointwise multiplication of the influence function and pseudo-moment leads to the final sensitivity $\frac{du_1}{dE}$ shown on the right. For the case of discrete finite elements, the continuous curves are only approximated. With an integration over the element length, discrete values per element are obtained and shown in Fig. 7.4 for a beam discretized with ten elements.

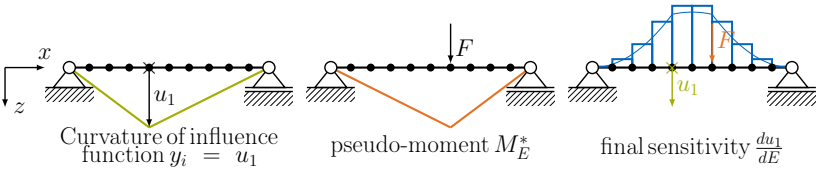

Figure 7.4: Graphical sensitivity analysis for effect of Young's modulus E on displacement u_1 of a beam under single load F with discrete finite elements.

The graphical procedure is similar to the visualization of the coda sensitivity computation in Fig. 5.7. Common in both sensitivity computations is

that input and response are separated. For coda sensitivities, this is the independence of source and receiver in the sensitivity kernels numerator (Eq. 5.19). A visible difference is, however, that coda sensitivities have, unlike the static loading in the structural analysis example, a time component such that all possible time combinations are added up in the integral of the sensitivity kernel (Eq. 5.19).

7.3 Computational Model Updating

Computational model updating aims to calibrate a numerical model such that computed values agree with real measurements. Recommendable works in this field with practical applications are, among others, the ones by Link [61, 68], Mottershead et al. [138], Stöhr [145], and Friswell [146].

Mathematically, the goal of computational model updating is to minimize a function $f(\mathbf{x})$ that describes the difference of measured responses $\tilde{\mathbf{y}}$, that are quantities from the real space and thus independent of numerical input parameters $\mathbf{x}$ and estimated responses $\mathbf{y}$, which in this case are the responses of the FE model.

$$\min_{\mathbf{x}\in\mathbb{R}^n} f(\mathbf{x}) \qquad \text{with } f(\mathbf{x}) = \tilde{\mathbf{y}} - \mathbf{y}(\mathbf{x}) \tag{7.14}$$

The problem that input parameters $\mathbf{x}$ need to be adapted such that the system's responses that can also be measured are matched is a classical inverse problem. When applying the Gauss-Newton algorithm of Ch. 3 on the inverse problem, Eq. 7.14 is formulated as least-squares problem that contains the RSS of estimated and measured values:

$$\min_{\mathbf{x}\in\mathbb{R}^n} \|\tilde{\mathbf{y}} - \mathbf{y}(\mathbf{x})\|_2^2 \tag{7.15}$$

The estimated responses $\mathbf{y}$ are approximated with a linearization by a Taylor series expansion that is truncated after the linear term:

$$\mathbf{y}(\mathbf{x}) \approx \mathbf{y}(\mathbf{x}_k) + \mathbf{A}_{\mathbf{x}_k} \cdot (\mathbf{x}_{k+1} - \mathbf{x}_k) \tag{7.16}$$

$\mathbf{y}(\mathbf{x}_k)$ thereby describes the responses of the initial (or previous) model with $\mathbf{x}_k$ as input parameters. The entries of $\mathbf{A}$ depend on the point of linearization given by $\mathbf{x}_k$, which is indicated by the notation with $\mathbf{x}_k$ as subscript. When inserting Eq. 7.16 into Eq. 7.15, one obtains the objective function for computational model updating:

$$\min_{\mathbf{x}\in\mathbb{R}^n} \|\tilde{\mathbf{y}} - \underbrace{\mathbf{y}(\mathbf{x}_k) + \mathbf{A}_{\mathbf{x}_k} \cdot (\mathbf{x}_k - \mathbf{x}_{k+1})}_{\mathbf{y}(\mathbf{x})} \|_2^2 \tag{7.17}$$

Eq. 7.17 is similar to Eq. 3.20. Applying the equations introduced in Sec. 3.5, the solution of one iteration step can thus be obtained with:

$$\mathbf{x}_{k+1} = \mathbf{x}_k + \underbrace{(\mathbf{A}_{x_k}^T \mathbf{A}_{x_k})^{-1} \mathbf{A}_{x_k}^T \overbrace{(\tilde{\mathbf{y}} - \mathbf{y}(\mathbf{x}_k))}^{\Delta \mathbf{y}_k}}_{\Delta \mathbf{x}_k} \tag{7.18}$$

In the solution of the Gauss-Newton iteration step in Eq. 7.18, the problem that solves for the incremental update $\Delta\mathbf{x}_k$ is a linear one that can be written as follows:

$$\underbrace{\mathbf{A}_{\mathbf{x}_k}}_{\frac{d\mathbf{y}}{d\mathbf{x}}} \cdot \Delta\mathbf{x}_k = \Delta\mathbf{y}_k \qquad \begin{aligned} &\text{with} \quad \Delta\mathbf{x}_k = \mathbf{x}_{k+1} - \mathbf{x}_k \\ &\text{and} \quad \Delta\mathbf{y}_k = \tilde{\mathbf{y}} - \mathbf{y}(\mathbf{x}_k) \end{aligned} \tag{7.19}$$

The problem of Eq. 7.19 is visualized in Fig. 7.5. In the figure, the indices of $\mathbf{A}$ refer to the position in the matrix (and not the point of linearization). It is noticeable that the problem is very similar to that of imaging with coda waves (cf. Fig. 5.9, Eq. 5.20).

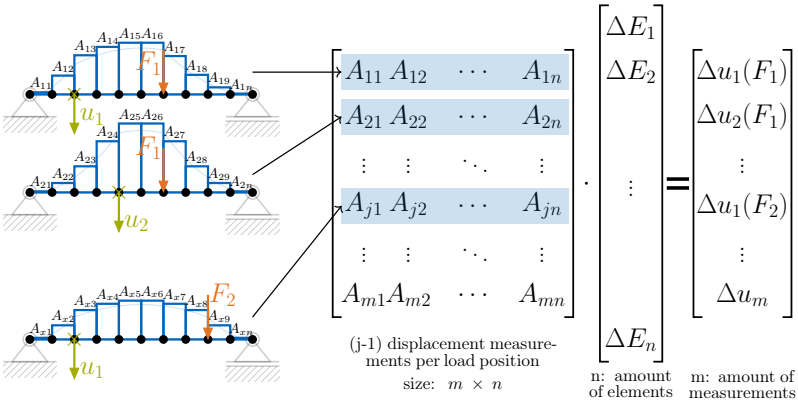

Figure 7.5: Linearized relation of input parameters $\mathbf{x}$ (here elemental Young's modulus E_i) and system responses $\mathbf{y}$ (here nodal displacements u_j) that is described in Eq. 7.19 visualized.

In each iteration step, $\mathbf{x}$ is updated, and therefore, a recomputation of all sensitivities in $\mathbf{A}$ is required. However, when assuming little changes of $\mathbf{x}$, the non-linearity of the least-squares optimization problem in Eq. 7.15 is typically significantly larger than the non-linearity of the structural behavior. In order to reduce computational effort, one could solve the problem for $\mathbf{x}$ with fixed sensitivities until convergence, update $\mathbf{A}$, and repeat the complete procedure until convergence.

The problem of Eq. 7.17 is ill-posed. It is thus required to regularize the problem, e.g., with the Tikhonov regularization presented in Sec. 3.3. Therefore, the inverse covariance matrix of the input parameters $\mathbf{C}_X^{-1}$ and the inverse covariance matrix of the measurements $\mathbf{C}_Y^{-1}$ are included and the incremental update for an iteration step $\Delta\mathbf{x}_k$ computes as follows (cf. Eq 3.27):

$$\Delta\mathbf{x}_k = (\mathbf{A}_{\mathbf{x}_k}^T \mathbf{C}_Y^{-1} \mathbf{A}_{\mathbf{x}_k} + \mathbf{C}_X^{-1})^{-1} \mathbf{A}_{\mathbf{x}_k}^T \mathbf{C}_Y^{-1} (\tilde{\mathbf{y}} - \mathbf{y}(\mathbf{x}_k) \tag{7.20}$$

This formulation is also used by Link [68] and Mottershead et al. [138]. For $\mathbf{C}_X^{-1}$, that represents the uncertainty in the initial parameter estimation [63, 147, 148], the authors do not use the damping of the Tikhonov regularization where $\mathbf{C}_X^{-1} = \alpha^2\mathbf{I}$ but the following:

$$\mathbf{C}_X^{-1} = \alpha^2\mathbf{W}_X \qquad \text{with } \mathbf{W}_X = \frac{\text{mean}(\mathbf{\Gamma})}{\text{mean}(\mathbf{\Gamma}^{-1})}\mathbf{\Gamma}^{-1} \text{ and } \mathbf{\Gamma} = \text{diag}(\mathbf{A}_{\mathbf{x}_k}^T\mathbf{C}_Y^{-1}\mathbf{A}_{\mathbf{x}_k}) \tag{7.21}$$

The weighting matrix $\mathbf{W}_X$ allows the parameter changes to be constrained according to their sensitivity [138]. As the matrix $\mathbf{\Gamma}$, which contains sensitivity information, is inverted, large sensitivities in $\mathbf{A}_{\mathbf{x}_k}^T\mathbf{C}_Y^{-1}\mathbf{A}_{\mathbf{x}_k}$ are damped with only a small value. In contrast, small sensitivities are damped with large entries in $\mathbf{W}_X$. Consequently, the parameters x_i remain unchanged if their sensitivity approaches zero [68]. The scalar α is obtained with the L-curve method of Sec. 3.4.

In the computations for imaging with coda waves, the relation of system responses that are contained in the inverse covariance matrix of the measurements $\mathbf{C}_Y^{-1}$ is neglected by choosing $\mathbf{C}_Y^{-1} = \mathbf{I}$. The choice of the identity matrix is called the Markov estimator and yields the best linear unbiased estimate [68]. If measurements of different types are used in the computational model updating, values are likely of different magnitude. In such cases, it is advantageous to normalize the measurements as follows [138]:

$$\mathbf{C}_Y^{-1} = \text{diag}(\mathbf{y})^{-2} \tag{7.22}$$

The computational model updating can be applied at various times in the life cycle of a structure. On the one hand, it is possible to initially calibrate a numerical model so that reality is represented in the best way possible. After calibration, the model is validated and can be used to predict different scenarios. If further changes happen in reality, the computational model updating allows localization and quantification of those changes. Knowledge about the affected input parameters can thereby significantly improve the results, as this could reduce the space of input parameters. Another improvement could be achieved by knowing whether a change has a positive or negative effect. This could be respected with constraints on the solution and the algorithms of Sec. 3.6.

7.4 Combination of Model Updating in Structural Analysis with Imaging with Coda Waves

The focus of this thesis lies in the imaging with coda waves in concrete. Therefore, the question arises of how this is related to the just-described computational model updating. The relationship is multi-layered. From a mathematical point of view, the two methods are an inverse problem in which sensitivity information is related to measurements, meaning mathematically, they are the same. The only difference is that in the computational model updating, the inverse problem is non-linear, as sensitivities change during the model updating. Therefore, improvements in the mathematical part of one

application can also improve the other application. The bigger advantage, however, is that with the developed FEM based imaging with coda waves and the computational model updating that also uses FEM, it is possible to apply both methods on the same mesh. Tab. 7.1 shows the similarities in the overall discretization and system identification (SI) approach as well as the differences in parameters, boundary conditions (BCs), responses and other settings. Note that for the structural-mechanics case, the measurements are a response of the FEM problem, and thus, it's possible to not only localize but also quantify identified changes. For the case of imaging with coda waves, the DC measurements are unitless with $DC \in [0, 1]$ and no direct part of the FEM problem. Thus, the interpretation of the obtained solution from the SI is not as straightforward as in the structural-mechanics case (cf. Sec. 5.2.4).

Table 7.1: Comparison: Coda Imaging - Computational Model Updating.

Physical system	Scattered dynamic waves	Structural-mechanics
Idealization	Diffusion model	Beam model
Discretization	FEM	FEM
Solver type	transient	static
Analysis type	non-linear	non-linear
Dirichlet BCs	transducer	support
Neumann BCs	reflecting boundaries	forces
Important material parameter	diffusivity	stiffness
FEM solution	energy concentration	displacements
Measurements	DC or ε of two ultrasound signals	system responses e.g. displacements, strains
System identification	sensitivity-based	sensitivity-based
Sensitivity analysis	random wave path combinations (Eq. 5.19)	analytic derivatives (Eq. 7.10)
Inverse problem	least-squares formulation with constant $\mathbf{A}$ (Eq. 3.20)	least-squares formulation with $\mathbf{A}(\mathbf{x})$ (Eq. 3.20)
Result of SI	Localization of "new" scatterers e.g. cracks	Parameter adaptation e.g. stiffness (Localization and quantification)

Due to the many similarities of the two methods, combining the evaluation of coda measurements and strain or displacement measurements is possible. The combination can be done in a simultaneous way where the inverse problem of imaging with coda waves and the one of computational model updating are joined to one by stacking the sensitivity matrices and measurement vectors. This combination comes with problems due to magnitude differences in sensitivities and measurement values. More promising would be a successively combination where imaging with coda waves is performed first. This results in a localized damage field, but as mentioned above, it is difficult to directly conclude the magnitude of the solution without complex calibration measurements. A classification could be made possible by applying the known damage field from coda imaging as a filter on the model updating problem so that only detected damage locations are in the set of investigated input parameters. The reduced model updating problem can be used to further classify the detected damage with structural parameters such as stiffness.

Another relation of coda measurements and quantities from structural analysis contains, at least in theory, the stretching factor of the coda signal ε. One can draw conclusions about the stress state by evaluating the stretching factor. Structural analysis can also compute such a stress state in a controlled environment. The relation of the two methods could then be deployed to individually calibrate the pairs in the ultrasound transducer network. Another way is to use measured stress information from ε evaluation in the computational model updating. Overall, there is great potential for synergy effects when combining the two methods in SHM applications. However, combining the two methods comes with immense requirements for the accuracy of the numerical models and the mandatory requirement of measurement technologies for coda imaging and computational model updating in the same specimen.

Chapter 8

Results on Model Updating in Structural Analysis

The computational model updating introduced in Sec. 7.3 is applied in two experiments in this chapter. First is a pure numerical test, where modifying selected parameters creates synthetic measurements. The modification is then identified with computational model updating. Similar to the results of imaging with coda waves in Ch. 6, the numerical framework is deployed to conduct parameter studies. As the aim is to apply the numerical methods to actual structures, the method is, in a second step, tested in a real experiment.

8.1 Computational Model Updating with Synthetic Data

8.1.1 Experimental Setup

The numerically investigated system is a beam with a moving single load applied at several positions. As system response, the displacements at several positions are measured. The number of load positions and displacement measurements varies in the parameter studies. The discretization is also part of the numerical parameter studies. Young's modulus is reduced in a defined section in the numerical experiment. The analysis results of this modified system are used as synthetic measurements. Young's modulus reduction is assumed to be unknown in the model updating workflow and is identified only from the synthetic measurements. An overview of the described experimental setup is shown in Fig. 8.1.

Load positions, displacement measurements, and FE refinement are part of numerical studies. Thereby, four different refinement levels, four different

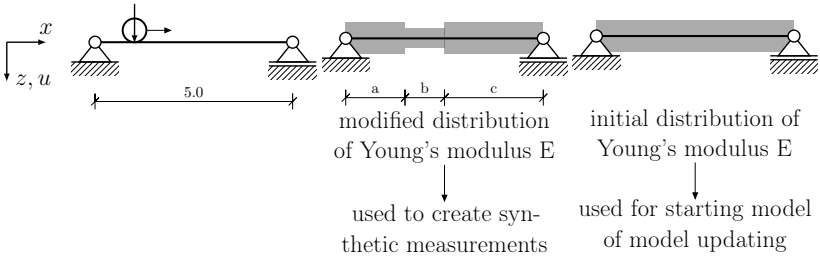

Figure 8.1: Overview of the structural system for the numerical experiment.

amounts of displacement measurements, and three load cases are investigated. Tab. 8.1 gives an overview of the different cases. The numerical weakening of the structure is chosen to be Young's modulus reduction by 20 % in a fixed range. The single loads in this example are only applied to the left part of the beam, as otherwise, many rows in the matrix would be linearly dependent due to symmetry. The state variables $\mathbf{u}$ are computed with a geometrically non-linear computation. Nevertheless, it does not make a difference as the measurements are computed similarly, and therefore, the

Parameters for numerical model updating		
statical system	single-span beam with $l = 5\,\mathrm{m}$ one single load F=100 N applied at x_F	
cross section	rectangular 40 mm×10 mm	
material	steel with $E = 210000\,\frac{N}{mm^2}$	
modification	reduction of E by 20 % in $x = 1.5\,\mathrm{m} - 2.5\,\mathrm{m}$	
FE refinement	10, 20, 40, 1000 elements	
displacement measurements	4 positions	$x_u = 1, 2, 3, 4\,[\mathrm{m}]$
	9 positions	$x_u = 0.5, 1.0, \ldots, 4.5\,[\mathrm{m}]$
	19 positions	$x_u = 0.25, 0.5, \ldots, 4.75\,[\mathrm{m}]$
	39 positions	$x_u = 0.125, 0.25, \ldots, 4.875\,[\mathrm{m}]$
load cases	1 single load	$x_F = 2.5\,[\mathrm{m}]$
	2 single loads	$x_F = 1.25$ and $x_F = 2.5\,[\mathrm{m}]$
	5 single loads	$x_F = 0.5, 1.0, 1.5, 2.0, 2.5\,[\mathrm{m}]$

Table 8.1: Settings for model updating with synthetic measurement data.

effects of the more accurate non-linear computation vanish. Additionally, the system's geometrical non-linearity under the given load is nearly linear and, therefore, neglectable.

In the parameter studies, the amount of unknowns is defined by the FE refinement, so between 10 and 1000. The combination of measured responses and load cases defines the amount of measurements. The example of Fig. 8.2 with four displacement measurements and one load case for refinement with ten elements shows the least amount of measurements. The maximum amount is 39 displacement measurements combined with five different load cases, which makes a total of 195 measurements. Depending on the chosen settings, the obtained inverse problem for model updating is either over- or underdetermined.

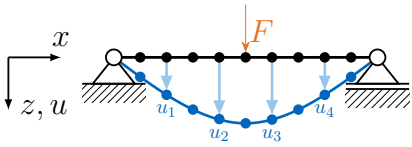

Figure 8.2: Example of four response measurements (u_i), one load case, and a refinement with ten elements.

8.1.2 Results of Computational Model Updating with Synthetic Data

With various parameters from Tab. 8.1 investigated, the evaluation of the results is complex. In the numerical experiment, where the damage location is precisely known, the residual evaluated for assessing the result is the difference of input parameters $\hat{\mathbf{x}}_{\text{updated}}$ and the actual input parameters $\mathbf{x}_{\text{known}}$. This differs from the minimized residual of responses. In the optimization, the residual of Eq. 7.15 is minimized but does not give direct information on how accurate the obtained solution is. Fig. 8.3 shows convergence plots for the four different refinements and an evaluation of how the amount of evaluated system responses relates to the remaining residual of input parameters. For an easier comparison, a constant y-axis is used in all diagrams. Starting with the refinement of 10 elements, the deviation of the obtained solution from the targeted one is zero for nearly all cases. Only with the least number of measurements could the obtained solution be better. With the refinement of 20 elements, one can see the effect of the amount of measured responses and load cases very clearly. To visualize the obtained residuals of the solution, Fig. 8.4 and Fig. 8.5 show results for the refinement with 20 elements and different densities of the measured responses. The figures are structured as follows: On the left is an overview of the evaluated load case and measured responses. These positions are also indicated on the right in light blue and

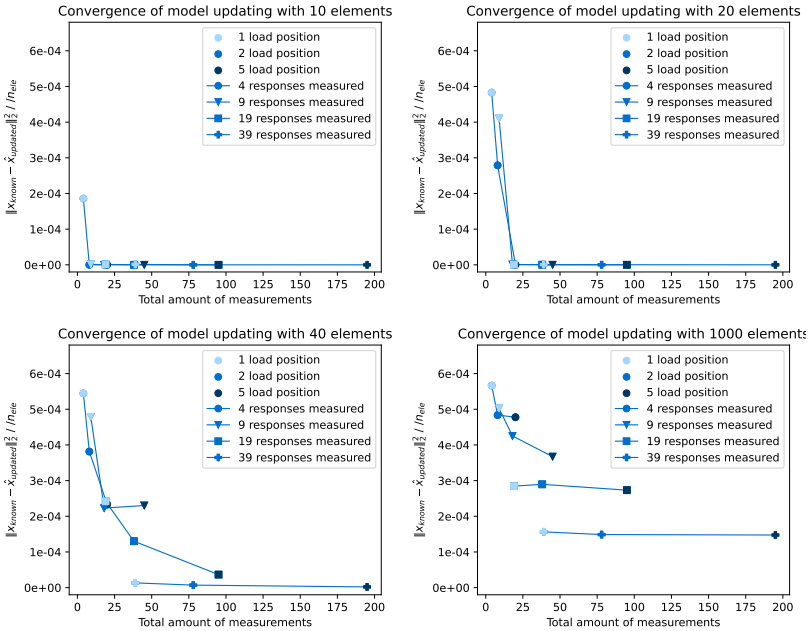

Figure 8.3: Convergence study on model updating with different element refinements.

orange. On the right side of the figure is the obtained solution for Young's modulus distribution plotted over the element length in grey. The black dotted lines indicate the actual applied modification to be identified.

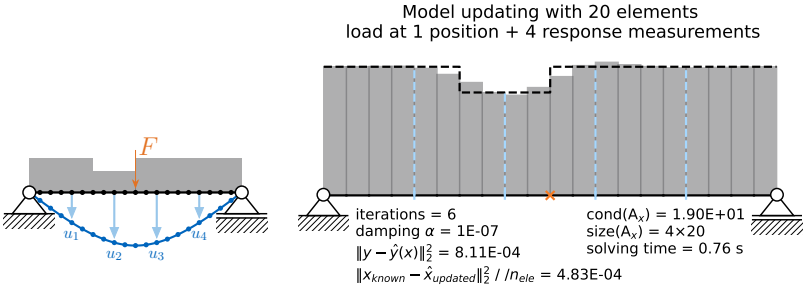

Figure 8.4: Model updating with 20 elements and four measurements.

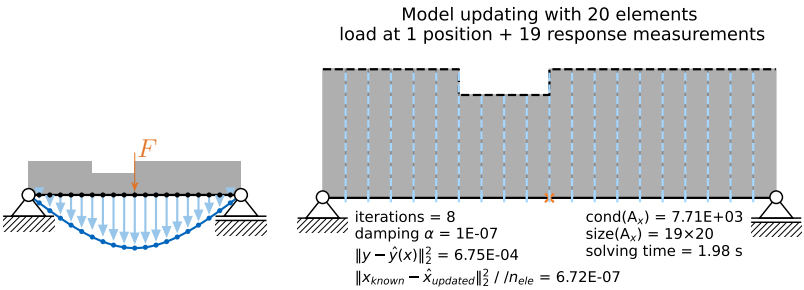

Figure 8.5: Model updating with 20 elements and 19 measurements.

For the case of 4 responses (Fig. 8.4), the discrete jump of the applied change in Young's modulus is not identified precisely and is only approximated. For the case of 19 response measurements (Fig. 8.5), where every nodal displacement is measured, the jump is, however, precisely identified, and the remaining error of the solution is nearly zero. This already indicates a result that becomes more evident with more elements: the refinement of points where either a load acts or a response is measured is crucial for the accuracy of the obtained solution. The observation is underlined by the convergence study with 40 and 1000 elements. With 40 elements, the remaining error is nearly zero for the fine refinement where every FE node displacement is measured. For the coarser measurements, one can see that an increase in load positions improves the result. However, the increase in response measurements has a larger effect, as one can see, e.g., at approximately 40 total measurements. This is also visible for the refinement with 1000 elements. Here, an increase in load cases does not affect the cases of 19 and 39 response measurements. However, an increase in measured responses significantly reduces the error. What is interesting about the 1000-element refinement is that it is unproblematic to have fewer measurements than unknowns for the mathematical solving part. Fig. 8.6 shows the solution with only four measurements in total. One can see that a rough identification of the applied modification is possible. The solution also shows that in between the points of response measurements, the solution interpolates linearly. A similar development can be seen in the refinement with 20 elements in Fig. 8.4. The solutions are, in fact, very similar, only that with 1000 elements, the linear interpolation is more evident. For the given example, this leads to the conclusion that the obtained solution is mesh-independent for a strongly underdetermined inverse problem.

Overall, the numerical study verifies the numerical model updating workflow. The study showed a dependency of the obtained solution on the number of load positions and response measurements. The response measurements' density has a larger effect in the given example. The observed linear interpolation of the solution between response measurements is remarkable and could help to optimize sensor placement, a field with immense potential for future

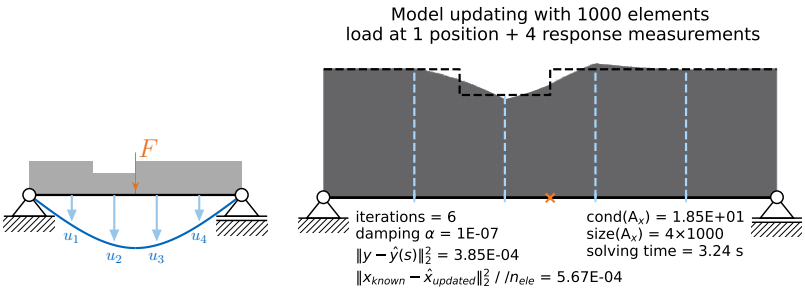

Figure 8.6: Model updating with 1000 elements and four measurements.

research. Due to the linear behavior between response measurements, the solution primarily depends on load and measurement positions rather than the mesh refinement. The finer mesh, however, helps to represent courses more accurately.

8.2 Computational Model Updating at a Real Experiment

8.2.1 Experimental Setup

With a successful verification of the numerical model updating, the method is tested with real measurements for further validation. Therefore, an experiment similar to the numerical one is carried out. A single-span beam with a length of 1.8 m is loaded with a single load at 17 positions. The static loading is applied with weights. The weight is chosen such that the material is still in its elastic range under maximum load (load at $l/2$), but deflections are as large as possible. Staying in the elastic range allows for the repetition of the experiment, and the larger the deformations, the smaller the influence of measurement errors. For displacement measurements, white dots are attached to the beam that can be tracked with digital image correlation (DIC). Therefore, pictures are taken with a camera (Fujifilm X-T30 with 26.1-megapixel sensor) and evaluated using the software GOM Correlate [149]. The beam is an aluminum rod with an 8 mm × 8 mm cross-section. As a modification, the beam can be stiffened by attaching another 8 mm × 8 mm aluminum rod with a length of 170 mm with five screws at defined positions. The attachment with screws allows the experiment to be repeated, as no permanent changes are made. Tab. 8.2 gives an overview of all settings. Fig. 8.7 and Fig. 8.8 show photos of the experiment.

Parameters for model updating at real experiment		
statical system	single-span beam with $l = 1.8\,\text{m}$ one single load F=16.74 N applied at x_F	
cross section	rectangular 8 mm×8 mm	
material	aluminium with $E = 69000\,\frac{N}{mm^2}$	
modification	stiffening of structure in range of $x = 0.78\,\text{m}$ $-0.95\,\text{m}$	
FE refinement	180 elements (l_{ele}=10 mm)	
displacement measurements	33 positions	x_u in range of $x = 0.27\,\text{m}$ $-1.40\,\text{m}$ approx. every 30 mm
load cases	17 positions	x_F every 0.1 m from 0.1 m to 1.7 m

Table 8.2: Settings for model updating with real measurement data.

The FE model is refined with 180 elements, equal to an FE element length of 10 mm. In the computations of displacements and sensitivities, geometrical non-linearities are respected. Computation results were compared to the actual measurements to validate the numerical model. The comparison showed that choosing the actual static system is not straightforward. The

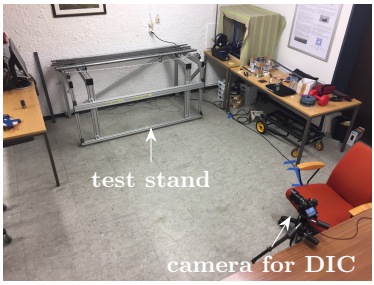

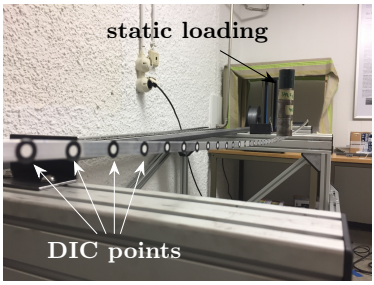

Figure 8.7: Setup of test stand with DIC displacement measurements under static loading.

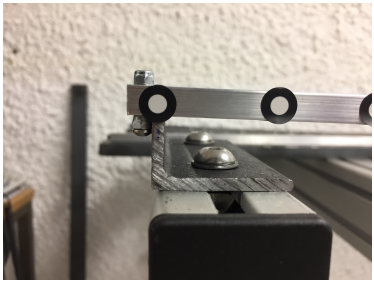

Support on both sides

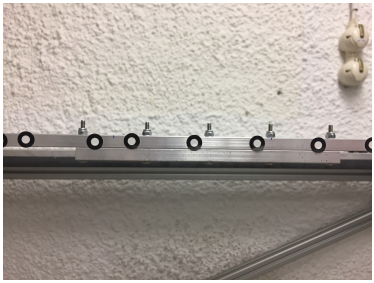

Stiffening

Figure 8.8: Details of the support and applied modification (stiffening) of the system.

detail of the support in Fig. 8.8 could lead to the assumption that both supports are assumed to be fixed as the movement toward the inside is blocked. In non-linear analysis, this leads to significant normal forces that stiffen the structure and reduce the maximum displacement. As the measured displacements are larger than the computed ones, the assumed rigid support on both sides is questionable. A computation with moving support on one side came closer to the measured values but still contained a significant error. The appropriate solution is a spring whose stiffness is calibrated with numerical model updating. Next to the boundary conditions, there are several other uncertainties (e.g., assumed Young's modulus, manufacturing-related residual stresses, pre-tensioning due to fixing the mounting position, etc.)and modeling errors (e.g., neglection of boreholes for stiffening, simplification with point load, etc.). In order to compensate for these modeling errors that have an enormous influence when using absolute displacement measurements, relative displacement measurements are used. Therefore, the experiment was conducted twice, once without and once with modification, and the used measurements for model updating are the difference between the two (cf.

Fig. 8.9). This has the advantage that the initial computation model does

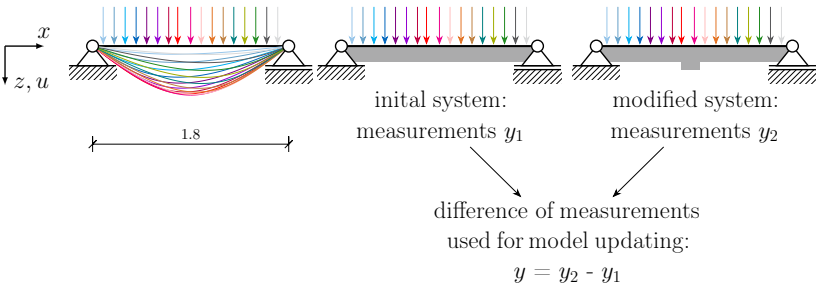

Figure 8.9: Overview of the real experiment. Colors represent the different load cases.

not need to be fully calibrated to match the measurements in the best way possible. For localization, it is sufficient to have a correct statical system, but the influence of the exact boundary conditions is limited as it is the same in the two measurements. Nevertheless, this fix avoids a full calibration and reduces uncertainties. However, to use the model for predictions or other extrapolations, one needs to apply the computational model updating for full calibration and the best possible modeling of all known non-linearities and specialties.

Displacement measurements are evaluated with DIC using the software GOM Correlate [149]. Per load position, five pictures are taken to reduce measurement errors and get insight into the accuracy that lies between 10^{-1} mm to 10^{-2} mm. This high accuracy is helpful as the initial and modified system deflection difference is around 1 mm. Fig. 8.10 shows the DIC results under maximum load. A difficulty in the data processing was that some measurement points, especially in the areas near the supports, were not tracked at all load positions. These measurements were not used as data, leading to 33 trackable points.

8.2.2 Results of Computational Model Updating at a Real Experiment

The first result is already mentioned above, namely the difficulty of fully calibrating an initial model such that computational results are matched to absolute measurements. By only measuring relative changes in the displacement (cf. Fig. 8.9), the large influence of uncertainties in the boundary conditions reduces significantly. The finally obtained measurements are shown in Fig. 8.11 and are the difference of displacement in the modified (u_2) and initial system(u_1): $u = u_2 - u_1$.

The most significant difference in deformations between the two systems is in the middle section, where deformations are the largest, and modification is applied. It is also very conclusive that the deformations on the stiffer system are smaller, and the difference is negative. The relative measurements are

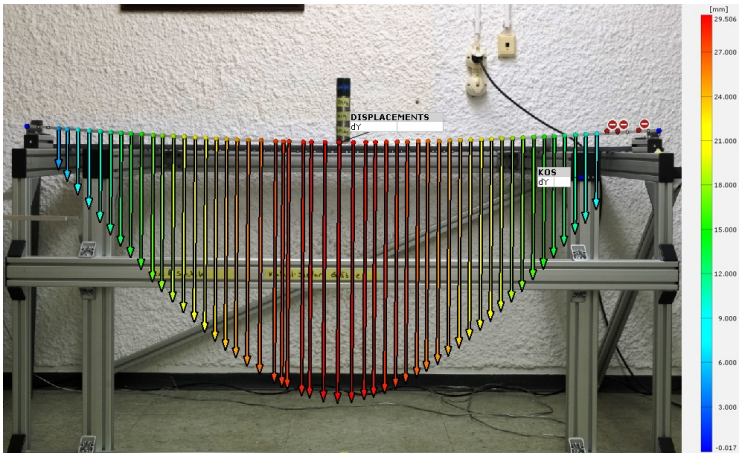

Figure 8.10: DIC results from GOM Correlate for load in the middle of the beam.

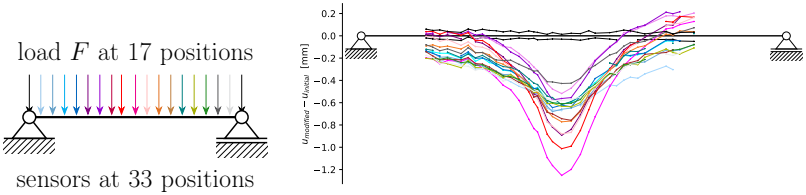

Figure 8.11: Used relative measurements of the real experiment.

positive in the edge areas of the measuring field, which should not be the case. The error on the right is especially evident. An inaccurate test setup is identified as a possible cause here. As the camera button was pressed multiple times directly on the camera during the experiment, there is a chance that the position, especially the camera angle, has minimally changed. At first glance, such a tiny change might not be visible, but considering the high accuracy of DIC, it can be a factor. This significant measurement error is a considerable handicap for the numerical model updating. In this thesis, no further pre-processing of the data that tries to reduce such an error is conducted. However, the visible error is instead regarded as a challenge in terms of robustness for practical applications of the method.

Eq. 7.18 and Eq. 7.20 are applied for the numerical model updating. As the problem is ill-posed, it needs regularization. Therefore, the L-curve method is applied to obtain an optimal damping factor, similar to the imaging with coda waves. Results are shown in Fig. 8.12, and one can see that the typical L-shape is not obtained. In the figure, one can see how different

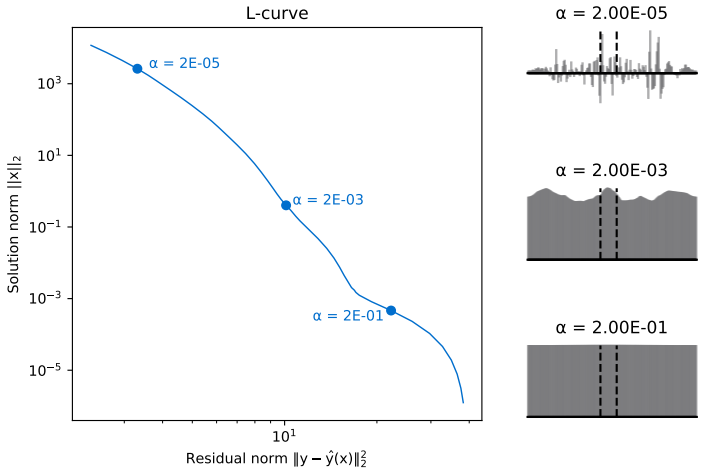

Figure 8.12: L-curve method for determining the damping factor α.

damping factors affect the solution, as a low factor (2×10^{-5}) creates a highly oscillating result, and a rather large factor leads to no changes, which also becomes evident when looking at the magnitudes of the y-axis. As the L-curve method does not yield a good result, the optimal damping factor is chosen from a visual comparison of the obtained solutions, in this case, 2×10^{-3}. The result is shown in Fig. 8.13. The figure is structured like the ones in the previous section. On the left is an overview of load and measurement positions, and on the right, the obtained solution is plotted in grey over the beam length. The black dotted lines thereby indicate initial values (horizontal line) and the location where the modification that is to be located is applied (vertical lines). As the actual magnitude of the stiffening is not known only the position is indicated.

The result from updating the numerical model locates a stiffening in the range of the applied modification, which is a good result. However, areas near the support are also identified as stiffened, which is false. A possible reason is the comparatively small sensitivity in that area and the lack of measured responses near the support. This problem of small sensitivities is the opposite of the issue with the sensitivity peaks for imaging with coda waves. The issue of these small sensitivity values affecting the solution is addressed by Link [68] and Mottershead et al. [138] who use Eq. 7.21 as the inverse covariance matrix of the input parameters instead of $\mathbf{C}_X^{-1} = \alpha^2 \mathbf{I}$ used so far in this thesis. Results with the different term for $\mathbf{C}_X^{-1}$ are shown in Fig. 8.14.

In the middle, the result looks similar to the previous one, but the areas near the supports are no longer modified. Therefore, the different inverse covariance matrix of the input parameters is a good improvement for the

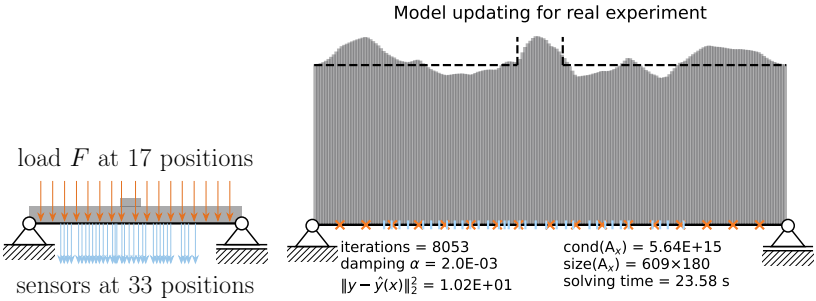

Figure 8.13: Model updating at real experiment with Eq. 7.18 and Eq. 7.20 with $\mathbf{C}_X^{-1} = \alpha^2\mathbf{I}$.

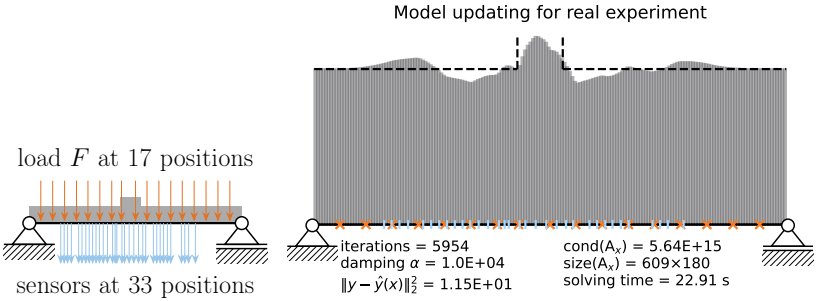

Figure 8.14: Model updating at real experiment with Eq. 7.18 and Eq. 7.20 with $\mathbf{C}_X^{-1}$ from Eq. 7.21.

algorithm. The maximum stiffness increase is 20.9 %, and the maximum stiffness reduction is 9.31 %. The reduction appears in the areas left and right of the modification and is a wrong identification. The problem can be improved by respecting further knowledge about the modification in the numerical model updating workflow. In reality, it is conceivable that an engineer knows if stiffness has either only decreased, e.g., due to cracks, or increased. This knowledge can be respected with constraints on the solution algorithm of Eq. 7.18 by applying the Projected Gradient Descent Method of Sec. 3.6.1. Doing so ensures a range of possible solution values during the solving process. For the given case of a local stiffening, the constraint is a non-negativity constraint on the input parameter update $\Delta\mathbf{x}_k$. Fig. 8.15 shows the obtained solution with the constraint.

The obtained solution is remarkably accurate in locating the modification

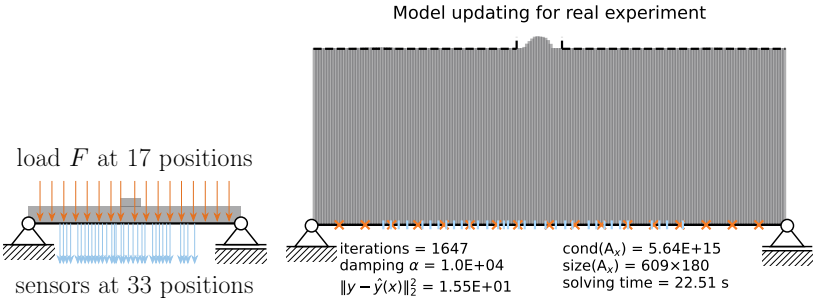

Figure 8.15: Model updating at real experiment with Eq. 7.18 and Eq. 7.20 with $\mathbf{C}_X^{-1}$ from Eq. 7.21 and non-negativity constraint on solution.

and a notable good result. However, the magnitude with a stiffness increase of 5.06 % is less than one would expect and less than the previous result. When looking at the stiffening detail in Fig. 8.8, one can see that the cross-section is doubled. The stiffness, however, strongly depends on the bond between the two rods. This bond strongly depends on factors such as tightening and slipping of the screws and friction between the two aluminum rods. As aluminum is a relatively soft metal, the stiffening effect may be significantly lower than the computed value. Therefore, this significant uncertainty on the actual applied modification limits the conclusions about damage quantification.

8.3 Conclusion on Computational Model Updating

This chapter derived and successfully applied computational model updating. The basis for a universal application of the method is created with a focus on the derivation of required sensitivities used in the inverse problem. This chapter used displacements as measurement data, but generally, any quantity that appears in the FE problem can be used. As the method relates digital models to real measurements, it is one possible core technology of DTs. Numerical investigations with synthetic measurements verified the successful application and showed the limits. Surprisingly, a substantial deficit between the amount of measurements and unknowns in the inverse problem does not cause problems with the algorithms for ill-posed problems. The accuracy of the solutions is also strongly related to the number of measured responses. The numerical investigations showed that the obtained solution interpolates linearly between response measurements. With the application-oriented approach of this thesis, the method was also tested using a real experiment. The measurement data itself, however, showed significant implausibilities. Nevertheless, the localization of the modification was successful, which shows that the method is robust to a certain extent. In theory the computational

model updating also allows for quantification. This, however, requires a well-calibrated initial model and a more accurate set of measurement data. Due to a simple setup and the tools available, such an accuracy was not achieved. Conclusions about the damage quantification would require further experiments to calibrate stiffness values at the support, the beam itself, and the stiffening. Working localization with simple tools is a successful proof of application at real structures and an excellent improvement for measurement data evaluation to gain further insight into structures. This leads towards the desired digital twin for SHM, where the numerical model updating plays a crucial role.

Chapter 9

Conclusions and Outlook

The aim of this work is method developments as a contribution to a DT for large structures. The integration into an overall monitoring concept of buildings using a DT shows several challenges. The basis of the DT is a constant exchange of model and reality, which places enormously high demands on the numerical models and represents a significant difficulty. Additionally, the goals of the presented DT that aim for autonomous, predictive maintenance are very ambitious. SHM technologies are also very diverse, and focusing on only one technology, e.g., CWI, is not enough. Ultimately, it is necessary to have universal methods that contribute individually towards better digital models that are part of the DT. It is also necessary to combine different technologies in one digital model. Methodological developments are performed, in particular, to localize damage with coda waves. Additionally, the universally applicable, and to a certain extent, core method of DTs, the computational model updating, is discussed and applied in this thesis. The discussion of mathematical principles shows that the fundamentally different measurement systems are almost identical mathematically. In both methods, an inverse problem is formulated and solved with local sensitivity information. The only difference is that sensitivities of the coda waves are independent of the to-be-identified input parameter "damage", whereas in computational model updating, the inverse problem is non-linear as sensitivities depend on the input parameters. However, the many parallels make it possible to transfer algorithms and findings from one application to another and vice versa. The application-oriented focus of this thesis is reflected in the structure of the experiments. Both investigated methods were first developed and tested at a numerical level in order to subsequently apply them in real experiments. The step up to the application in reality is always associated with many difficulties. However, to make the whole thing a real DT, it is indispensable and a special achievement of this work.

The focus of methodological developments in this thesis is on damage localization with coda waves. By homogenizing the highly complex diffuse spread of ultrasound waves in concrete, the complex phenomena are transferred to a simpler diffusion problem, which can also be solved for large geometries. Previous studies [20–22] used analytic solutions to the diffusion problem. In this thesis, FEM is used to solve the diffusion problem. FEM is a well-established method to solve different kinds of partial differential equations. A significant advantage is that any geometry can be modeled and solved using unstructured meshes. The modular structure of the imaging workflow also allows for the exchange or improvement of the diffusion problem, with one better suited for representing the scattered ultrasound waves in concrete. In this thesis, the modular structure is utilized to combine the FEM solution with analytic radiation terms from the RTE that, according to literature [23, 115], are better suited to describe the coda waves in areas close to the transducer. The combination of the primary solution with FEM to allow geometric flexibility and local improvement through radiation terms is a promising novelty. A particular challenge in this work was the central frequency of the ultrasound waves of 60 kHz. Published applications of damage localization [20–22] worked with higher frequencies where the signal is scattered more often. As the scattering behavior is a central element of the simplification that the multiple scattered ultrasound waves can be approximated with a diffusion simulation [113] and the model for computing the sensitivities [122] is also based on this assumption, the low frequency is a significant challenge. In order to meet this challenge, the current state of the art was simulated in numerical experiments, and extensive parameter studies were carried out on all possible input parameters. Found settings were then applied to a laboratory experiment with 60 kHz as the central frequency. An investigation of the signals has suggested that with a sufficient dwell time of the signals in the specimen, even a 60 kHz signal is scattered sufficiently often to apply the models based on multiple scattering. Nevertheless diffusivities obtained from an envelope fitting show a large variance and are implausible. A typical problem of the CWI based damage localization is a correlation of the obtained solution with the transducer network that can also be found in literature [124, 125]. This thesis avoids the effect by limiting the sensitivities in transducer regions to a fraction of the maximum. The modification improves the obtained solution and increases the robustness to implausible measurements. Results of the laboratory experiment show the immense sensitivity of coda waves to microscopic changes that happen before the first microcracks occur. With many cracks appearing close to each other, the individual localization of each crack was not always possible, but a robust identification of the damage zone works. This is generally sufficient for CWI as supporting technology in an integral SHM concept where several technologies work together. A novelty of this thesis with great results is using the measured phase shift in the signals for the inverse problem of damage localization. So far, the DC is the only used measurement of the coda signals used for imaging. The use of phase shifts is explained with a general interpretation of the coda sensitivities that goes beyond scattering and resulting waveform distortion. Results show a good identification of cracking regions and correctly distinguishing pressure

and tension zones. The successful application of the developed method in a real, large building again underlines the technology's great potential and paves the way for its use in practice. Summarized key contributions in the field of CWI of this thesis are

- Successful development and demonstration of low-frequency imaging in numerical, laboratory, and field experiments.
- Methodological developments through the use of FEM.
- Improvements in accuracy through the consideration of radiation terms in the FEM solution.
- Overall robustness improvement through sensitivity modifications.
- Novel use of phase-shift as measurements in the inverse problem.

One problem of damage localization with CWI is the classification and quantification of localized damage. However, the thesis shows indicators that become visible with permanent monitoring under increasing load. Motivated by the difficulty of classifying damage, another method was developed that promises to quantify structural changes: computational model updating. The detailed explanation of the method allows the transfer to different measurements. The graphical explanations of the inverse problem also make the close parallelism to damage localization with CWI clear. To apply it in the context of a DT, the method is developed and examined in a numerical framework and later applied in a real experiment. However, a considerable measurement error is directly recognizable due to the simple measurement setup. Nevertheless, it is possible to localize system modifications correctly. Only the correct quantification does not succeed, as higher demands are placed on the accuracy of the measurements and models. Nevertheless, the method is one possible core technology of DTs as it allows the communication of the digital model with reality to ultimately improve the model in accuracy and reliability.

Outlook Lately, there has been much research about DTs. The recent report of the Federal Ministry for Digital and Transport in Germany on DTs for bridges is just the latest chapter. It underlines the recent trend and its importance. Goals and the actual status quo of DTs in civil engineering are, at the moment, far apart. Current projects [45–47] realize a capability level of 2 out of 5. In order to achieve higher capability levels, combining different SHM technologies in an integral monitoring concept is required. The measurement technologies need to be chosen so that they complement each other in a meaningful way. In the digital models, there is a need for modular and universal structures to enable exchange and data fusion. It should also be noted that the solution space is deterministic for the presented imaging methods based on discrete sensitivities. Despite validation with real measurements, values are always subject to uncertainties. Therefore, one should incorporate these uncertainties into the DT (e.g., via Bayesian updating).

With a focus on coda waves in this thesis, the topic is a good starting point for future research and improvements. One of the evident problems is a strong correlation of the source-receiver distance to obtained diffusivities from an envelope fitting of the signals with the solution of the diffusion problem (cf. Fig. 6.21). Even though the imaging workflow worked with the used diffusivities, one could improve the solution by respecting the derivation of the obtained individual diffusivity from the used one in the covariance matrix of the measurement data. The practical application of CWI in a large building has shown great potential. Now, strategies are needed to use the technology as SHM during operation. With CWI being sensitive to many influences, a big difficulty is to filter the desired quantity. Therefore, further investigations on the individual environmental influences and their superposition or intelligent choices of the reference signal are good starting points for further research. A conceivable goal for practical applications is, for example, to calibrate the CWI so that an alarm is activated when limit values are exceeded, leading to a local inspection. In the final instance, such processes should be as automated as possible. With a working imaging workflow in both the CWI imaging and computational model updating, future research could also address the question of optimized sensor placement to find a good trade-off between accuracy and necessary hardware.

The insight into structures with NDT also allows the numerical models to be calibrated better. If one finds ways of incorporating the stress information measured with CWI (that appears in the phase shift of the coda waves) into a structural model, this would have immense potential in several respects. On the one hand, it would be easier to classify damage with CWI measurements, which is one of the remaining challenges. The measurement data from large areas within the structure would also make it possible to calibrate the computation models more precisely, which evens the way for potential forecasts for the future. Ultimately, this would further improve the safety of the existing infrastructure and enable long-term, forward-looking planning.

Appendix A

Results for Coda Imaging at Laboratory Experiment at All Load Steps

The following figures relate to Sec. 6.2. The reader is referred to this section for an explanation of the related experiment. The contents of the figures are structured as follows: On the top half, the modeled geometry is shown with light grey, indicating the used sensor pairs. Blue shows the damage localization with CWI on a scale shown on the right. The red line indicates the position of the FOS, whose measurements are shown in the bottom half of the figure. In the FOS measurement, peaks indicate cracks.

A.1 Standard Damage Localization

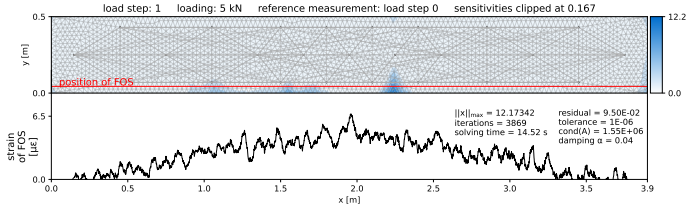

Figure A.1: Damage localization at load step 1.

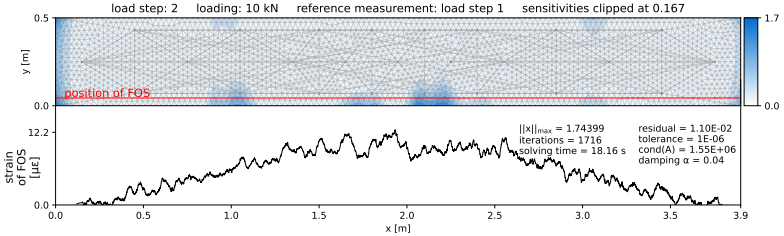

Figure A.2: Damage localization at load step 2.

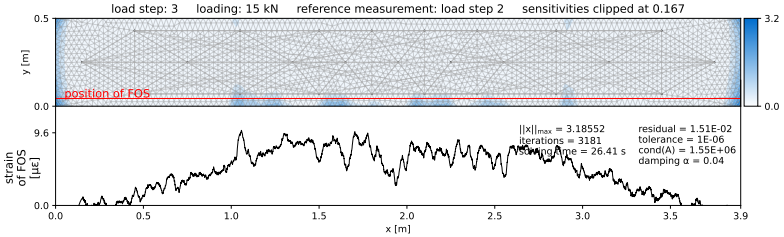

Figure A.3: Damage localization at load step 3.

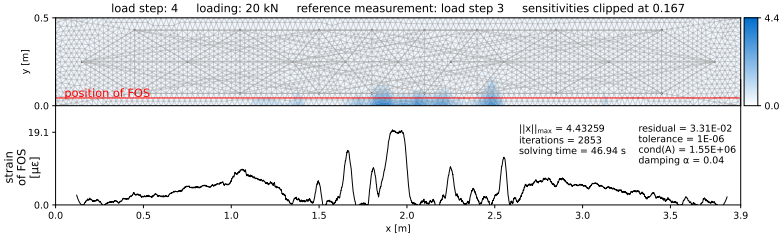

Figure A.4: Damage localization at load step 4.

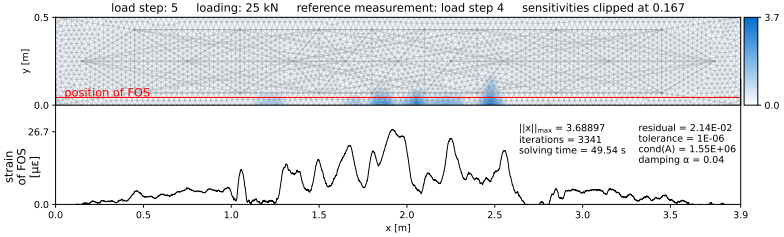

Figure A.5: Damage localization at load step 5.

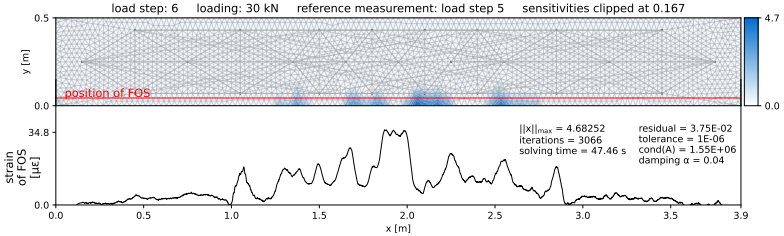

Figure A.6: Damage localization at load step 6.

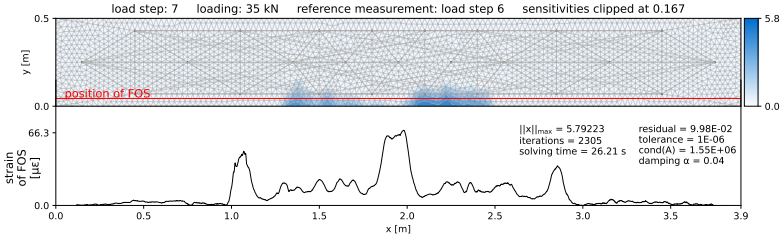

Figure A.7: Damage localization at load step 7.

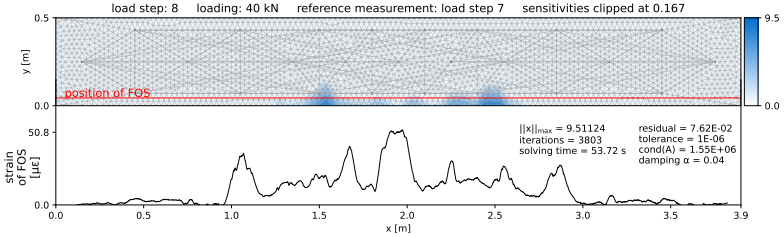

Figure A.8: Damage localization at load step 8.

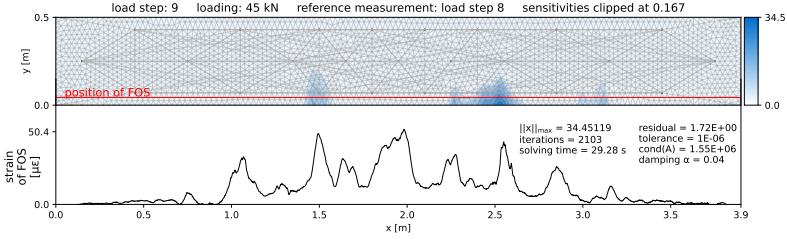

Figure A.9: Damage localization at load step 9.

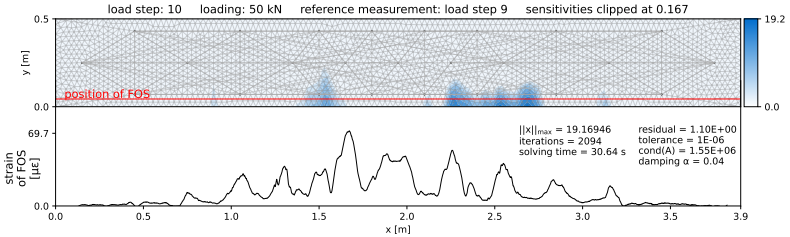

Figure A.10: Damage localization at load step 10.

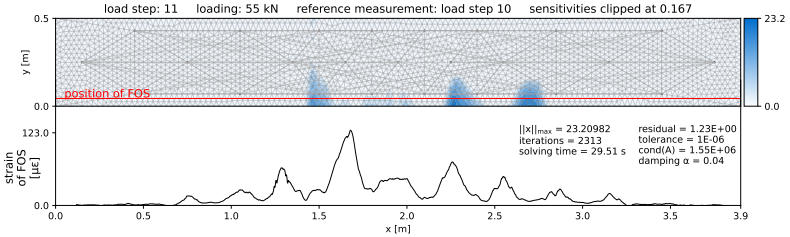

Figure A.11: Damage localization at load step 11.

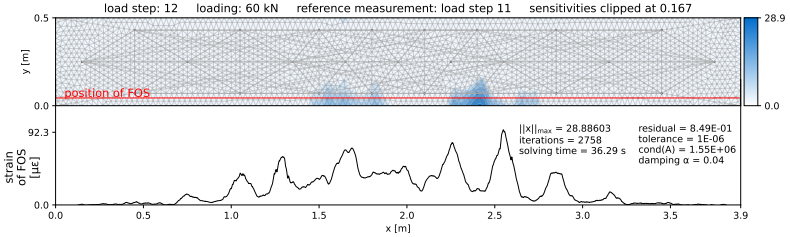

Figure A.12: Damage localization at load step 12.

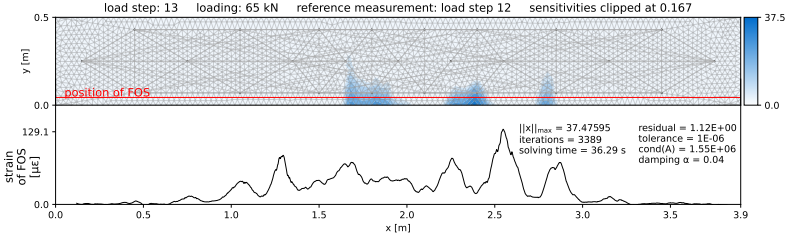

Figure A.13: Damage localization at load step 13.

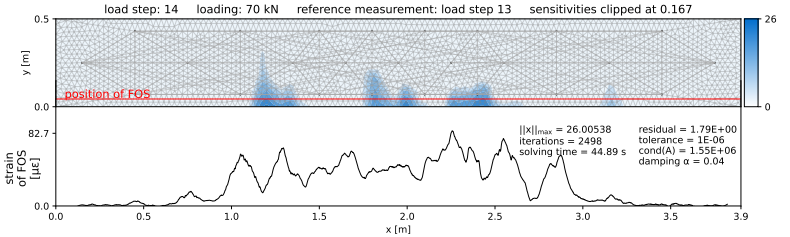

Figure A.14: Damage localization at load step 14.

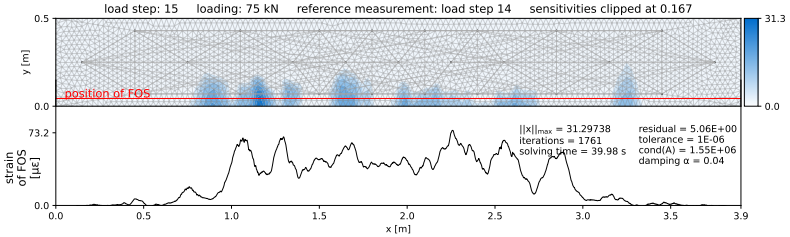

Figure A.15: Damage localization at load step 15.

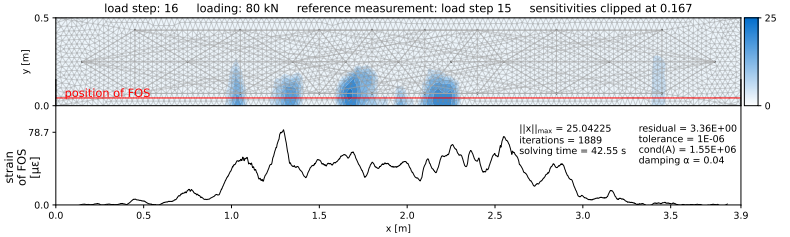

Figure A.16: Damage localization at load step 16.

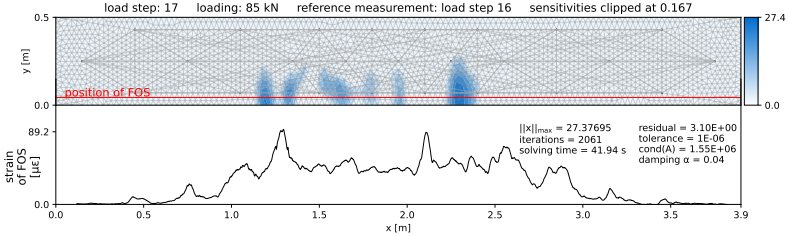

Figure A.17: Damage localization at load step 17.

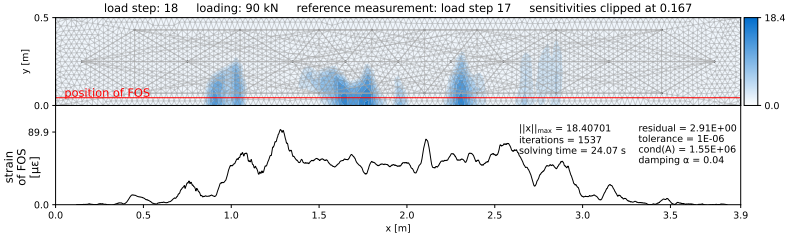

Figure A.18: Damage localization at load step 18.

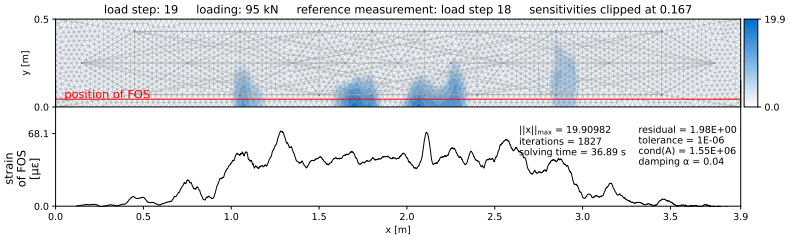

Figure A.19: Damage localization at load step 19.

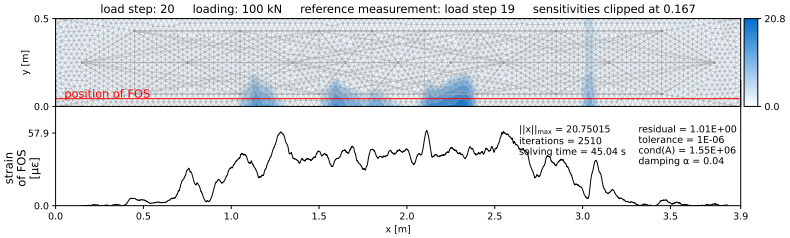

Figure A.20: Damage localization at load step 20.

A.2 Damage Localization with ε as Measurement

Refer to Sec. 6.2.5.2 for further explanations on the figures below.

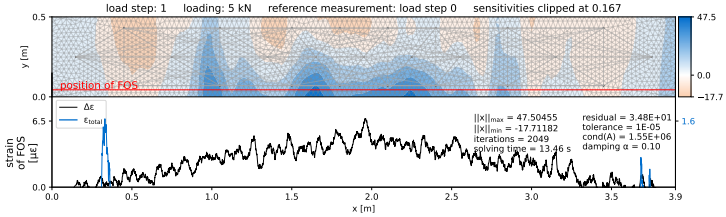

Figure A.21: Damage localization with $\frac{\partial}{\partial v}$ at load step 1.

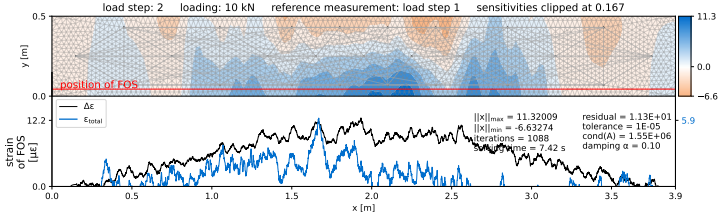

Figure A.22: Damage localization with $\frac{\partial}{\partial v}$ at load step 2.

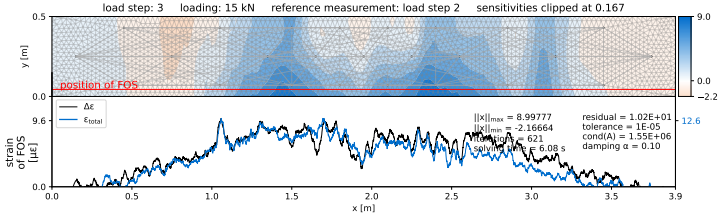

Figure A.23: Damage localization with $\frac{\partial}{\partial v}$ at load step 3.

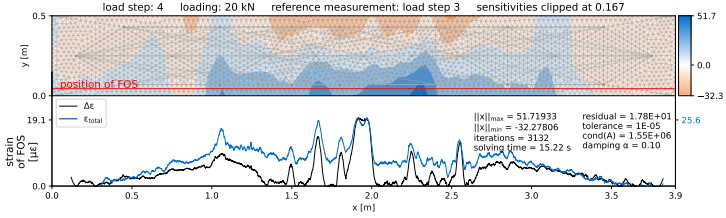

Figure A.24: Damage localization with $\frac{\partial}{\partial v}$ at load step 4.

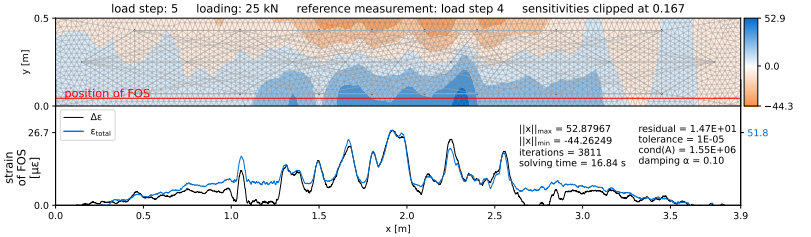

Figure A.25: Damage localization with $\frac{\partial}{\partial v}$ at load step 5.

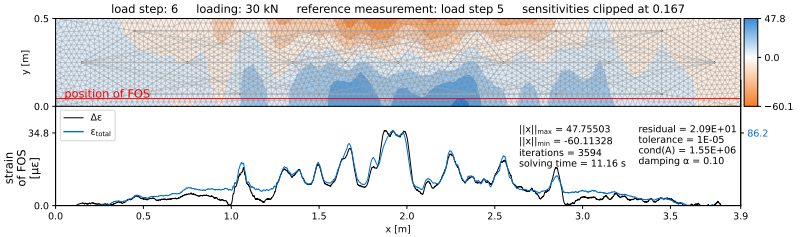

Figure A.26: Damage localization with $\frac{\partial}{\partial v}$ at load step 6.

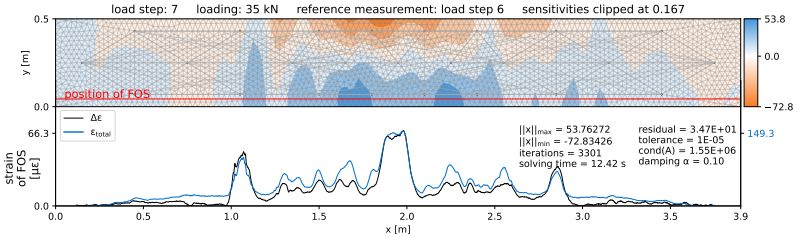

Figure A.27: Damage localization with $\frac{\partial}{\partial v}$ at load step 7.

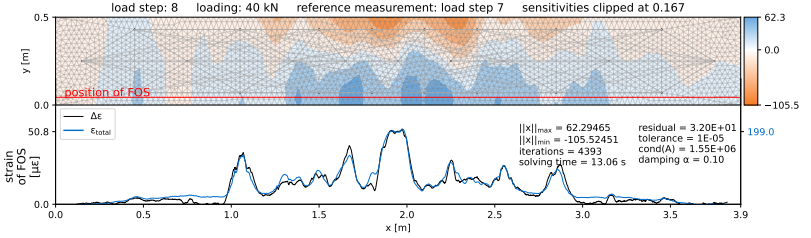

Figure A.28: Damage localization with $\frac{\partial}{\partial v}$ at load step 8.

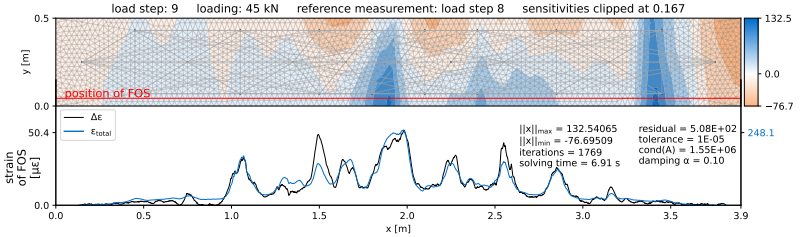

Figure A.29: Damage localization with $\frac{\partial}{\partial v}$ at load step 9.

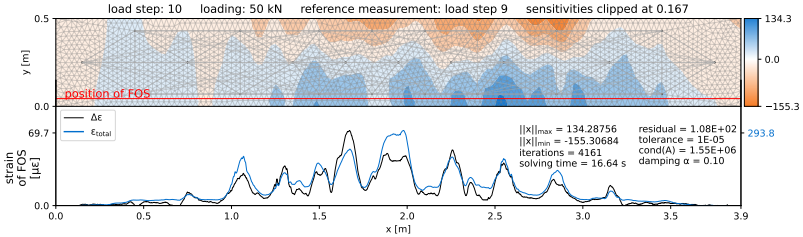

Figure A.30: Damage localization with $\frac{\partial}{\partial v}$ at load step 10.

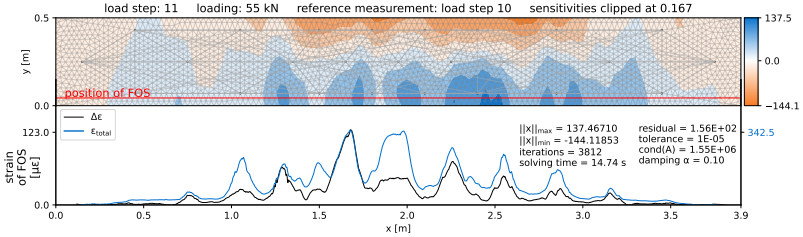

Figure A.31: Damage localization with $\frac{\partial}{\partial v}$ at load step 11.

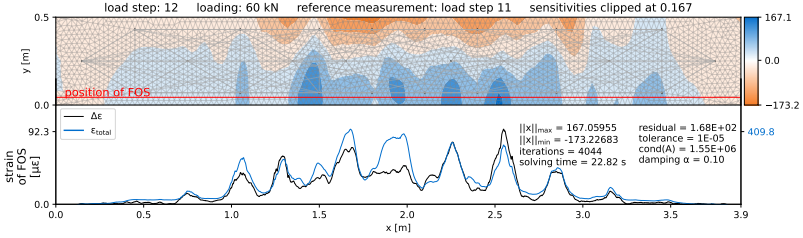

Figure A.32: Damage localization with $\frac{\partial}{\partial v}$ at load step 12.

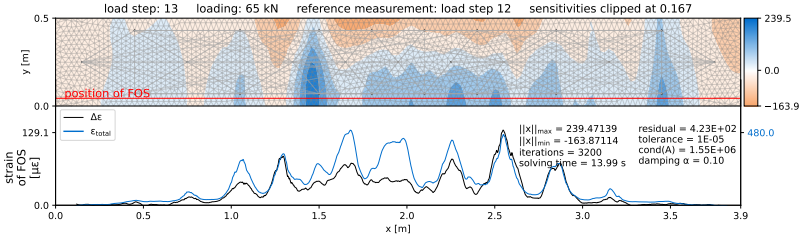

Figure A.33: Damage localization with $\frac{\partial}{\partial v}$ at load step 13.

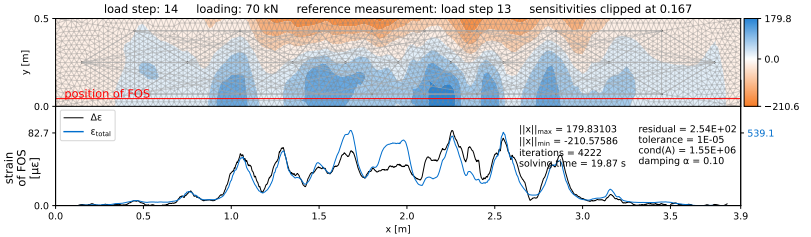

Figure A.34: Damage localization with $\frac{\partial}{\partial v}$ at load step 14.

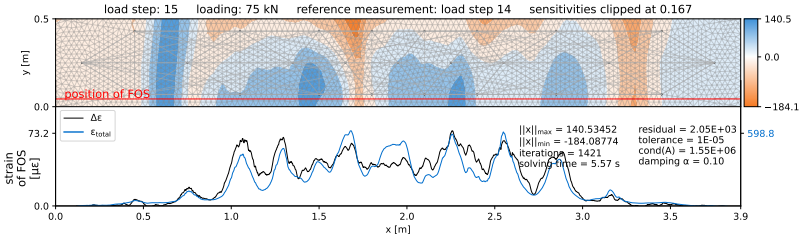

Figure A.35: Damage localization with $\frac{\partial}{\partial v}$ at load step 15.

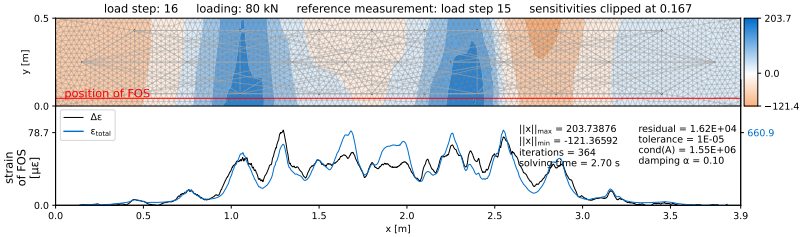

Figure A.36: Damage localization with $\frac{\partial}{\partial v}$ at load step 16.

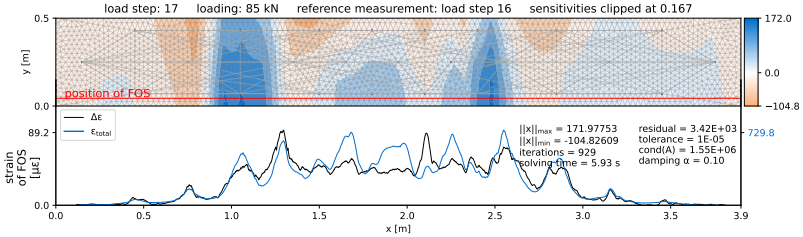

Figure A.37: Damage localization with $\frac{\partial}{\partial v}$ at load step 17.

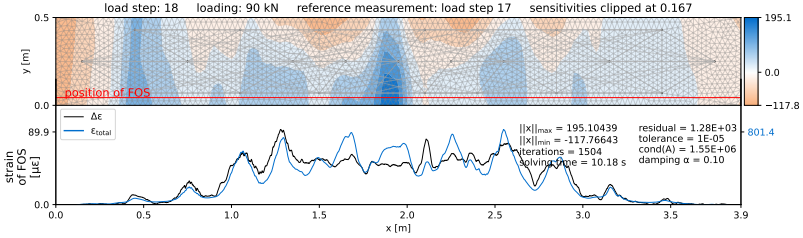

Figure A.38: Damage localization with $\frac{\partial}{\partial v}$ at load step 18.

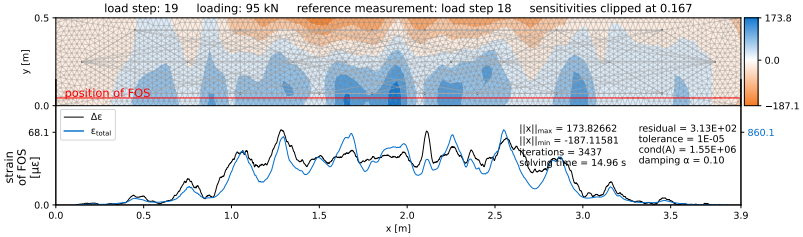

Figure A.39: Damage localization with $\frac{\partial}{\partial v}$ at load step 19.

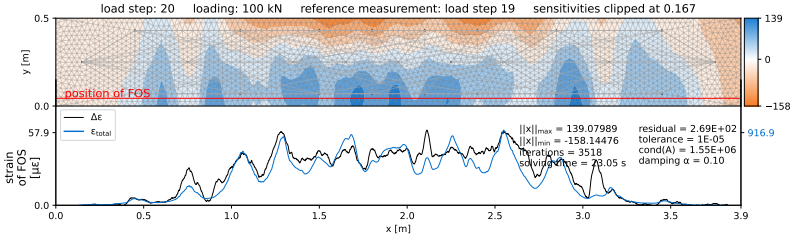

Figure A.40: Damage localization with $\frac{\partial}{\partial v}$ at load step 20.

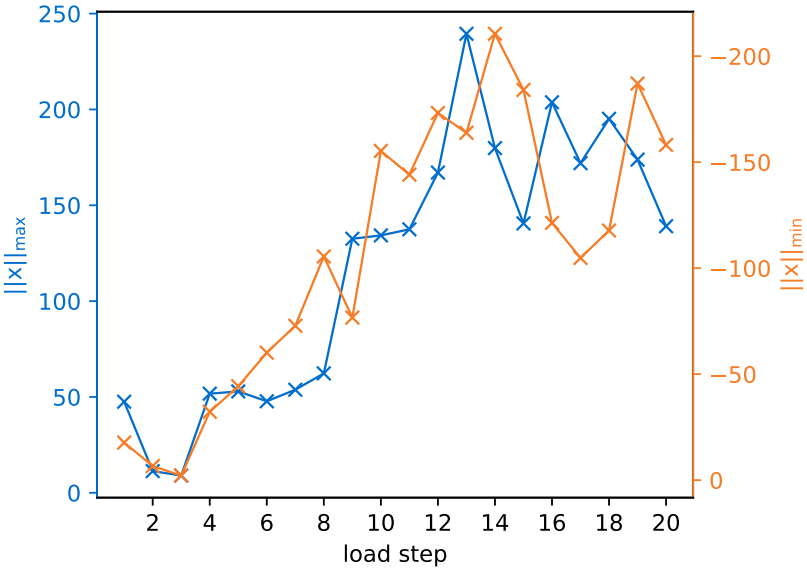

Figure A.41: Development of $||x||_{max}$ and $||x||_{min}$ for the first 20 load steps with ε as Measurement.

List of Figures

List of Tables

Bibliography

[1] *Brückenstatistik*. Bundesanstalt für Straßenwesen. 2023.

[2] *DIN 1076:1999-11, Ingenieurbauwerke im Zuge von Straßen und Wegen - Überwachung und Prüfung*. DOI: 10.31030/8499929.

[3] M. Wenner et al. *Digitaler Zwilling von Brücken*. Tech. rep. Berlin, Germany: Federal Ministry for Digital and Transport, 2023.

[4] T. Planès and E. Larose. "A review of ultrasonic Coda Wave Interferometry in concrete". In: *Cement and Concrete Research* 53 (2013), pp. 248–255. DOI: 10.1016/j.cemconres.2013.07.009.

[5] F. Diewald, N. Epple, T. Kraenkel, C. Gehlen, and E. Niederleithinger. "Impact of External Mechanical Loads on Coda Waves in Concrete". In: *Materials* 15.16 (2022), p. 5482. DOI: 10.3390/ma15165482.

[6] Y. Zhang, O. Abraham, F. Grondin, A. Loukili, V. Tournat, A. L. Duff, B. Lascoup, and O. Durand. "Study of stress-induced velocity variation in concrete under direct tensile force and monitoring of the damage level by using thermally-compensated Coda Wave Interferometry". In: *Ultrasonics* 52.8 (2012), pp. 1038–1045. DOI: 10.1016/j.ultras.2012.08.011.

[7] E. Larose and S. Hall. "Monitoring stress related velocity variation in concrete with a 2.10^{-5} relative resolution using diffuse ultrasound". In: *The Journal of the Acoustical Society of America* 125 (2009), pp. 1853–1856. arXiv: 0901.1722 [physics.geo-ph].

[8] I. Lillamand, J.-F. Chaix, M.-A. Ploix, and V. Garnier. "Acoustoelastic effect in concrete material under uni-axial compressive loading". In: *NDT & E International* 43.8 (2010), pp. 655–660. DOI: 10.1016/j.ndteint.2010.07.001.

[9] F. Diewald, M. Denolle, J. J. Timothy, and C. Gehlen. "Impact of Temperature and Relative Humidity Variations on Coda Waves in Concrete". In: (2023). DOI: 10.2139/ssrn.4358600.

[10] C. Wunderlich and E. Niederleithinger. "Evaluation of Temperature Influence on Ultrasound Velocity in Concrete by Coda Wave Interferometry". In: *Nondestructive Testing of Materials and Structures*. Springer Netherlands, 2011, pp. 227–232. DOI: 10.1007/978-94-007-0723-8_33.

[11] T. Ju, S. Li, J. Achenbach, and J. Qu. "Effects of moisture on ultrasound propagation in cement mortar". In: *AIP Conference Proceedings* 1650.1 (2015), pp. 1409–1414. DOI: 10.1063/1.4914756. eprint: https://aip.scitation.org/doi/pdf/10.1063/1.4914756.

[12] E. Larose, T. Planes, V. Rossetto, and L. Margerin. "Locating a small change in a multiple scattering environment". In: *Applied Physics Letters* 96.20 (2010), p. 204101. DOI: 10.1063/1.3431269.

[13] F. Clauß, N. Epple, M. A. Ahrens, E. Niederleithinger, and P. Mark. "Correlation of Load-Bearing Behavior of Reinforced Concrete Members and Velocity Changes of Coda Waves". In: *Materials* 15.3 (2022), p. 738. DOI: 10.3390/ma15030738.

[14] E. Niederleithinger, X. Wang, M. Herbrand, and M. Müller. "Processing Ultrasonic Data by Coda Wave Interferometry to Monitor Load Tests of Concrete Beams". In: *Sensors* 18.6 (2018), p. 1971. DOI: 10.3390/s18061971.

[15] X. Wang and E. Niederleithinger. "Coda Wave Interferometry Used To Detect Loads And Cracks In A Concrete Structure Under Field Conditions". In: (2018). DOI: 10.5281/ZENODO.1402380.

[16] X. Wang, E. Niederleithinger, J. Chakraborty, and P. Klikowicz. "Monitoring a concrete bridge girder with the coda wave interferometry method". en. In: (2019). DOI: 10.5281/ZENODO.3520603.

[17] X. Wang, J. Chakraborty, A. Bassil, and E. Niederleithinger. "Detection of Multiple Cracks in Four-Point Bending Tests Using the Coda Wave Interferometry Method". In: *Sensors* 20.7 (2020), p. 1986. DOI: 10.3390/s20071986.

[18] H. Zhan, H. Jiang, J. Zhang, and R. Jiang. "Condition Evaluation of an Existing T-Beam Bridge Based on Neutral Axis Variation Monitored with Ultrasonic Coda Waves in a Network of Sensors". In: *Sensors* 20.14 (2020), p. 3895. DOI: 10.3390/s20143895.

[19] A. Hafiz and T. Schumacher. "Monitoring of Stresses in Concrete Using Ultrasonic Coda Wave Comparison Technique". In: *Journal of Nondestructive Evaluation* 37.4 (2018). DOI: 10.1007/s10921-018-0527-8.

[20] E. Larose, A. Obermann, A. Digulescu, T. Planès, J.-F. Chaix, F. Mazerolle, and G. Moreau. "Locating and characterizing a crack in concrete with diffuse ultrasound: A four-point bending test". In: *The Journal of the Acoustical Society of America* 138.1 (2015), pp. 232–241. DOI: 10.1121/1.4922330.

[21] Y. Zhang, T. Planès, E. Larose, A. Obermann, C. Rospars, and G. Moreau. "Diffuse ultrasound monitoring of stress and damage development on a 15-ton concrete beam". In: *The Journal of the Acoustical Society of America* 139.4 (2016), pp. 1691–1701. DOI: 10.1121/1.4945097.

[22] Y. Zhang, E. Larose, L. Moreau, and G. d'Ozouville. "Three-dimensional in-situ imaging of cracks in concrete using diffuse ultrasound". In: *Structural Health Monitoring* 17.2 (2017), pp. 279–284. DOI: 10.1177/1475921717690938.

[23] T. Planès, E. Larose, V. Rossetto, and L. Margerin. "Imaging multiple local changes in heterogeneous media with diffuse waves". In: *The Journal of the Acoustical Society of America* 137.2 (2015), pp. 660–667. DOI: 10.1121/1.4906824.

[24] M. Grieves. "Digital Twin: Manufacturing Excellence through Virtual Factory Replication". In: (2015).

[25] Google. *Google Maps*. maps.google.com. [Online; accessed 25-March-2024].

[26] D. Gelernter. *Mirror Worlds. or the Day Software Puts the Universe in a Shoebox...How It Will Happen and What It Will Mean*. Oxford University Press, USA, 1991, p. 256. ISBN: 9780195079067.

[27] M. Grieves. *SME Management Forum Completing the Cycle: Using PLM Information in the Sales and Service Functions*. 2002.

[28] M. W. Grieves. "Product lifecycle management: the new paradigm for enterprises". In: *International Journal of Product Development* 2.1/2 (2005), p. 71. DOI: 10.1504/ijpd.2005.006669.

[29] M. Grieves. "Back to the Future: Product Lifecycle Management and the Virtualization of Product Information". In: *Product Realization*. Springer US, 2008, pp. 1–13. ISBN: 9780387094823. DOI: 10.1007/978-0-387-09482-3_3.

[30] M. Grieves. *Origins of the Digital Twin Concept*. 2016. DOI: 10.13140/RG.2.2.26367.61609.

[31] M. Shafto, M. Conroy, R. Doyle, E. Glaessgen, C. Kemp, J. LeMoigne, and L. Wang. *Modeling, Simulation, Information Technology and Processing Roadmap*. Tech. rep. 2010.

[32] Centre for Digital Built Britain. *National Digital Twin Programme*. https://www.cdbb.cam.ac.uk/what-we-did/national-digital-twin-programme. [Online; accessed 25-March-2024]. 2019.

[33] M. Grieves and J. Vickers. "Digital Twin: Mitigating Unpredictable, Undesirable Emergent Behavior in Complex Systems". In: *Transdisciplinary Perspectives on Complex Systems*. Springer International Publishing, 2016, pp. 85–113. ISBN: 9783319387567. DOI: 10.1007/978-3-319-38756-7_4.

[34] A. Madni, C. Madni, and S. Lucero. "Leveraging Digital Twin Technology in Model-Based Systems Engineering". In: *Systems* 7.1 (2019), p. 7. DOI: 10.3390/systems7010007.

[35] Arup. *Digital twin: towards a meaningful framework*. Tech. rep. London, UK: Arup, 2019.

[36] L. W. Aaron Parrott. *Industry 4.0 and the digital twin*. Tech. rep. Deloitte University Press, 2017.

[37] GE Digital. *Meet the Digital Twin.* https://www.youtube.com/watch?v=2dCz3oL2rTw. [Online; accessed 25-March-2024]. 2016.

[38] IBM. *What is a digital twin?* https://www.ibm.com/topics/what-is-a-digital-twin. [Online; accessed 25-March-2024]. 2019.

[39] Siemens. *Digital twin.* https://www.plm.automation.siemens.com/global/en/our-story/glossary/digital-twin/24465. [Online; accessed 25-March-2024]. 2019.

[40] M. Liu, S. Fang, H. Dong, and C. Xu. "Review of digital twin about concepts, technologies, and industrial applications". In: *Journal of Manufacturing Systems* 58 (2021), pp. 346–361. DOI: 10.1016/j.jmsy.2020.06.017.

[41] L. Wright and S. Davidson. "How to tell the difference between a model and a digital twin". In: *Advanced Modeling and Simulation in Engineering Sciences* 7.1 (2020). DOI: 10.1186/s40323-020-00147-4.

[42] W. Kritzinger, M. Karner, G. Traar, J. Henjes, and W. Sihn. "Digital Twin in manufacturing: A categorical literature review and classification". In: *IFAC-PapersOnLine* 51.11 (2018), pp. 1016–1022. DOI: 10.1016/j.ifacol.2018.08.474.

[43] J. Banks, ed. *Handbook of Simulation: Principles, Methodology, Advances, Applications, and Practice.* Wiley, 1998. ISBN: 9780470172445. DOI: 10.1002/9780470172445.

[44] T. Bauernhansl, J. Krüger, G. Reinhart, and G. Schuh. "WGP-Standpunkt Industrie 4.0". In: (2016). Ed. by E. Abele. DOI: 10.24406/PUBLICA-FHG-297876.

[45] M. Grabe, C. Ullerich, M. Wenner, and M. Herbrand. "smartBridge Hamburg – prototypische Pilotierung eines digitalen Zwillings". In: *Bautechnik* 97.2 (2020), pp. 118–125. DOI: 10.1002/bate.201900108.

[46] M. Wenner, M. Meyer-Westphal, M. Herbrand, and C. Ullerich. "The Concept of Digital Twin to Revolutionise Infrastructure Maintenance: the Pilot Project smartBRIDGE Hamburg". In: *27th ITS World Congress* (2021).

[47] A. Lazoglu, H. Naraniecki, I. Zaidman, and S. Marx. "A monitoring based digital twin for the Filstal bridges". In: *Life-Cycle of Structures and Infrastructure Systems.* CRC Press, 2023, pp. 205–212. ISBN: 9781003323020. DOI: 10.1201/9781003323020-22.

[48] I. Brilakis, Y. Pan, A. Borrmann, H.-G. Mayer, F. Rhein, C. Vos, E. Pettinato, and S. Wagner. "Built Environment Digital Twinning". In: *Report of the International Workshop on Built Environment Digital Twinning presented by TUM Institute for Advanced Study and Siemens AG.* Munich, Germany, 2019.

[49] S. Kaewunruen and N. Xu. "Digital Twin for Sustainability Evaluation of Railway Station Buildings". In: *Frontiers in Built Environment* 4 (2018). DOI: 10.3389/fbuil.2018.00077.

[50] S. Kaewunruen, P. Rungskunroch, and J. Welsh. "A Digital-Twin Evaluation of Net Zero Energy Building for Existing Buildings". In: *Sustainability* 11.1 (2018), p. 159. DOI: 10.3390/su11010159.

[51] S. Kaewunruen and Q. Lian. "Digital twin aided sustainability-based lifecycle management for railway turnout systems". In: *Journal of Cleaner Production* 228 (2019), pp. 1537–1551. DOI: 10.1016/j.jclepro.2019.04.156.

[52] F. N. Airaudo, R. Löhner, R. Wüchner, and H. Antil. "Adjoint-based determination of weaknesses in structures". In: *Computer Methods in Applied Mechanics and Engineering* 417 (2023), p. 116471. DOI: 10.1016/j.cma.2023.116471.

[53] R. Löhner, F. Airaudo, H. Antil, R. Wüchner, F. Meister, and S. Warnakulasuriya. "High-fidelity digital twins: Detecting and localizing weaknesses in structures". In: *International Journal for Numerical Methods in Engineering* (2024). DOI: 10.1002/nme.7568.

[54] J. Hadamard. *Lectures on Cauchy's problem in linear partial differential equations*. Yale University Press, 1923.

[55] R. Kress. *Numerical Analysis*. Springer New York, 1998. DOI: 10.1007/978-1-4612-0599-9.

[56] E. Moore. "On the reciprocal of the general algebraic matrix". In: *Bulletin of the American Mathematical Society* (1920).

[57] R. Penrose. "A generalized inverse for matrices". In: *Mathematical Proceedings of the Cambridge Philosophical Society* 51.3 (1955), pp. 406–413. DOI: 10.1017/s0305004100030401.

[58] D. L. Phillips. "A Technique for the Numerical Solution of Certain Integral Equations of the First Kind". In: *Journal of the ACM* 9.1 (1962), pp. 84–97. DOI: 10.1145/321105.321114.

[59] A. N. Tikhonov. "Solution of incorrectly formulated problems and the regularization method". In: *Soviet Math. Dokl.* 4 (1963), pp. 1035–1038.

[60] P. C. Hansen. "Analysis of Discrete Ill-Posed Problems by Means of the L-Curve". In: *SIAM Review* 34.4 (1992), pp. 561–580. DOI: 10.1137/1034115.

[61] M. Link. "Updating of Analytical Models-Procedures and". In: *Proceedings of Conference on Modern Practice in Stress and Vibration Analysis* (1993), pp. 35–52.

[62] Wikipedia. *Ridge regression/Tikhonov regularization — Wikipedia, The Free Encyclopedia*. http://en.wikipedia.org/w/index.php?title=Ridge\%20regression&oldid=1183899574. [Online; accessed 28-November-2023]. 2023.

[63] B. Weber, P. Paultre, and J. Proulx. "Consistent regularization of nonlinear model updating for damage identification". In: *Mechanical Systems and Signal Processing* 23.6 (2009), pp. 1965–1985. DOI: 10.1016/j.ymssp.2008.04.011.

[64] C. R. Vogel. *Inverse and ill-posed problems*. Ed. by H. W. Engl and C. Groetsch. Academic Press, 1987. Chap. An Overview of Numerical Methods for Nonlinear Ill-Posed Problems, pp. 231–245. ISBN: 0122390407.

[65] K. Levenberg. "A method for the solution of certain non-linear problems in least squares". In: *Quarterly of Applied Mathematics* 2.2 (1944), pp. 164–168. DOI: 10.1090/qam/10666.

[66] D. W. Marquardt. "An Algorithm for Least-Squares Estimation of Nonlinear Parameters". In: *Journal of the Society for Industrial and Applied Mathematics* 11.2 (1963), pp. 431–441. DOI: 10.1137/0111030.

[67] A. Tarantola and B. Valette. "Generalized nonlinear inverse problems solved using the least squares criterion". In: *Reviews of Geophysics* 20.2 (1982), pp. 219–232. DOI: 10.1029/rg020i002p00219.

[68] M. Link. "Updating of Analytical Models — Basic Procedures and Extensions". In: *Modal Analysis and Testing*. Springer Netherlands, 1999, pp. 281–304. ISBN: 9789401145039. DOI: 10.1007/978-94-011-4503-9_14.

[69] C. L. Lawson and R. J. Hanson. "Solving Least Squares Problems". In: *Solving Least Squares Problems*. Society for Industrial and Applied Mathematics, 1995. Chap. 23. Linear Least Squares with Linear Inequality Constraints, pp. 158–173. DOI: 10.1137/1.9781611971217.ch23.

[70] P. Stark and R. Parker. "Bounded-Variable Least-Squares: an Algorithm and Applications". In: *Computational Statistics* 10 (1995).

[71] M. A. Branch, T. F. Coleman, and Y. Li. "A Subspace, Interior, and Conjugate Gradient Method for Large-Scale Bound-Constrained Minimization Problems". In: *SIAM Journal on Scientific Computing* 21.1 (1999), pp. 1–23. DOI: 10.1137/s1064827595289108.

[72] Wikipedia. *Gradient descent — Wikipedia, The Free Encyclopedia*. http://en.wikipedia.org/w/index.php?title=Gradient\%20descent&oldid=1188975540. [Online; accessed 12-December-2023]. 2023.

[73] R. H. Byrd, R. B. Schnabel, and G. A. Shultz. "Approximate solution of the trust region problem by minimization over two-dimensional subspaces". In: *Mathematical Programming* 40–40.1–3 (1988), pp. 247–263. DOI: 10.1007/bf01580735.

[74] SciPy. *scipy.optimize.least_squares — SciPy v1.11.4 Manual*. https://docs.scipy.org/doc/scipy/reference/generated/scipy.optimize.least_squares.html. [Online; accessed 12-December-2023]. 2023.

[75] S. Lee, N. Kalos, and D. H. Shin. "Non-destructive testing methods in the U.S. for bridge inspection and maintenance". In: *KSCE Journal of Civil Engineering* 18.5 (2014), pp. 1322–1331. DOI: 10.1007/s12205-014-0633-9.

[76] D. McCann and M. Forde. "Review of NDT methods in the assessment of concrete and masonry structures". In: *NDT & E International* 34.2 (2001), pp. 71–84. DOI: 10.1016/s0963-8695(00)00032-3.

[77] K. Schiebold. *Zerstörungsfreie Werkstoffprüfung - Ultraschallprüfung*. Springer Berlin Heidelberg, 2015. DOI: 10.1007/978-3-662-44700-0.

[78] N. Yoder and D. Adams. "Commonly used sensors for civil infrastructures and their associated algorithms". In: *Sensor Technologies for Civil Infrastructures*. Elsevier, 2014, pp. 57–85. DOI: 10.1533/9780857099136.57.

[79] K. Worden and J. M. Dulieu-Barton. "An Overview of Intelligent Fault Detection in Systems and Structures". In: *Structural Health Monitoring* 3.1 (2004), pp. 85–98. DOI: 10.1177/1475921704041866.

[80] A. Rytter. "Vibrational Based Inspection of Civil Engineering Structures". English. Ph.D.-Thesis defended publicly at the University of Aalborg, April 20, 1993 PDF for print: 206 pp. PhD thesis. Denmark, 1993.

[81] *Beton angeschliffen*. Wikimedia Commons. 2006.

[82] J. Wolf. "Schadenserkennung in Beton durch Überwachung mit eingebetteten Ultraschallprüfköpfen". PhD thesis. Universität Potsdam, 2017, pp. ix, 142.

[83] *Different types of waves*. Wikimedia Commons. 2007.

[84] R. L. Weaver. "On diffuse waves in solid media". In: *The Journal of the Acoustical Society of America* 71.6 (1982), pp. 1608–1609. DOI: 10.1121/1.387816.

[85] W. Gao, C. Glorieux, S. E. Kruger, K. V. de Rostyne, V. Gusev, W. Lauriks, and J. Thoen. "Investigation of the microstructure of cast iron by laser ultrasonic surface wave spectroscopy". In: *Materials Science and Engineering: A* 313.1-2 (2001), pp. 170–179. DOI: 10.1016/s0921-5093(01)01143-1.

[86] W. P. Mason and H. J. McSkimin. "Attenuation and Scattering of High Frequency Sound Waves in Metals and Glasses". In: *The Journal of the Acoustical Society of America* 19.3 (1947), pp. 464–473. DOI: 10.1121/1.1916504.

[87] A. B. Bhatia. "Scattering of High-Frequency Sound Waves in Polycrystalline Materials". In: *The Journal of the Acoustical Society of America* 31.1 (1959), pp. 16–23. DOI: 10.1121/1.1907605.

[88] E. P. Papadakis. "5. Scattering in Polycrystalline Media". In: *Methods in Experimental Physics*. Elsevier, 1981, pp. 237–298. DOI: 10.1016/s0076-695x(08)60336-1.

[89] J. A. Turner and R. L. Weaver. "Radiative transfer and multiple scattering of diffuse ultrasound in polycrystalline media". In: *The Journal of the Acoustical Society of America* 96.6 (1994), pp. 3675–3683. DOI: 10.1121/1.410587.

[90] E. P. Papadakis. "Revised Grain-Scattering Formulas and Tables". In: *The Journal of the Acoustical Society of America* 37.4 (1965), pp. 703–710. DOI: 10.1121/1.1909399.

[91] K. Aki. "Correlogram Analyses of Seismograms by Means of a Simple Automatic Computer." In: *Journal of Physics of the Earth* 4.2 (1956), pp. 71–79. DOI: 10.4294/jpe1952.4.71.

[92] K. Aki and B. Chouet. "Origin of coda waves: Source, attenuation, and scattering effects". In: *Journal of Geophysical Research* 80.23 (1975), pp. 3322–3342. DOI: 10.1029/jb080i023p03322.

[93] M. B. Priestley. *Spectral analysis and time series*. London New York: Academic Press, 1981. Chap. 9, p. 704. ISBN: 9780125649018.

[94] P. M. Roberts, W. S. Phillips, and M. C. Fehler. "Development of the active doublet method for measuring small velocity and attenuation changes in solids". In: *The Journal of the Acoustical Society of America* 91.6 (1992), pp. 3291–3302. DOI: 10.1121/1.402864.

[95] C. Sens-Schönfelder and U. Wegler. "Passive image interferometry and seasonal variations of seismic velocities at Merapi Volcano, Indonesia". In: *Geophysical Research Letters* 33.21 (2006). DOI: 10.1029/2006gl027797.

[96] E. Niederleithinger and C. Wunderlich. "Influence of small temperature variations on the ultrasonic velocity in concrete". In: *AIP Conference Proceedings*. AIP, 2013. DOI: 10.1063/1.4789074.

[97] H. Sun and J. Zhu. "Thermal modulation of nonlinear ultrasonic wave for concrete damage evaluation". In: *The Journal of the Acoustical Society of America* 145.5 (2019), EL405–EL409. DOI: 10.1121/1.5108532.

[98] X. Wang, E. Niederleithinger, and I. Hindersmann. "The installation of embedded ultrasonic transducers inside a bridge to monitor temperature and load influence using coda wave interferometry technique". In: *Structural Health Monitoring* 21.3 (2021), pp. 913–927. DOI: 10.1177/14759217211014430.

[99] L. Brillouin. "Les tensions de radiation ; leur interprétation en mécanique classique et en relativité". In: *Journal de Physique et le Radium* 6.11 (1925), pp. 337–353. DOI: 10.1051/jphysrad:0192500601103370O.

[100] R. A. Guyer. *Nonlinear mesoscopic elasticity the complex behaviour of granular media including rocks and soil. the complex behaviour of granular media including rocks and soil*. Wiley-VCH, 2009, p. 395. ISBN: 9783527628261.

[101] P. Shokouhi, A. Zoëga, and H. Wiggenhauser. "Nondestructive Investigation of Stress-Induced Damage in Concrete". In: *Advances in Civil Engineering* 2010 (2010), pp. 1–9. DOI: 10.1155/2010/740189.

[102] D. P. Schurr, J.-Y. Kim, K. G. Sabra, and L. J. Jacobs. "Damage detection in concrete using coda wave interferometry". In: *NDT & E International* 44.8 (2011), pp. 728–735. DOI: 10.1016/j.ndteint.2011.07.009.

[103] D. Masera, P. Bocca, and A. Grazzini. "Coda Wave Interferometry Method Applied in Structural Monitoring to Assess Damage Evolution in Masonry and Concrete Structures". In: *Journal of Physics: Conference Series* 305 (2011), p. 012108. DOI: 10.1088/1742-6596/305/1/012108.

[104] Y. Zhang et al. "Following Stress Level Modification of Real Size Concrete Structures with Coda Wave Interferometry (CWI)". In: *AIP Conference Proceedings*. AIP, 2011. DOI: 10.1063/1.3592082.

[105] C. Sayers. "Stress-induced ultrasonic wave velocity anisotropy in fractured rock". In: *Ultrasonics* 26.6 (1988), pp. 311–317. DOI: 10.1016/0041-624x(88)90028-5.

[106] P. Shokouhi, A. Zoëga, H. Wiggenhauser, and G. Fischer. "Surface Wave Velocity-Stress Relationship in Uniaxially Loaded Concrete". English. In: *ACI Materials Journal* 109.2 (2012), pp. 141–148.

[107] W. Suaris and V. Fernando. "Ultrasonic Pulse Attenuation as a Measure of Damage Growth During Cyclic Loading of Concrete". In: *Aci Materials Journal* 84 (1987), pp. 185–193.

[108] E. Niederleithinger, J. Wolf, F. Mielentz, H. Wiggenhauser, and S. Pirskawetz. "Embedded Ultrasonic Transducers for Active and Passive Concrete Monitoring". In: *Sensors* 15.5 (2015), pp. 9756–9772. DOI: 10.3390/s150509756.

[109] F. Clauß, M. A. Ahrens, and P. Mark. "A comparative evaluation of strain measurement techniques in reinforced concrete structures–A discussion of assembly, application, and accuracy". In: *Structural Concrete* 22.5 (2021), pp. 2992–3007. DOI: 10.1002/suco.202000706.

[110] S. Grabke, K.-U. Bletzinger, and R. Wüchner. "Development of a finite element-based damage localization technique for concrete by applying coda wave interferometry". In: *Engineering Structures* 269 (2022), p. 114585. DOI: 10.1016/j.engstruct.2022.114585.

[111] R. Courant, K. Friedrichs, and H. Lewy. "Über die partiellen Differenzengleichungen der mathematischen Physik". In: *Mathematische Annalen* 100.1 (1928), pp. 32–74. DOI: 10.1007/bf01448839.

[112] C. Finger, L. Saydak, G. Vu, J. J. Timothy, G. Meschke, and E. H. Saenger. "Sensitivity of Ultrasonic Coda Wave Interferometry to Material Damage—Observations from a Virtual Concrete Lab". In: *Materials* 14.14 (2021), p. 4033. DOI: 10.3390/ma14144033.

[113] L. Ryzhik, G. Papanicolaou, and J. B. Keller. "Transport equations for elastic and other waves in random media". In: *Wave Motion* 24.4 (1996), pp. 327–370. DOI: 10.1016/s0165-2125(96)00021-2.

[114] J. Crank. *The Mathematics of Diffusion*. Oxford Eng: Oxford University Press, 1975. 424 pp. ISBN: 0198533446.

[115] T. Planès, E. Larose, L. Margerin, V. Rossetto, and C. Sens-Schönfelder. "Decorrelation and phase-shift of coda waves induced by local changes: multiple scattering approach and numerical validation". In: *Waves in Random and Complex Media* 24.2 (2014), pp. 99–125. DOI: 10.1080/17455030.2014.880821.

[116] J. C. J. Paasschens. "Solution of the time-dependent Boltzmann equation". In: *Physical Review E* 56.1 (1997), pp. 1135–1141. DOI: 10.1103/physreve.56.1135.

[117] N. Ottosen and H. Petersson. *Introduction to the finite element method*. New York: Prentice Hall, 1992. ISBN: 9780134738772.

[118] O. C. Zienkiewicz, R. L. Taylor, and J. Z. Zhu. *The Finite Element Method: Its Basis and Fundamentals*. Elsevier LTD, Oxford, 2013. 768 pp. ISBN: 1856176339.

[119] J. Crank and P. Nicolson. "A practical method for numerical evaluation of solutions of partial differential equations of the heat-conduction type". In: *Mathematical Proceedings of the Cambridge Philosophical Society* 43.1 (1947), pp. 50–67. DOI: 10.1017/s0305004100023197.

[120] J. Taler and P. Ocłon. "Finite Element Method in Steady-State and Transient Heat Conduction". In: *Encyclopedia of Thermal Stresses*. Ed. by R. B. Hetnarski. SPRINGER NATURE, 2014, pp. 1604–1633. ISBN: 9400727402.

[121] P. Sheng. *Introduction to wave scattering, localization, and mesoscopic phenomena*. San Diego: Academic Press, 1995. ISBN: 0126398453.

[122] C. Pacheco and R. Snieder. "Time-lapse travel time change of multiply scattered acoustic waves". In: *The Journal of the Acoustical Society of America* 118.3 (2005), pp. 1300–1310. DOI: 10.1121/1.2000827.

[123] V. Rossetto, L. Margerin, T. Planès, and É. Larose. "Locating a weak change using diffuse waves: Theoretical approach and inversion procedure". In: *Journal of Applied Physics* 109.3 (2011), p. 034903. DOI: 10.1063/1.3544503.

[124] H. Zhan, H. Jiang, and R. Jiang. "Three-dimensional images generated from diffuse ultrasound wave: detections of multiple cracks in concrete structures". In: *Structural Health Monitoring* 19.1 (2019), pp. 12–25. DOI: 10.1177/1475921719834045.

[125] H. Jiang, H. Zhan, Z. Ma, and R. Jiang. "Comparative Study of Three-Dimensional Stress and Crack Imaging in Concrete by Application of Inverse Algorithms to Coda Wave Measurements". In: *Sensors* 20.17 (2020), p. 4899. DOI: 10.3390/s20174899.

[126] F. Xie, E. Larose, L. Moreau, Y. Zhang, and T. Planes. "Characterizing extended changes in multiple scattering media using coda wave decorrelation: numerical simulations". In: *Waves in Random and Complex Media* 28.1 (2017), pp. 1–14. DOI: 10.1080/17455030.2017.1308042.

[127] Q. Xue, E. Larose, and L. Moreau. "Locating structural changes in a multiple scattering domain with an irregular shape". In: *The Journal of the Acoustical Society of America* 146.1 (2019), pp. 595–602. DOI: 10.1121/1.5118246.

[128] V. M. Ferrándiz et al. *KratosMultiphysics/Kratos: Release v9.5*. en. 2024. DOI: 10.5281/ZENODO.3234644.

[129] S. Grabke, F. Clauß, K.-U. Bletzinger, M. A. Ahrens, P. Mark, and R. Wüchner. "Damage Detection at a Reinforced Concrete Specimen with Coda Wave Interferometry". In: *Materials* 14.17 (2021), p. 5013. DOI: 10.3390/ma14175013.

[130] F. Clauß, N. Epple, M. A. Ahrens, E. Niederleithinger, and P. Mark. "Comparison of Experimentally Determined Two-Dimensional Strain Fields and Mapped Ultrasonic Data Processed by Coda Wave Interferometry". In: *Sensors* 20.14 (2020), p. 4023. DOI: 10.3390/s20144023.

[131] A. Savitzky and M. J. E. Golay. "Smoothing and Differentiation of Data by Simplified Least Squares Procedures." In: *Analytical Chemistry* 36.8 (1964), pp. 1627–1639. DOI: 10.1021/ac60214a047.

[132] C. Pacheco and R. Snieder. "Time-lapse traveltime change of singly scattered acoustic waves". In: *Geophysical Journal International* 165.2 (2006), pp. 485–500. DOI: 10.1111/j.1365-246x.2006.02856.x.

[133] P. Fröjd. "Structural health monitoring of concrete structures using diffuse waves". English. PhD thesis. Department of Biomedical Engineering, 2018. ISBN: 978-91-7753-581-2.

[134] A. Müller, C. Sodeikat, J. Schänzlin, F. Knab, L. Albrecht, R. Groschup, and P. Obermeier. "Die Gänstorbrücke in Ulm – Untersuchung, Probebelastung und Brückenmonitoring". In: *Beton- und Stahlbetonbau* 115.3 (2019), pp. 164–178. DOI: 10.1002/best.201900071.

[135] T. J. R. Hughes. *The finite element method. linear static and dynamic finite element analysis*. Prentice-Hall, 1987. ISBN: 0133170179.

[136] K. J. Bathe. *Finite-Elemente-Methoden*. Springer, 2001, p. 1253. ISBN: 9783540668060.

[137] C. A. Felippa. "Introduction to Finite Element Methods". https://vulcanhammernet.files.wordpress.com/2017/01/ifem.pdf. Accessed: 2024–01-08. 2004.

[138] J. E. Mottershead, M. Link, and M. I. Friswell. "The sensitivity method in finite element model updating: A tutorial". In: *Mechanical Systems and Signal Processing* 25.7 (2011), pp. 2275–2296. DOI: 10.1016/j.ymssp.2010.10.012.

[139] M. Fußeder. "Methodological and Application-Oriented Advances in Sensitivity Analysis with a Focus on Structural Engineering". PhD thesis. Technical University of Munich, 2024.

[140] K.-U. Bletzinger, M. Firl, and F. Daoud. "Approximation of derivatives in semi-analytical structural optimization". In: *Computers & Structures* 86.13 (2008). Structural Optimization, pp. 1404–1416. DOI: https://doi.org/10.1016/j.compstruc.2007.04.014.

[141] C. Gengdong and L. Yingwei. "A New Computation Scheme for Sensitivity Analysis". In: *Engineering Optimization* 12.3 (1987), pp. 219–234. DOI: 10.1080/03052158708941096.

[142] H. Masching. "Parameter Free Optimization of Shape Adaptive Shell Structures". en. PhD thesis. Technische Universität München, 2016, p. 208.

[143] M. Fußeder, R. Wüchner, and K.-U. Bletzinger. "Sensitivitätsanalyse mit verallgemeinerten Einflussfunktionen zur Tragwerksbewertung bei Modellparametervariationen/Sensitivity analysis with generalized influence functions for the treatment of model parameter variations in structural analysis". In: *Bauingenieur* 96.06 (2021), pp. 191–200. DOI: 10.37544/0005-6650-2021-06-33.

[144] M. Fußeder, R. Wüchner, and K.-U. Bletzinger. "Towards a computational engineering tool for structural sensitivity analysis based on the method of influence functions". In: *Engineering Structures* 265 (2022), p. 114402. DOI: 10.1016/j.engstruct.2022.114402.

[145] S. Stöhr. "Identifikation von lokalen Steifigkeitsmodifikationen an Brückentragwerken unter Verwendung experimenteller Einflusslinien". PhD thesis. Kassel University, 2009. ISBN: 978-3-89958-476-9.

[146] M. I. Friswell. *Finite Element Model Updating in Structural Dynamics*. Springer Netherlands, 1995, p. 292. ISBN: 9789048145355.

[147] J. E. Mottershead and C. D. Foster. "On the treatment of ill-conditioning in spatial parameter estimation from measured vibration data". In: *Mechanical Systems and Signal Processing* 5.2 (1991), pp. 139–154. DOI: 10.1016/0888-3270(91)90020-6.

[148] U. Prells. "A regularization method for the linear error localization of models of elastomechanical systems". In: *Inverse Problems in Engineering* 3.4 (1996), pp. 197–217. DOI: 10.1080/174159796088027624.

[149] *GOM Correlate*. GOM Software 2019 (2019 Hotfix 7, Rev. 128764, Build 2020-06-18). 2019.

Bisherige Titel der Schriftenreihe

Band	Titel
1	Frank Koschnick, *Geometrische Lockingeffekte bei Finiten Elementen und ein allgemeines Konzept zu ihrer Vermeidung*, 2004.
2	Natalia Camprubi, *Design and Analysis in Shape Optimization of Shells*, 2004.
3	Bernhard Thomee, *Physikalisch nichtlineare Berechnung von Stahlfaserbetonkonstruktionen*, 2005.
4	Fernaß Daoud, *Formoptimierung von Freiformschalen - Mathematische Algorithmen und Filtertechniken*, 2005.
5	Manfred Bischoff, *Models and Finite Elements for Thin-walled Structures*, 2005.
6	Alexander Hörmann, *Ermittlung optimierter Stabwerkmodelle auf Basis des Kraftflusses als Anwendung plattformunabhängiger Prozesskopplung*, 2006.
7	Roland Wüchner, *Mechanik und Numerik der Formfindung und Fluid-Struktur-Interaktion von Membrantragwerken*, 2006.
8	Florian Jurecka, *Robust Design Optimization Based on Metamodeling Techniques*, 2007.
9	Johannes Linhard, *Numerisch-mechanische Betrachtung des Entwurfsprozesses von Membrantragwerken*, 2009.
10	Alexander Kupzok, *Modeling the Interaction of Wind and Membrane Structures by Numerical Simulation*, 2009.

Band Titel

11 Bin Yang, *Modified Particle Swarm Optimizers and their Application to Robust Design and Structural Optimization*, 2009.

12 Michael Fleischer, *Absicherung der virtuellen Prozesskette für Folgeoperationen in der Umformtechnik*, 2009.

13 Amphon Jrusjrungkiat, *Nonlinear Analysis of Pneumatic Membranes - From Subgrid to Interface*, 2009.

14 Alexander Michalski, *Simulation leichter Flächentragwerke in einer numerisch generierten atmosphärischen Grenzschicht*, 2010.

15 Matthias Firl, *Optimal Shape Design of Shell Structures*, 2010.

16 Thomas Gallinger, *Effiziente Algorithmen zur partitionierten Lösung stark gekoppelter Probleme der Fluid-Struktur-Wechselwirkung*, 2011.

17 Josef Kiendl, *Isogeometric Analysis and Shape Optimal Design of Shell Structures*, 2011.

18 Joseph Jordan, *Effiziente Simulation großer Mauerwerksstrukturen mit diskreten Rissmodellen*, 2011.

19 Albrecht von Boetticher, *Flexible Hangmurenbarrieren: Eine numerische Modellierung des Tragwerks, der Hangmure und der Fluid-Struktur-Interaktion*, 2012.

20 Robert Schmidt, *Trimming, Mapping, and Optimization in Isogeometric Analysis of Shell Structures*, 2013.

21 Michael Fischer, *Finite Element Based Simulation, Design and Control of Piezoelectric and Lightweight Smart Structures*, 2013.

22 Falko Hartmut Dieringer, *Numerical Methods for the Design and Analysis for Tensile Structures*, 2014.

23 Rupert Fisch, *Code Verification of Partitioned FSI Environments for Lightweight Structures*, 2014.

Band Titel

24 Stefan Sicklinger, *Stabilized Co-Simulation of Coupled Problems Including Fields and Signals*, 2014.

25 Madjid Hojjat, *Node-based parametrization for shape optimal design*, 2015.

26 Ute Israel, *Optimierung in der Fluid-Struktur-Interaktion - Sensitivitätsanalyse für die Formoptimierung auf Grundlage des partitionierten Verfahrens*, 2015.

27 Electra Stavropoulou, *Sensitivity analysis and regularization for shape optimization of coupled problems*, 2015.

28 Daniel Markus, *Numerical and Experimental Modeling for Shape Optimization of Offshore Structures*, 2015.

29 Pablo Suárez, *Design Process for the Shape Optimization of Pressurized Bulkheads as Components of Aircraft Structures*, 2015.

30 Armin Widhammer, *Variation of Reference Strategy - Generation of Optimized Cutting Patterns for Textile Fabrics*, 2015.

31 Helmut Masching, *Parameter Free Optimization of Shape Adaptive Shell Structures*, 2016.

32 Hao Zhang, *A General Approach for Solving Inverse Problems in Geophysical Systems by Applying Finite Element Method and Metamodel Techniques*, 2016.

33 Tianyang Wang, *Development of Co-Simulation Environment and Mapping Algorithms*, 2016.

34 Michael Breitenberger, *CAD-integrated Design and Analysis of Shell Structures*, 2016.

35 Önay Can, *Functional Adaptation with Hyperkinematics using Natural Element Method: Application for Articular Cartilage*, 2016.

Band Titel

36 Benedikt Philipp, *Methodological Treatment of Non-linear Structural Behavior in the Design, Analysis and Verification of Lightweight Structures*, 2017.

37 Michael Andre, *Aeroelastic Modeling and Simulation for the Assessment of Wind Effects on a Parabolic Trough Solar Collector*, 2018.

38 Andreas Apostolatos, *Isogeometric Analysis of Thin-Walled Structures on Multipatch Surfaces in Fluid-Structure Interaction*, 2018.

39 Altuğ Emiroğlu, *Multiphysics Simulation and CAD-Integrated Shape Optimization in Fluid-Structure Interaction*, 2019.

40 Mehran Saeedi, *Multi-Fidelity Aeroelastic Analysis of Flexible Membrane Wind Turbine Blades*, 2017.

41 Reza Najian Asl, *Shape optimization and sensitivity analysis of fluids, structures, and their interaction using Vertex Morphing Parametrization*, 2019.

42 Ahmed Abodonya, *Verification Methodology for Computational Wind Engineering Prediction of Wind Loads on Structures*, 2020.

43 Anna Maria Bauer, *CAD-integrated Isogeometric Analysis and Design of Lightweight Structures*, 2020.

44 Andreas Winterstein, *Modeling and Simulation of Wind Structure Interaction of Slender Civil Engineering Structures Including Vibration Systems*, 2020.

45 Franz-Josef Ertl, *Vertex Morphing for Constrained Shape Optimization of Three-dimensional Solid Structures*, 2020.

46 Daniel Baumgärtner, *On the Grid-based Shape Optimization of Structures with Internal Flow and the Feedback of Shape Changes into a CAD Model*, 2020.

47 Mohamed Khalil, *Combining Physics-based models and machine learning for an Enhanced Structural Health Monitoring*,2021.

Band Titel

48 Long Chen, *Gradient Descent Akin Method*, 2021.

49 Aditya Ghantasala, *Coupling Procedures for Fluid-Fluid and Fluid-Structure Interaction Problems Based on Domain Decomposition Methods*, 2021.

50 Ann-Kathrin Goldbach, *The Cad-Integrated Design Cycle for Structural Membranes*, 2022.

51 Iñigo Pablo López Canalejo„ *A Finite-Element Transonic Potential Flow Solver with an Embedded Wake Approach for Aircraft Conceptual Design*, 2022.

52 Mayu Sakuma, *An Application of Multi-Fidelity Uncertainty Quantification for Computational Wind Engineering*, 2022.

53 Suneth Warnakulasuriya, *Development of methods for Finite Element-based sensitivity analysis and goal-directed mesh refinement using the adjoint approach for steady and transient flows*, 2022.

54 Klaus Bernd Sautter, *Modeling and Simulation of Flexible Protective Structures by Coupling Particle and Finite Element Methods*, 2022.

55 Efthymios Papoutsis, *On the incorporation of industrial constraints in node-based optimization for car body design*, 2023.

56 Thomas Josef Oberbichler, *A modular and efficient implementation of isogeometric analysis for the interactive CAD-integrated design of lightweight structures*, 2023.

57 Tobias Christoph Teschemacher, *CAD-integrated constitutive modelling, analysis, and design of masonry structures*, 2023.

58 Shahrokh Shayegan, *Enhanced Algorithms for Fluid-Structure Interaction Simulations – Accurate Temporal Discretization and Robust Convergence Acceleration*, 2023.

Band Titel

59 Ihar Antonau, *Enhanced computational design methods for large industrial node-based shape optimization problems*, 2023.

60 Rishith Ellath Meethal, *Hybrid modelling and simulation approaches for the solution of forward and inverse problems in engineering by combining finite element methods and neural networks*, 2023.

61 Máté Péntek, *Method Development for the Numerical Wind Tunnel in Applied Structural Engineering*, 2023.

62 Anoop Kodakkal, *High Fidelity Modeling and Simulations for Uncertainty Quantification and Risk-averse Optimization of Structures Under Natural Wind Conditions*, 2024.

63 Philipp Bucher, *CoSimulation and Mapping for large scale engineering applications*, 2024.

64 Martin Fußeder, *Methodological and Application-Oriented Advances in Sensitivity Analysis with a Focus on Structural Engineering*, 2024.

65 Wenjia Wang, *Adjoint Sensitivity Analysis for Non-parametric Shape Optimization with Geometric Nonlinearity and Elastoplasticity*, 2024.

66 Manuel Meßmer, *Efficient and robust quadrature for embedded solids: Application to isogeometric analysis and shape optimizationg*, 2024.

67 Veronika Maria Singer, *Partitioned Coupling Strategies to Simulate Granular Mass Flows Impacting Flexible Protective Structures*, 2024.

68 Stefan Grabke, *System Identification with Coda Waves and Model Updating for Digital Twins in Civil Engineering*, 2024.